



**Politecnico
di Torino**

Politecnico di Torino

Master's Degree in Mechanical engineering

Thesis

**Analysis of CD147 inhibitors such as ivermectin, azithromycin with respect to
their potential therapeutic use against the emerging COVID mutations**

Supervisors

Prof. Jacek Adam TUSZYNSKI

Prof. Marco Agostino DERIU

Candidate

Ehsan SAFAEEARDEBILI

July 2022

Abstract

It has been reported by clinical scientists that a macrocyclic lactone such as ivermectin showed some activity against new emerging SARS CoV-2 (COVID- 19). Since a biological mechanism proposed for this anti-viral effect is not solely adequate to draw a conclusion at the physiological scale, this in silico investigation is conducted to identify potential modes of action of ivermectin against COVID-19. In this regard, a vast multi target molecular simulation has been implemented to assess not only Ivermectin, but also other structurally similar compounds to identify a possible therapeutic solution. Ivermectin and 14 other compounds, whose use may cause the infectivity and morbidity of the SARS CoV-2 to be reduced. Molecular simulations have been conducted in MOE. Docking scores which represent the binding affinity between ligand and receptor have been computed for all 15 agents on several docking sites for FOUR targeted proteins. These targeted proteins are all involved in infection and spreads of SARS CoV-2 virus within the human body. The first one is the spike glycoprotein of the virus, for which over time many mutations occurred in its protein sequence and consequently in its 3D structure. Therefore, the second targeted protein is the mutated spike protein. since D614G is the most common mutation among all variants, this study is focused on this specific mutation. Third protein is the CD147 human receptor which has been identified as a secondary attachment target for the virus. The last considered receptor is the alpha-7 nicotinic acetylcholine receptor ($\alpha 7nAChr$), which is an activation site for the cholinergic anti-inflammatory pathway controlled by vagus nerve and is an indicated penetration point of neuronal tissue. Binding modes of each compound have been investigated, and all the binding affinities calculated for these multiple docking sites. Competitively high binding affinity for Ivermectin is identified and even higher binding affinities in case of other proposed compounds are reported for all four of these targeted proteins. These results suggest biological mechanisms by which ivermectin may limit the infectivity and morbidity of the both original and mutated SARS- CoV-2 virus and stimulate an

$\alpha 7$ nAChr-mediated anti-inflammatory pathway that could limit cytokine production by immune cells.

Acknowledgments

This master thesis represents my last contribution as a master student at Politecnico di Torino for earning a Master of Science (MSc) degree in Mechanical engineering. The topic of this thesis report is completely different with respect to my previous experience as a mechanical engineering student. First, I got to know this field of research in a course called “Rational Drug Discovery” with Prof. Tuszynski. The outcome of this course and latter research and contributions was a publication in this research fields under the name of “In Silico Analysis of the Multi-Targeted Mode of Action of Ivermectin and Related Compounds “. Completing this job would not have been possible without various people’s immense and persistent assistance and direction. First, I would like to express my sincere appreciation to Professor Jacek Tuszynski and Marco Deriu my supervisors at Politecnico di Torino for their full guidance and support in formulating my research aims. Especial thanks to Dr. Maral Aminpour from Alberta University in CANADA and all my teammates and Co-Authors of our publication who were beside me during the submission of this paper. Mentioned publication is included in this thesis report both in method and result section since it is the base of presented thesis and is completed by the final results which derived in this dissertation.

Ehsan SafaeeArdebili

Table of Contents

LIST OF FIGURES	VIII
ABBREVIATION.....	X
1. LITERATURE REVIEW	3
1.1. CORONA VIRUS, SARS-CoV-2:.....	3
1.2. OVERALL STRUCTURE OF SARS-CoV-2 SPIKE PROTEIN:.....	3
1.3. N-TERMINAL DOMAIN.....	7
1.4. RECEPTOR BINDING DOMAIN	8
1.5. C-TERMINAL DOMAINS	10
1.6. S2 STRUCTURE.....	11
1.7. MUTATION:.....	13
1.8. TRANSMISSION EFFICIENCY OF SARS-CoV-2 G614 VARIANT:	14
1.9. STRUCTURAL AND MECHANISTIC IMPACT OF THE D614G MUTATION:	14
1.10. COMPETITIVE STRUCTURAL ADVANTAGES OF D614G MUTATION:	18
1.11. CD147:.....	24
1.12. INFLAMMATORY RESPONSES OF CD147:	26
1.13. NICOTINIC ACETYLCHOLINE RECEPTORS:	27
2. MATERIAL AND METHODS	30
2.1. LIGAND DATABASE PREPARATION:	30
2.2. PROTEIN PREPARATION:.....	30
2.3. BINDING SITES IDENTIFICATION:	31
2.4. MOLECULAR DOCKING SIMULATION:.....	44
2.5. MOLECULAR DYNAMICS SIMULATION:	46
2.6. LIGAND INTERACTION FINGERPRINT:.....	47
3. RESULTS	49
3.1. MOLECULAR DOCKING RESULT:	49
3.2. COMPOUNDS SELECTION:.....	53
3.3. MOLECULAR DYNAMICS SIMULATION AND RMSD ANALYSIS:.....	57
3.4. PROTEIN LIGAND INTERACTION:	59
3.5. BIOACTIVITY OF THE TEST AGENTS WITH GREATEST BINDING STRENGTH.....	66
4. CONCLUSIONS AND FUTURE RESEARCH.....	68
BIBLIOGRAPHY:.....	69

List of Figures

FIGURE 1.1. DISTINCT CONFORMATIONAL STATES OF THE SARS-CoV-2 SPIKE PROTEIN.	4
FIGURE 1.2. STRUCTURES OF NTD AND ITS ANTIBODY COMPLEXES.	6
FIGURE 1.3. STRUCTURES OF CTDs.	11
FIGURE 1.4. STRUCTURES AND PROPOSED CONFORMATIONAL CHANGES OF SARS-CoV S2.	12
FIGURE 1.5. STRUCTURAL AND EPISTRUCTURAL INTERACTIONS AT THE S1/S2 INTERFACE IN THE SPIKE PROTEIN OF SARS-CoV-2.	17
FIGURE 1.6. SURFACE REPRESENTATION OF THE SARS-COV2-S PROTEIN	18
FIGURE 1.7. STRUCTURAL REPRESENTATIONS OF D614 AND G614 SARS-CoV-2 S PROTEIN	21
FIGURE 1.8. ALIGNMENT OF MODELS OF THE D614 AND G614 CLEAVAGE DOMAINS WITH AN ACTIVE SITE INHIBITOR	22
FIGURE 1.9. ALIGNMENT OF D614 AND G614 IN THE CATALYTIC DOMAIN OF FURIN	23
FIGURE 1.10. CD147 OR BASIGIN ISOFORMS,	24
FIGURE 1.11. DEDUCED PROTEIN SEQUENCE OF HUMAN BSG PRECURSOR	25
TABLE 2.1. BINDING SITES OF SPIKE PROTEIN	32
TABLE 2.2. BINDING SITES OF MUTATED SPIKE PROTEIN	35
TABLE 2.3. BINDING SITES OF CD147	40
FIGURE 2.1. CD 147, BINDING SITES ILLUSTRATION	41
TABLE 2.4. BINDING SITES OF A7NACHR	41
FIGURE 2.2. BINDING SITES OF (A) DESENSITIZED, (B) ACTIVATED AND (C) RESTING CONFORMATIONS OF A7NACHR PROTEIN	43
FIGURE 2.3. POSITIVE CONTROL DOCKING OF EPIBATIDINE	45
FIGURE 2.4. DECOY COMPOUNDS.	46
TABLE 3.1. DOCKING SCORES OF ALL TESTED COMPOUNDS AND SPIKE PROTEIN	49
TABLE 3.2. DOCKING SCORES OF ALL SELECTED COMPOUNDS AND MUTATED SPIKE PROTEIN	51
TABLE 3.3. DOCKING SCORES OF ALL SELECTED COMPOUNDS AND CD147	52
TABLE 3.4. DOCKING SCORES OF ALL SELECTED COMPOUNDS AND A7NACHR	52
FIGURE 3.1. BINDING POSES OF LIGANDS AND SPIKE PROTEIN	54
FIGURE 3.2. DORAMECTIN AND MUTATED SPIKE PROTEIN COMPLEX	55
FIGURE 3.3. IVERMECTIN AND MUTATED SPIKE PROTEIN COMPLEX	55
FIGURE 3.4. AMPHOTERICIN-B AND MUTATED SPIKE PROTEIN COMPLEX	55
FIGURE 3.5. EPRINOMECTIN AND MUTATED SPIKE PROTEIN COMPLEX	55
FIGURE 3.6. GITOFORMATE AND MUTATED SPIKE PROTEIN COMPLEX	56
FIGURE 3.7. BINDING POSES OF TOP COMPOUNDS AND CD147	56
FIGURE 3.8. BINDING POSES OF TOP COMPOUNDS AND A7NACHR	57
FIGURE 3.9. LIGAND INTERACTION PLOTS OF IVERMECTIN AND (A)SPIKE PROTEIN, (B)CD147, (C)A7NACHR	59
FIGURE 3.10. LIGAND INTERACTION PLOTS OF IVERMECTIN FOR MUTATED SPIKE PROTEIN (AMINO ACID D614G)	60

FIGURE 3.12. LIGAND INTERACTION OF TOP COMPOUNDS AND SPIKE PROTEIN	61
FIGURE 3.13. AMPHOTERICIN B AND MUTATED SPIKE PROTEIN INTERACTION	62
FIGURE 3.14. DORAMECTIN AND MUTATED SPIKE PROTEIN INTERACTION	62
FIGURE 3.15. IVERMECTIN AND MUTATED SPIKE PROTEIN INTERACTION	63
FIGURE 3.16. EPRINOMECTIN AND MUTATED SPIKE PROTEIN INTERACTION	62
FIGURE 3.17. GITOFORMATE AND MUTATED SPIKE PROTEIN INTERACTION	63
FIGURE 3.18. LIGAND INTERACTION PLOTS OF COMPOUNDS SELECTED FOR CD147 INHIBITION (A) SELAMECTIN, (B) P-57AS3, (C) CONCANAMYCIN_A AND (D) IVERMECTIN	64
FIGURE 3.19. LIGAND INTERACTION PLOTS OF COMPOUNDS SELECTED FOR A7NACHR INHIBITION. (A) IVERMECTIN, (B) DORAMECTIN, (C) OKADAIC ACID, (D) MOXIDECTIN.	65

Abbreviation

the following abbreviations are used in this dissertation.

α 7nAChr	alpha-7 nicotinic acetylcholine receptor
ACE2	angiotensin converting enzyme 2
ACh	acetylcholine
BCov	bovine coronavirus
CD147	cluster of differentiation 147 protein, encoded by the BSG gene
Co-IP	co-immunoprecipitation
COVID-19	coronavirus disease 2019
ELISA	enzyme-linked immunosorbent assay
GPU	graphics processing unit
HE	hemagglutinin esterase
HIV	human immunodeficiency virus
IL-1	interleukin 1
IL-6	interleukin 6
MD	molecular dynamics
MERS	Middle East respiratory syndrome
MHV-4	mouse hepatitis virus 4, JHM strain
MOE	Molecular Operating Environment
NAG	N-acetyl-D-glucosamine
NTD	N-terminal domain
PDB	Protein Data Bank
PLB	propensity for ligand binding
RBC	red blood cell

RBD	receptor binding domain
RCSB	Research Collaboratory for Structural Bioinformatics
RCT	randomized clinical trial
RMSD	root mean square deviation
SA	sialic acid
SARS-CoV-2	severe acute respiratory syndrome coronavirus 2
SPR	surface plasmon resonance
TNF	tumor necrosis factor

Literature review

1. Literature review

1.1. Corona virus, SARS-CoV-2:

Severe acute respiratory syndrome coronavirus 2 (SARS- CoV-2) is the causative agent of the COVID-19 (corona- virus disease 2019) pandemic [163]. To control this unpleasant crisis there are urgent demand for vaccine or therapeutic solution as well as potential future needs if it becomes seasonal with continuous emergence of new dangerous variants. A deep knowledge of the relation between structure and the functionality of viral proteins and related host agents will be required in order to meet these needs. Coronaviruses (CoVs) are enveloped positive-stranded RNA viruses that penetrate the human host cell by fusion of its envelope lipid bilayer with the target cell membrane. This very initial vital step of viral infection is catalyzed by its trimeric spike (S) protein, which covers the virion surface as a major antigen and induces neutralizing antibody responses. Therefore, the protein is an important target for further development of diagnostics, therapeutics, and vaccines. Remarkable progress in the structural biology of SARS-CoV-2 S protein has been made since the initial emergence of the virus [164]. In the following paragraphs, a summary of the current knowledge on the structural and functionality of the SARS-CoV-2 S protein is provided which will be continued by introducing the most common variation among various mutations.

1.2. Overall structure of SARS-CoV-2 Spike protein:

Type I membrane protein, The SARS-CoV-2 spike glycoprotein (Figure 1a), which creates a trimer, anchored to the viral membrane by its transmembrane segment, while covering the virion surface with it huge ectodomain (Figure 1b). It binds to the receptor angiotensin-converting enzyme 2 (ACE2) on a human host cell and undergo massive structural rearrangements to elevate membrane fusion [163,165]. This protein is heavily and widely glycosylated with each protomer containing 22 N-linked glycosylation sites [166,167]. S protein in the full length, Wuhan-Hu-1 strain from the initial outbreak has 1273 amino acid residues, by considering a N-terminus signal peptide, a receptor-binding strand S1 and a fusion fragment S2. S1 is consists of a N-terminal domain (NTD), receptor-binding domain (RBD) and C-terminal domains (CTD1 and CTD2), while S2 includes fusion peptide (FP), fusion-peptide proximal region (FPPR), heptad repeat 1 (HR1), central helix (CH), connector domain (CD), heptad repeat 2 (HR2), trans- membrane segment (TM) and the cytoplasmic tail (CT), depicted in Figure 1a.

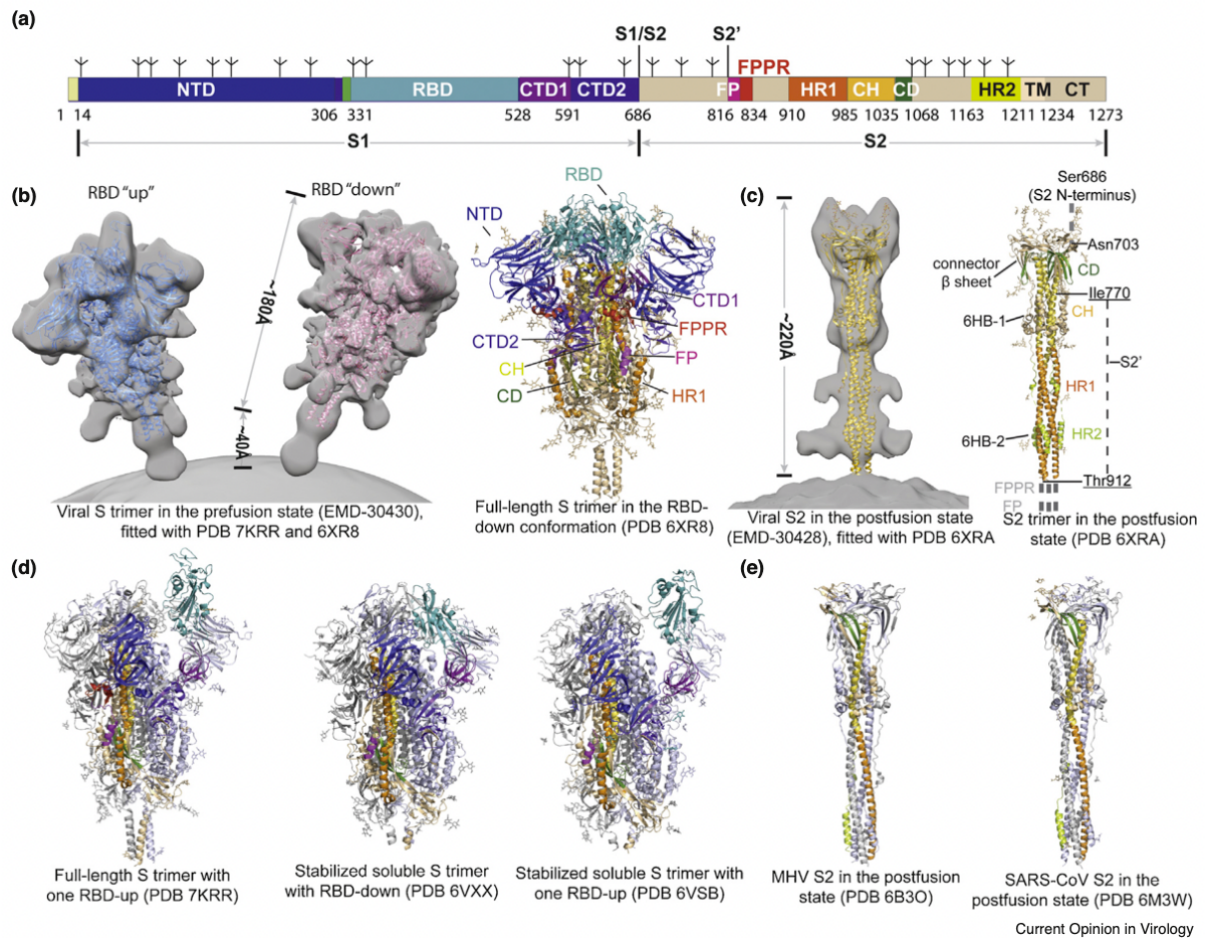


Figure 1.1. Distinct conformational states of the SARS-CoV-2 spike protein.

The following is worth noting about the picture above: (a) Schematic representation of the SARS-CoV-2 spike protein organization. S1 and S2 group consist of: NTD, N-terminal domain; RBD, receptor-binding domain; CTD1, C-terminal domain 1; CTD2, C-terminal domain 2; S1/S2, S1/S2 cleavage site; S2', S2' cleavage site; FP, fusion peptide; FPPR, fusion peptide proximal region; HR1, heptad repeat 1; CH, central helix region; CD, connector domain; HR2, heptad repeat 2; TM, transmembrane anchor; CT, cytoplasmic tail; and tree-like symbols for glycans. (b) on the Left: viral SARS-CoV-2 S trimer in the specific prefusion conformation (EMD-30430; Ref. [186]), completed with the purified protein structure (PDB ID: 7KRR and 6XR8; [175,186]). On the right side: cryo-EM structure of the full-length S trimer in the RBD-down conformation (PDB ID: 6XR8). (c) Left: viral SARS-CoV-2 S2 trimer in the postfusion conformation (EMD-30428; Ref. [177]), fitted with the structure of the purified protein (PDB ID: 6XRA; Ref. [175]). Right: cryo-EM structure of the full-length S2 trimer in the

postfusion conformation (PDB ID: 6XRA). (d) Additional structures of coronavirus S proteins, including the full-length SARS-CoV-2 S trimer carrying G614 in the one RBD-up conformation (PDB ID: 7KRR), the stabilized soluble SARS-CoV-2 S trimer in the RBD-down conformation (PDB ID: 6VXX; Ref. [169]), the stabilized soluble SARS-CoV-2 S trimer in the one RBD-up conformation (PDB ID: 6VSB; Ref. [168]). (e) MHV (mouse hepatitis virus) S2 in the postfusion state (PDB ID: 6B3O; Ref. [188]), and SARS-CoV S2 in the postfusion state (PDB ID: 6M3W; Ref. [187]).

Several 3D structures of spike protein fragments derived from the Wuhan-Hu-1 strain, including the S ectodomain which is stabilized in its prefusion state [168,169], RBD-ACE2 complexes [170-173], and segments of S2 in the postfusion state [174], were explored in the very beginnings of the pandemic. Later, full-length S proteins in both prefusion and postfusion conformations were identified by scientists [175,176], as well as those of the intact S trimer on the virion surface, studied by cryo-electron tomography [177-180], were also noted (Figure 1b and c). In general, the structure of spike protein of the SARS-CoV-2 shows many similarities to those of other coronavirus spike proteins [181-185]. In the prefusion structure, the S1 segment, adopting a 'V' shaped architecture with the NTD at one arm and the RBD, CTD1 and CTD2 at the other (also see Figure 2a), which fall around the central helical bundle formed by the prefusion S2 segment, illustrating the N-terminal end of HR1 toward the viral membrane. S trimer apex is formed by the three RBDs, creating two different conformations 'up' introducing a receptor-accessible state and 'down' representing a receptor-inaccessible state (Figure 1b). The three NTDs are navigated at the periphery of the trimer, each of them are in contact with the RBD from the adjacent protomer. The CTD1 and CTD2 pack underneath the RBD against S2 and between the two neighboring NTDs, showing they could modulate these domains and act an important role in the structural rearrangements required for membrane fusion.

In the postfusion state, S1 acts as a monomer, while S2 adopts a baseball bat rigid shape ($\sim 220 \text{ \AA}$ long), and the HR1 and CH turn over to form a continuous long helix together, which will be surrounded by short helices and famous β -sheets at the distal end of the membrane (Figure 1c and e). The connector domain (CD), together with a segment (residues 718–729) in the S1/S2–S2 fragment, form a three-stranded β sheet, and residues 1127–1135 join the connector β -sheet to expand it into four

branches. Three helical regions are locked by two disulfide pack against the slot of the CH part to form a short bundle structure with six helices (6HB-1). One turn helical state is adopted by the N-terminal region of HR2 and packs against the slot of the HR1 coiled coil; a longer helix is formed in the C-terminal region of HR2 that makes up the second six-helix bundle structure with the rest of the HR1 coiled coil (6HB-2) [175,187,188].

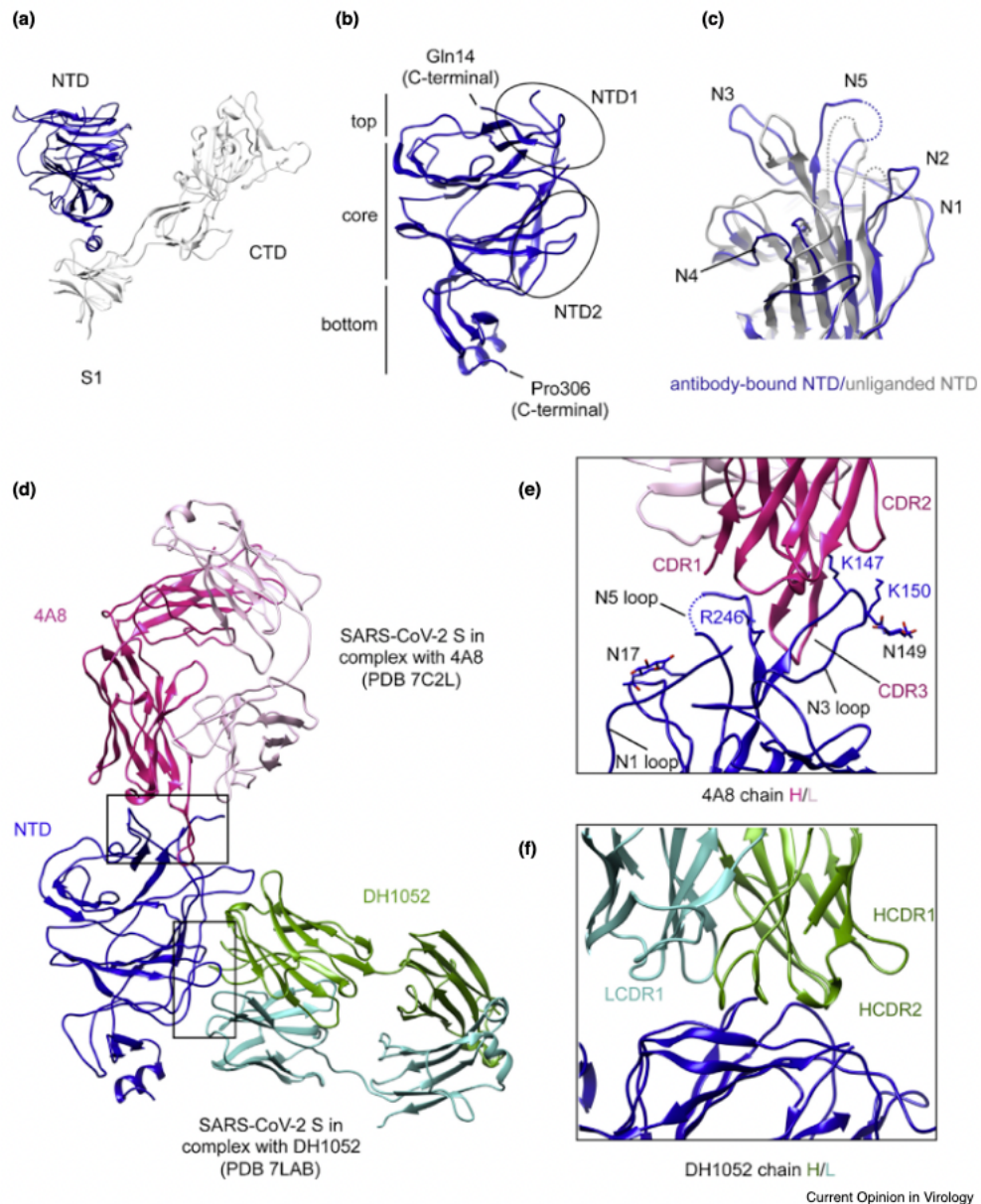


Figure 1.2. Structures of NTD and its antibody complexes [216].

About the picture above: (a) Cryo-EM structure of S1 segment from the SARS-CoV-2 full-length S trimer (PDB ID: 6XR8), the NTD is highlighted in blue and the S1 is in gray. (b) Close-up view of the NTD in the SARS-CoV-2 S protein. (c) The NTD (in blue) superposed with the domain from the full-length S trimer in gray and from its complex with 4A8, five surface loops are illustrated then (N1–N5). (e) and (f) Close-up view of the binding interface for the NTD-4A8 and NTD-DH1205 compounds with contacting residues in the NTD highlighted in sticks. (d) Superposition of the structures of the NTD in complex with antibody 4A8 Fab (PDB ID: 7C2L; Ref. [191]) and DH1052 Fab (PDB ID: 7LAB; Ref. [195]), as indicated. Heavy and light chains of 4A8 are colored in red and pink, respectively, and those of DH1052 are in green and cyan, respectively.

1.3. *N-terminal domain*

The NTD projects away from the threefold axis at the periphery of the spike protein (Figure 1b) [175], and can be sub-divided into the top section, and bottom regions (Figure 2b). The core structure is made of a galectin-like antiparallel β -sandwich fold, formed by one six-stranded β -sheets and the other with seven branches. The top section includes two antiparallel β -sheets which by a short loop are connected, while the bottom region is primarily made of a helix and two short β -sheets. The overall structure of the NTD is covered by eight N-linked glycans and similar to that of the S proteins from Middle East respiratory syndrome corona-virus (MERS-CoV) [189] and bovine coronavirus [190]. Although the exact function of the NTD in SARS-CoV-2 S remains undiscovered, NTDs of other coronaviruses have been shown to recognize sugars within the first attachment or specific protein receptors or play a role in the prefusion to postfusion transition [190]. However, antibodies which neutralizing NTD-targeted (nAbs), with a potency at the nM level, have been isolated from SARS-CoV-2 infected patients [191], offering a functionally vital role of this domain. High resolution 3D structures of the Spike protein in complex with NTD directed neutralizing antibodies (4A8, FC05, CM25, 4-18, S2M28, and DH1205) have been determined [191-195], reporting that these antibodies primarily bind to two glycan-free surfaces of the domain, designated NTD-1 and NTD-2 regions, respectively (Figure 2b; Ref. [196]).

NTD-1 region is being targeted by most antibodies, which thus named the NTD-1-antigenic supersite. It is navigated at the edge of the NTD top region, consisting five surface loops: N1 (residues 14–26), N2 (residues 67–79), N3 (residues 141–156), N4 (residues 177–186), N5 (residues 246–260) (Figure 2c), and a b-hairpin structure near N3, surrounded by four N-linked glycans (Asn17, Asn74, Asn122 and Asn149). These loops restate upon binding to different antibodies (Figure 2c). In the S-4A8 complex structure (Figure 2d) [191], the third complementarity illustrating section (CDR3) of the 4A8 heavy chain inserts to a cleft which is created by the N3 b-hairpin loop and N5 loop, while the CDR1 and CDR2 are in contact with the tips of the two loops. Moreover, the glycan at Asn149 is too close to the interface and may also help to elevate the binding of antibody (Figure 2e). Other antibodies, such as S2M28, 4-18, DH1050, CM25, FC05, 12C9 [196], also use their CDR1-3 to contact the N3 and N5 loops, but some interact with the nearby N1 loop or the glycan at Asn17 as well. Despite the the deafferent binding poses among these antibodies, their interface with the NTD-1 is highly conserved. Till now, NTD-2 is recognized by non-neutralizing antibodies, such as by DH1052 and 81D6 [196]. The CDR loops of both heavy and light chains in DH1052 interact with the surface organized by residues spanning in the range of 27–32, 59–62 and 211–218 in the NTD (Figure 2f), with possible involvement of the glycan at Asn603 of the CTD-2. Not surprisingly, the newly emerged SARS-CoV-2 variants of concerns, including Alpha (lineage B.1.1.7), Beta (B.1.351), Gamma (B.1.1.28) and Delta (B.1.617.2), all have mutations and/or deletions within the NTD-1-supersite, rendering resistance to neutralization by directed NTD antibodies [197,198].

1.4. Receptor binding domain

The RBD includes two subdomains which are a five-stranded antiparallel β -sheet connected by short helices and loops, and an extended loop, named receptor binding motif (RBM) [170,171,199]. In the human host cell, ACE2 is an important component of renin angiotensin system (RAS) and elevate the hydrolysis of angiotensin II to angiotensin 1–7 [171]. The full-length human ACE2 is also a chaperone of the amino acid transporter BAT1 and forms a homodimer mediated by its neck domain in the presence of BAT1 (Figure 3a) [172]. Cryo-EM structures of the soluble uncleaved Spike protein in complex with monomeric ACE2 show that the S trimer has the capacity of binding, up to three ACE2s in the RBD up state (Figure 3b) [200,201]. The crystal

structure of the SARS-CoV-2 RBD ACE2 complex reveals a similar structure to the SARS-CoV RBD-ACE2 complex [170,171]. A nicely concave outer surface of the extended RBM interacts with the N-terminal helix of the claw-like peptidase domain (PD) of ACE2 (Figure 3c) [170-172]. Between a series of polar residues, such as K417, E484, N487 and N501 of the RBD and D30, K31, H34, Y41 and K353 of the ACE2 which contain hydrogen bonds and salt bridges, dominate the RBD-ACE2 interaction (Figure 3c) [170-172]. There are additional hydrophobic interactions between F486 of the RBD and L79, M82 and Y83 of the ACE2 which contribute to the receptor engagement (Figure 3c) [170-172]. Upgraded affinity for ACE2 and immune evasion is powered by mutations of the key residues, such as N501Y, K417N and E484K, which have been identified in the fast-spreading variants of concern [202,203].

The RBD is a dominant target of nAbs elicited by either natural infection or vaccination, emphasizing its vital role during infection [204,205]. The RBD directed nAbs can recognize several different epitopes, alarming great potencies at the pM-nM level in vitro neutralization assays (Figure 3d) [205]. The nAbs that target the ACE2 binding site, such as REGN10933, C144 and S2H14, directly compete for ACE2 association [204-207]. Those recognizing the non ACE2 binding site, such as REGN10987 and C135, probably prevent ACE2 binding either by clashing with ACE2 or by blocking the transition of the RBD from the 'down' to the 'up' state [205-207]. The dissociation of the S trimer can be caused by other nAbs against the so called 'cryptic supersite', like CR3022 and S304, which destabilize the S trimer [204,205,208]. Although a high potency of this class of antibodies makes them promising therapeutic agents, however the resistant variants could possibly limit the clinical applications of these agents for treating the COVID-19.

The human ACE2, named APN01, is under evaluation as a therapeutical treatment for COVID-19 in a second phase clinical trial, based on the favorable results from a previous phase 1 trial [209], and evidence that the protein blocks SARS-CoV-2 infection effectively in vitro [210]. Other ACE2 based fusion inhibitors have been developed with optimized binding and potency comparable to those of the nAbs [200,211,212]. The ACE2 is constructed with multivalency, such as the dimeric protein sACE2_{2.v2.4}- IgG1 including the mutation T27Y/L79T/N330Y and the trimeric protein ACE2 foldon T27W, potentially are able to inhibit the viral infection with a potency 1000

fold and 1700 fold higher than that of the monomeric soluble ACE2 with the wildtype sequence [200,211]. Further stabilization of the binding interface through non-polar interactions with residues Y489, F456 and Y473 of the RBD (Figure 3c) can be reached by substitution of T27 with an aromatic residue. To be added, a series of miniproteins, created using computer generated scaffolds to mimic the N-terminal helix of ACE2, can bind the RBD and inhibit viral infection at a concentration below the nM level [212]. These ACE2 derived inhibitors may show even higher affinity to those SARS-CoV-2 variants that have gained increased receptor binding than the Wuhan-Hu-1 virus. Nonetheless, further validation is required for pharmacokinetics, in vivo efficacy and safety profile of these new designs.

1.5. C-terminal domains

The C-terminal domains (CTDs) are formed primarily by β -structures of segments from S1, as well as the N-terminal segment of S2 adjacent to the furin cleavage site (Figure 4). CTD1 contains two antiparallel β -sheets, with two strands and four strands, respectively. CTD2 also has two β -sheets: a four-stranded one and another four-stranded one that includes a strand from the S2 subunit [168,169,175,186]. In the RBD-down conformation of the S trimer, a structural element in the CTD2, named the '630 loop', becomes well-ordered in the G614 variant while disordered in the Wuhan-Hu-1 strain [175,186]. When structured, the 630 loop inserts into a gap between the NTD and CTD1 of the same protomer, stabilizing the CTD2 structure. It is also located in the vicinity of the S1/S2 boundary as well as the FPPR of a neighboring protomer [186]. The FPPR and the 630 loop help retain the RBDs in the down conformation but move out of their positions when the adjacent RBD flips up. Thus, the CTDs, together with the FPPR and the 630 loop are key components of the S fusion machinery that modulate the fusogenic structural rearrangements of S protein.

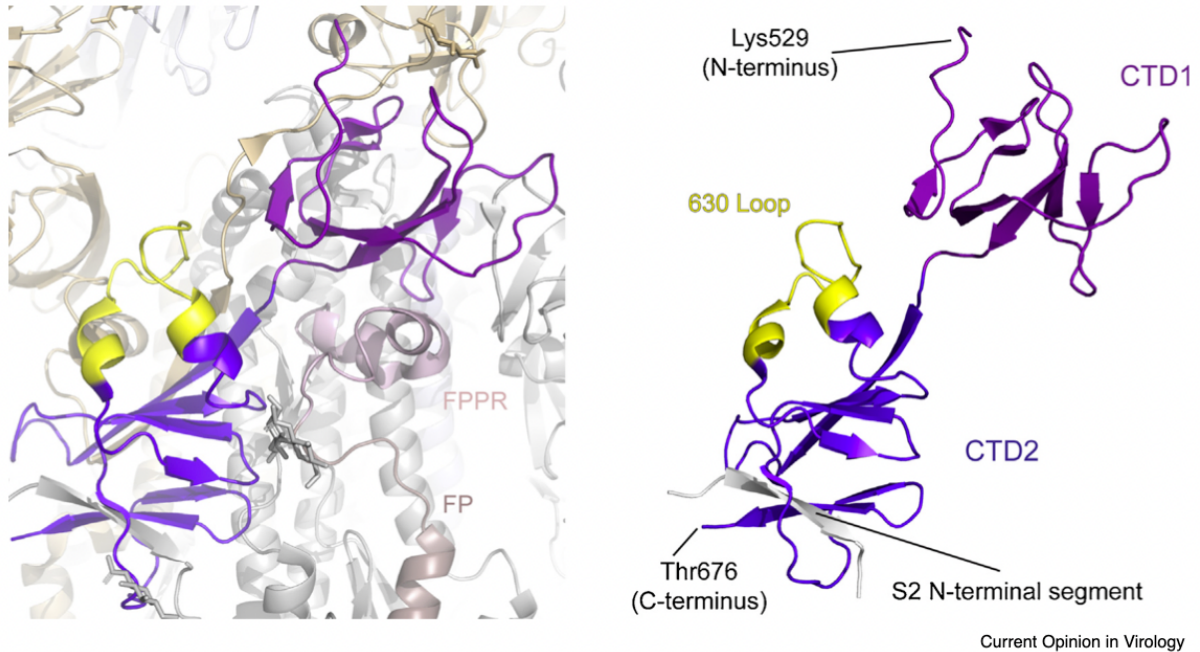


Figure 1.3. Structures of CTDs [216].

The full-length S trimer is formed by structures of CTDs (PDB ID: 7KRQ; Ref. [186]) are shown, with CTD1 in magenta, CTD2 in purple, the 630-loop in yellow, and the β strand in the CTD2 from S2 subunit in gray.

1.6. S2 structure

Three S2 sub sections are tightly pack around a central three stranded coiled coil of 140 Å long in the perfusion conformation [175] and formed by CH (Figure 1b). Portion of the HR1 together with another fragment of S2 (residues 758– 784) adopt a-helical state and finally create a nine helix bundle with the central coiled coil, which is the most rigid part of the S trimer. The CD region connects CH and the C-terminal HR2 by a linker region (Figure 5a). The FP creates a short helix and tucks in a pocket formed by two neighboring S protomers. If the RBD moves up and thus appears to help clamp the perfusion S trimer in the closed the structured FPPR clashes with the CTD1, RBD down state. It has also been suggested to function as a pH-dependent switch domain that modulates the RBD position [201]. The remaining HR2, TM and CT segments are disordered in the most S trimer structures, but report low resolution density in the cryo-ET reconstructions that can be tilted away from the threefold axis of the trimer with the angle spans from 17 to 60 [178].

In the postfusion state [175,187], the HR1 and CH create a continuous helix and three copies of them derive a long central three stranded coiled coil of 180 Å (Figure 5a). To stabilize the prefusion conformation two proline substitutions at the boundary between the HR1 and CH prevent formation of the postfusion helix, and such a design has been used for structural studies and the first-generation vaccines [168,169,213]. Small section of the HR2 folds into a helix and packs against the slot between two HR1-CH helices to create a six-helix bundle structure, reminiscent of the postfusion organization of other viral fusion proteins [214,215]. From the prefusion conformation the CD remains unchanged, as a three-stranded β-sheet evolving the C-terminal end of HR1-CH helices. In Comparison between the prefusion and postfusion states of S suggests that HR1 experiences large rearrangements to form a coiled coil, translocating its N-terminal end by a long distance to guide the FP towards the targeted cell membrane (Figure 5b). In addition, the HR2 and the TM at its C-terminal end must fold back to pack along the slot of the HR1-CH coiled-coil to create the postfusion six-helical bundle (Figure 5c). These refolding actions effectively bring the viral and target cell membranes in contact, ultimately leading to membrane fusion (Figure 5d). Five N-linked glycans cover the postfusion S2 surface along the long axis with a regular spacing and may protect the S2 from the host immune reactions.

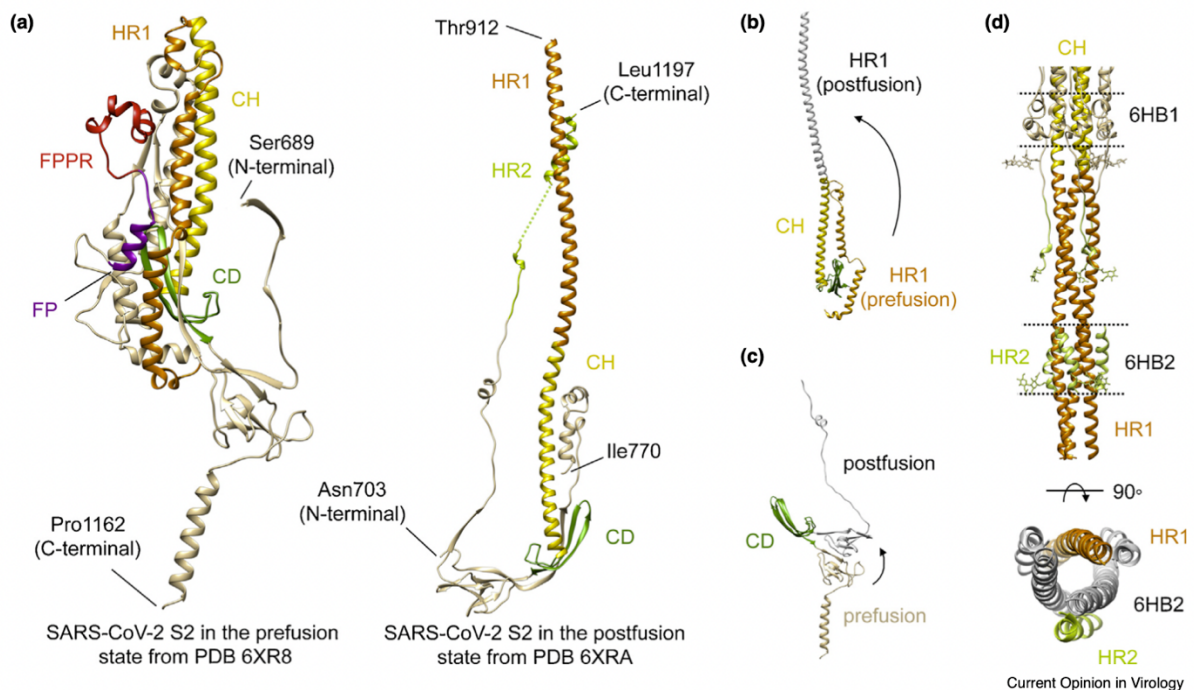


Figure 1.4. Structures and proposed conformational changes of SARS-CoV S2 [214].

Regarding the structural variations of SARS-CoV: (a) Close-up view of S2 in the prefusion (left) and postfusion (right) conformations from PDB ID: 6XR8 and 6XRA, with the fusion peptide (FP) highlighted in purple, the FPPR in red, central helix (CH) in gold, connector domain (CD) in green, HR1 in orange and HR2 in green. (b) Proposed structural transition of the HR1 from the prefusion to postfusion conformation. (c) Proposed conformational change of the HR2. (d). Six-helix bundle structures in the postfusion S2 with HR1 in orange and HR2 in green.

1.7. Mutation:

The virus SARS-CoV-2 arose in China and rapidly propagated leading to the COVID-19 pandemic of 2020. With the awareness of this public health disaster, the evolutionary fate of the virus becomes a matter of the utmost concern [154-157]. Its evolutionary change is likely to impact key functionalities associated with transmission efficacy and severity, bearing directly on the course of the pandemic. Korber et al. provided epidemiological evidence that the amino acid substitution D614G in SARS-CoV-2 spike protein is rapidly becoming dominant, suggesting that the G614 mutant may entail a significant fitness advantages. Since the spike (S) protein mediates the viral recognition of the host receptor (angiotensin-converting enzyme 2, hACE2) as well as the fusion of viral and cellular membrane, it becomes imperative to find out how this mutation affects viral transmission and infectivity. Korber et al. argued that the rapid spread of the G614 mutant is related to higher infectivity. To support this hypothesis, they showed that the G614 variant yields higher titers in pseudoviruses from in vitro experiments. These results appear to be corroborated by other groups [155,156]. In infected individuals, the variant G614 is likely to cause higher upper respiratory tract viral loads, yet the severity of the disease does not appear to increase. These findings prompt a mechanistic assessment of the impact of the S-protein mutation on virus transmission as a guidance to steer the development of novel immunological cures.

1.8. Transmission efficiency of SARS-CoC-2 G614 Variant:

S^{D614} and S^{G614} are the most competing phenotypes which were recently characterized and compared [157]. That analysis reported that retroviruses pseudotyped with S^{G614} infected human ACE2 expressing cells significantly more efficiently than those with S^{D614} . To understand better the results, it is first noted that the S protein is formed as a trimer with each monomer including two tethered and mutually in contact domains S1 and S2, the first involved in receptor binding (RB) through its RBD domain, while S2 elevates the fusion of viral and cellular membranes [154]. The higher transmission efficiency of the G614 mutation is proven not to associate with higher epitope affinity or binding efficacy but with less S1 shedding and higher incorporation of the S protein into the pseudovirion, pointing to a higher stability of the S^{G614} phenotype[157]. Since the S1 residue 614 is close to the S2 domain in the S-protein quaternary structure, Zhang et al. first compared the ratio between the S1 and S2 domains in the virion that could possibly signal altered release or shedding of the S1 domain after cleavage at the S1/S2 junction. The resulting S1:S2 ratio is markedly greater in PV^{G614} compared with PV^{D614} , concluding that G614 stabilizes the interaction between the S1 and S2 domains, that limits S1 shedding.

1.9. Structural and mechanistic impact of the D614G mutation:

A structural analysis of effects of the D614G substitution on the S1/S2 interface supports this belief, while as shown subsequently, the analysis needs to go beyond the structural assumption and analyze the relationship between structure and enveloping solvent, the so called epistructure [158] It has been postulated [154] that the carboxyl group in D614 creates a hydrogen bond with the hydroxyl group in T859 which exists in the S1/S2 interface. The crystal structures of the complex reject this beliefs since the side chain groups are not nicely organized for hydrogen bonding (Figure 1.5a). Furthermore, This hypothesis is totally incompatible with the findings of the experiment of Zhang et al. since the D614G mutation would totally eliminate the hypothesized hydrogen bond across the S1/S2 interface; hence, the S^{G614} phenotype would be characterized by more S1 shedding compared with S^{D614} . The experimental evidence favors accurately the opposite conclusion [157]

The epistructure of the interacting S1 and S2 domains is taken into consideration in a more detailed examination of the effects of the D614G mutation. The pre-bonded D614-A647 backbone hydrogen (BHB) is partially in contact with the solvent (Figure 1b), and Dehydron is a specific type of packing flaw which results from this [158-160] in the S1 domain. In a thermodynamic point of view, the dehydron is an adhesive spot promoting removal of surrounding water [160,161] for two mutually empowering reasons: [158-160] (a) the preformed BHB gets stabilized when a protein association (i.e., S1/S2 interaction) causes removal of surrounding water thereby hindering the structurally disruptive hydration of amide and carbonyl (destabilizing the unbound state is tantamount to stabilize the bound state), and (b) the removal of backbone-solvating water molecules at the dehydron site is favorable because the partial confinement of such water molecules curtails their hydrogen bonding coordination possibilities; therefore, their transference to the bulk becomes thermodynamically supported [161] An energetic perspective can also be used to justify the dehydron adhesiveness, because the surrounding water molecules are eliminated together with the partial charges screened by the BHB, the BHB is strengthened. [160]

Dehydrons generally undermine the protein structure's stability by exposing it to disruptive backbone hydration and encourage protein interactions to block out surrounding water. [158-160]. Exogenous withdrawal of water from the dehydron milieu increases and stabilizes the electrostatic connection that underlying the BHB, turning dehydrons into determinants for protein attachment. This theory is accepted by bioinformatics data on the distribution of dehydrons at protein complex interfaces, which highlights dehydrons as significant forces behind complex formation [160]. A descriptor is created and called wrapping that assesses the reliance on binding partnerships to sustain local structural integrity to identify dehydrons in the protein structure. [159,160]. The underwrapped BHB that is a dehydron has inadequate side-chain nonpolar groups crowded around it, leaving it susceptible to structure-disruptive hydration. Direct computation of dehydrons and wrapping from structural coordinates is possible. [160]. The extent of hydrogen-bond wrapping determines how many side chain nonpolar groups are contained inside a "desolvation domain" (two intersecting balls centered at the paired residues' -carbons), which in a reported structure defines the BHB microenvironment. As a result, in a structural database, dehydrons are found towards the tail of the distribution of wrapping values across BHBs. [160]

The D614-A647 BHB in our case is an intramolecular dehydron surrounded by the residues D614, A647, V615, T645, and R646. (Figure 1b). When this residue creates a salt bridge with D614 it achieves the greatest wrapping from R646 (Figure 1c). The salt bridge D614-R646 helps to stabilize BHB D614-A647 in the uncomplexed S1 and prevents the S1/S2 connection in this way. The salt bridge is dissolved as S1 and S2 become connected (it is absent in PDB structure 6VXX, as expected), and the dehydron D614-A647 completes its intermolecular wrapping with assistance from P862 from the S2 domain (Figure 1d). The substitution D614G has a major impact on the epistructure of S1, vis-a-vis the previous considerations. The effect results from two contributions: (a) In addition to improving the wrapping of the dehydron pairing residues at positions 614 and 647, mutation D614G eliminates the salt bridge that interferes with the S1/S2 association. (b) The mutation makes the dehydron G614-A647 a better promoter of the S1/S2 interaction by decreasing the dehydron-wrapping contributions from side chains at positions 614 and 646, which makes the uncomplexed S1 domain unstable. The structural stability of the 614-647 BHB is more dependent on the contribution from P862 upon S1/S2 interaction in the G614 mutant (Figure 1d).

The thermodynamic cost of destabilizing the S1 structure as a result of depriving the BHB 614647 of three wrapping carbonaceous groups due to the D614G substitution is calculated using conservative estimates derived from experimental data on the cost of unwrapping the BHB, which yields $3.8 \text{ kJ/mol} = 5.73 \text{ kcal/mol}$. The lost wrapping contributions include one methylene group from the D \rightarrow G substitution proper and two methylene groups from R646 that no longer can form the salt bridge with the glycine at position 614 (Figure 1.5c). Because of this, the D614G mutation has a considerable effect on the S1/S2 complex's stability, which can be conservatively calculated as $\Delta G = 5.73 \text{ kcal/mol}$. It worth to be notede that the stabilization of the S1/S2 complex arises from the destabilization of the free S1 structure. [162]

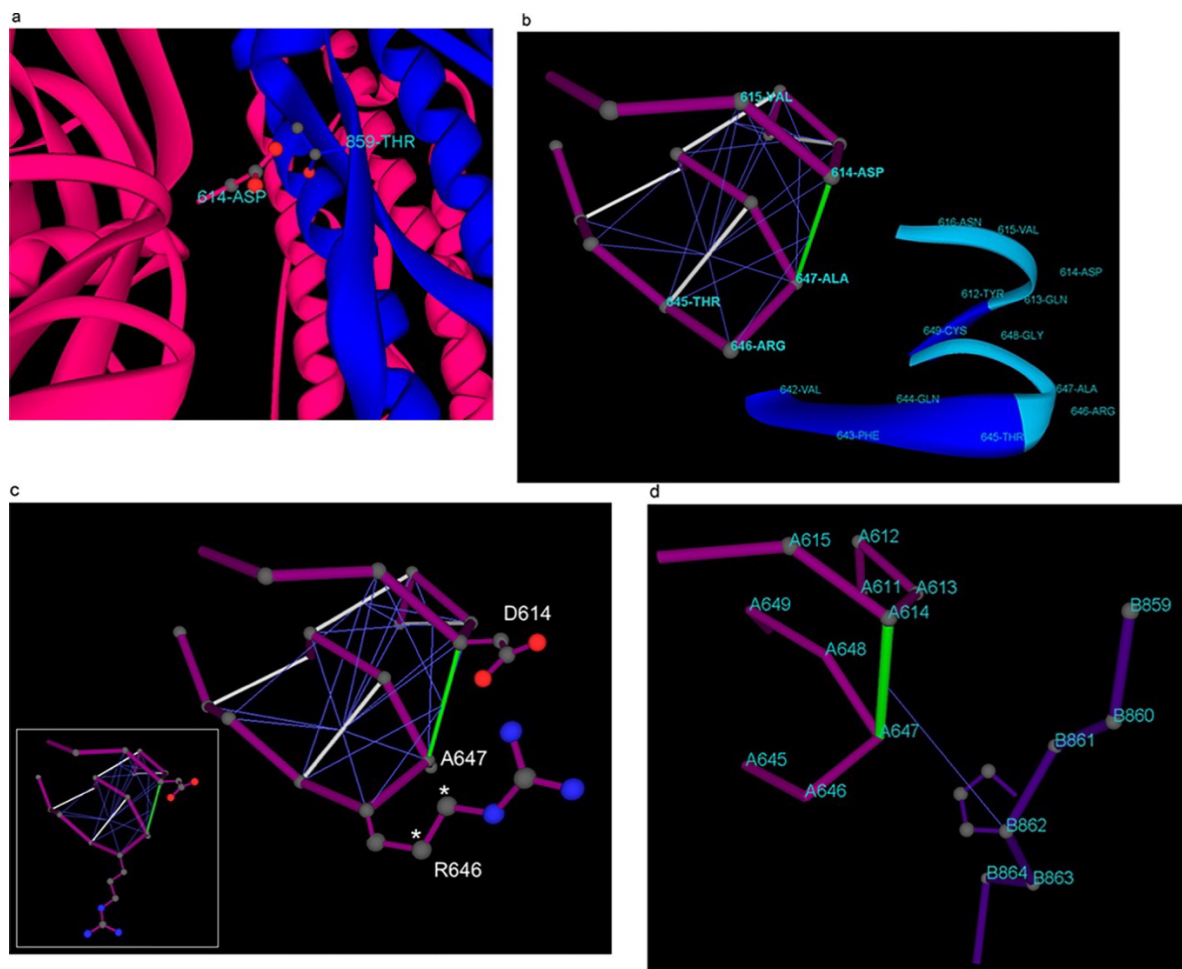


Figure 1.5. Structural and epistatistical interactions at the S1/S2 interface in the spike protein of SARS-CoV-2 [217].

About the structural interaction of two chains S1 and S2: (a) The spike protein structure published in PDB6VXX shows the location of D614 in the S1 chain (magenta) in relation to T859 in the S2 chain (blue) at the S1/S2 interface. The protein backbone is rendered in ribbon representation. (b) Intramolecular wrapping of backbone hydrogen bonds (BHBs) around dehydron D614-A647 for the S1 chain. A polygonal (magenta) representation of the protein backbone is shown, with lines connecting the α -carbons of succeeding residues. The dehydron is depicted in green, while well-wrapped BHBs are indicated as gray lines linking the α -carbons of paired residues. Thin blue lines connecting the bond's core to the residue's α -carbon, which provides side-chain nonpolar groups to the BHB's desolvation domain, represent the wrapping of each BHB. The ribbon rendering serves as a visual help. (c) Improved intramolecular wrapping of dehydron D614-A647 achieved by forming the D614-R646 salt bridge. In

this state, When it is compared to the fully hydrated R646 side chain that develops when S1 joins the S1/S2 complex, R646 adds two more side chain methylene groups (asterisks) to the wrapping of the D614-A647 BHB. (inset). (d) Intermolecular wrapping of dehydron D614-A647 by P862 across the S1/S2 interface. According to PDB 6VXX, the chains are identified as A and B, which correspond to S1 and S2, respectively.

1.10. Competitive Structural advantages of D614G mutation:

An investigation of the D614G mutation's potential effects was driven by the sequences with the mutation's reported rise in dominance over the Wuhan S sequence. The D614G mutation is proximal to the S1 cleavage domain. Monomer of SARS-CoV-2 is presented in the Figure 1.6 which is taken from PDB ID: 6VSB [144] is shown. The full Cryo-EM structure of the trimer has only medium resolution. It is worth to notice to the fact that the PDB:6VSB structure is missing 673-686. Thus, the structure of the furin cleavage domain, 682- RRARS-686, remains unknown. The D614G mutation, however, would be roughly 24 angstroms from the S1 cleavage domain in this depiction based on the position of amino acids bracketing the furin cleavage domain.

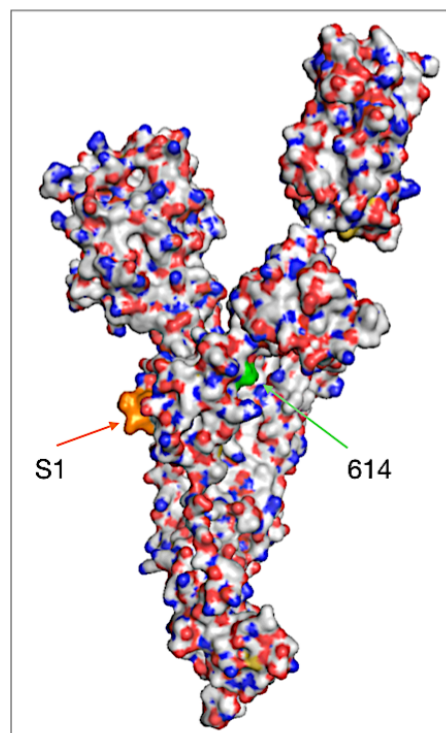


Figure1.6. Surface representation of the SARS-Cov2-S protein [216]

Space filling representation illustrating the general position of the furin cleavage domain (orange) and D614 (green). The D614G mutation is estimated to induce a structural variant in the Furin cleavage domain. The protein region from AA S591 to N710 is modeled using I-TASSER [145,146] multiple sample threading methodology. Modeling is performed using SARS-CoV spike protein PDB ID: 5X58 [147] as the main sample. With the strongest homology to SARS-CoV-2, this structure is the highest resolution PDB structure. Because it contains both the D614G mutation site and the furin cleavage site with distinct secondary structure close to the two sites, the AA region of 591 to 710 is chosen for investigation. The exact same threading method is used for both the Wuhan S and D614G mutation sequences with the only variation in the sequence of the 2 models being D614 to G614, referred to below as D614 and G614, respectively. The Template Modeling Scores (TM-Score) for the D614 and G614 models were 0.59 and 0.58, respectively. A model with a TM-Score higher than 0.5 indicates a model with correct and accurate topology [148].

Figure 1.7A shows a ribbon introducing the AA 591 to 710 region of the D614 and G614 models. By inspecting the 2 structures, it is observed that the five residues in the furin polybasic cleavage domain (RRARS, R682– S686) are 22 angstroms from AA614 in these models. Comparison of the two models clearly shows the furin cleavage domain has the highest rate of changes in secondary structure within AA 591 to 710. The G614 model shows a more compact alpha helical structure while the D614 model has a more random coil. This finding is supported by analysis using the Kabsch and Sander algorithm [149] to define the secondary structure of proteins (KSDSSP) shown in Figure 1.7B. KSDSSP uses the position of the backbone atoms of a protein to identify which residues are in alpha helices and beta strands based on hydrogen bonding interactions. An alpha helix in the furin cleavage domain is estimated for G614 but is missing in the D614. Thus, I-TASSER and KSDSSP both estimate an alpha helical configuration in the furin cleavage domain for G614 that was absent for D614. Additionally, I-TASSER and KSDSSP identified no more major changes in secondary configuration. It is compelling that the model showed the greatest conformation change induced by D614G mutation in a functionally relevant location (e.g., furin polybasic peptide domain).

The hydrogen bonding network alters when the acidic side chain of aspartate at position 614 is swapped for the hydrogen atom of glycine, generating an alpha helical structure 22 angstroms away from AA 614.

The D614G mutation alters the orientation of vital residues in the furin cleavage domain. The minimal sequence requirement for furin catalysis of a cleavage site is RXXR*X where * indicates the site of amide hydrolysis C-terminal to the recognition site [150]. For the S1 domain of SARS CoV-2 it has been reported that furin cleaves between R685 and S686, at the C-terminus of the consensus furin recognition domain 682-RRAR*S -686 [151]. Catalysis is successfully done by placement of arginines at the P1 (R685) and P4 (R682) positions of the substrate into the corresponding binding pockets of furin [152].

The cleavage domains for D614 and G614 are aligned using Pymol with the 3D structure of an active inhibitor (Meta-guanidinomethyl-phenylacetyl-RVR). A high resolution crystal structure of the inhibitor bound into the furin catalytic domain PDB ID: 5XJH [152] was used for the alignment. Comparing the alignments of the D614 vs. G614 cleavage domain to the inhibitor (Fig 1.7) it is observed that the orientation of the G614 P1 and P4 residues is closer to the orientation of the P1 and P4 residues of the inhibitor structure compared to D614. The closer a substrate is to the transition state orientation, the lower the energetic requirement for cleavage [152, 153]. Therefore, the cleavage of the G614 including S protein is suggested to be energetically favored over the D614 containing S protein.

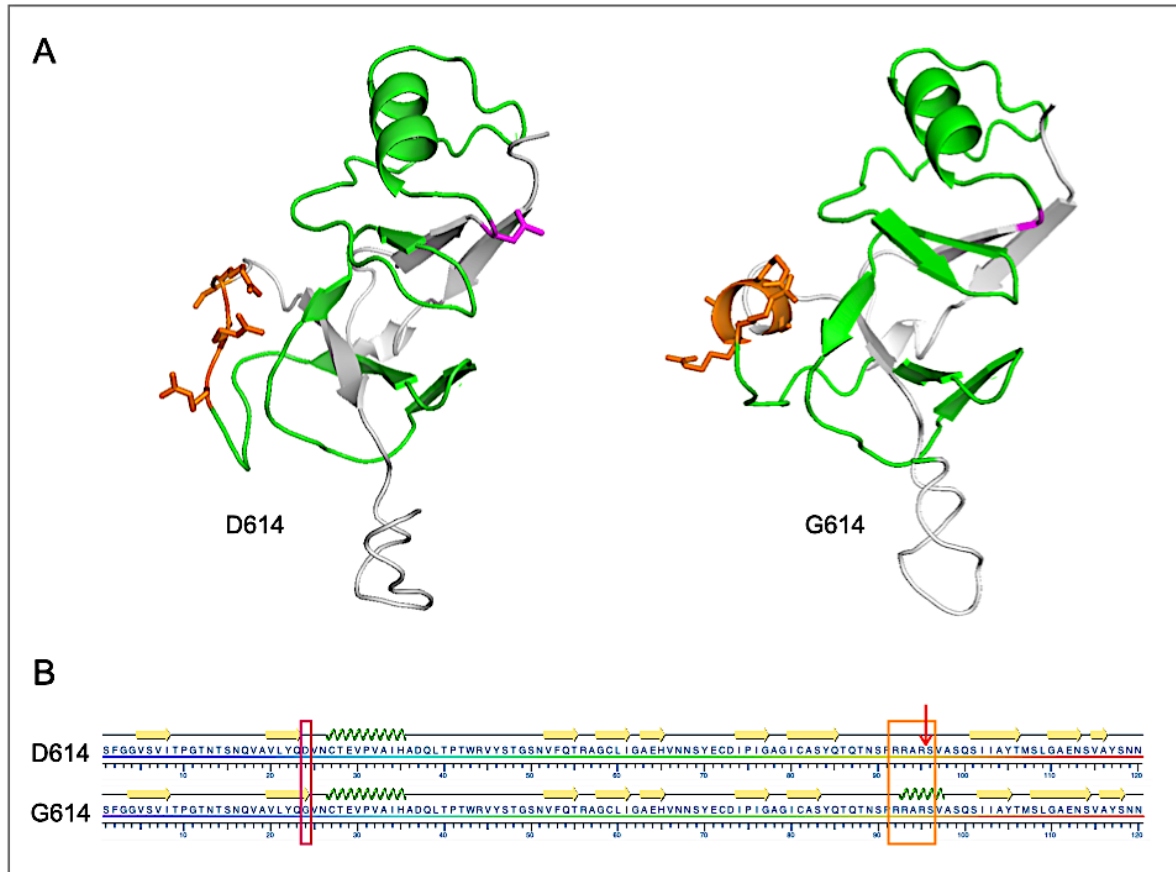


Figure 1.7. Structural representations of D614 and G614 SARS-CoV-2 S protein [150]

The above illustration (Fig. 1.7) is limited from S591 through N710. A. I-TASSER-derived models using SARS-CoV spike protein PDB ID: 5X58 as the basic sample. The furin cleavage domain 682-RRARS-686 is shown in orange and D614 (left) or G614 (right) are shown in magenta. Residues between 614 and the cleavage domain are shown in green. B. Results of the KSDSSP algorithm for defining secondary structure of proteins. The furin cleavage domain is marked with an orange box, the D614G mutation with a magenta box, and the cleavage site with an arrow. Beta sheet or alpha helix secondary structures are indicated by yellow arrows or green corkscrew, respectively.

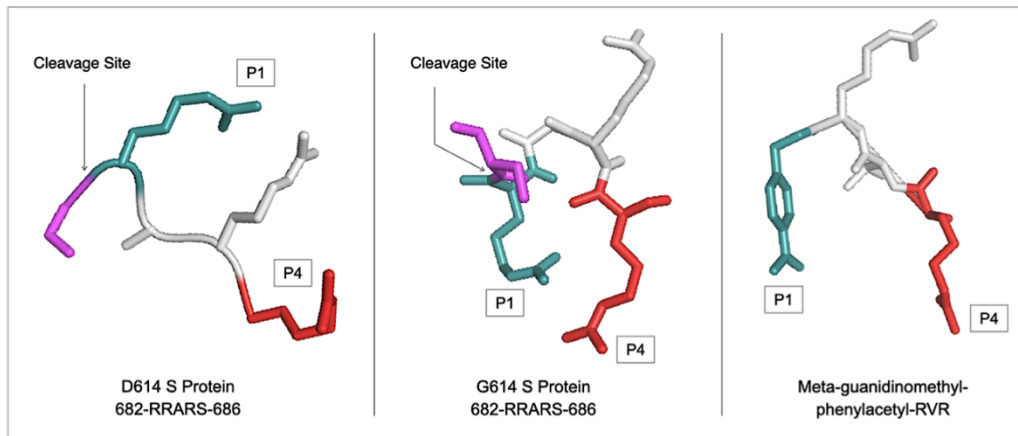


Figure 1.8. Alignment of models of the D614 and G614 cleavage domains with an active site inhibitor [153]

Teal and red, respectively, represent the P1 and P4 residues of the D614 and G614 cleavage domains and inhibitor. The magenta residue at the cleavage site is serine.

The D614G mutation more favorably aligns important residues in the furin active site. Using the model of furin and the inhibitor (PDB ID: 5JXH), the inhibitor aligned structures of D614 or G614, R682– S686, were substituted for the inhibitor in the furin catalytic domain using Pymol (Fig 1.9). G614 puts the necessary guanadino side chains, P1 (R685) and P4 (R682), into their respective enzyme pockets whereas the D614 only offers one or the other. This scenario would indicate a lower energy barrier for furin to cleave the S protein, which contains G614. Therefore, the D614G mutation's expected long-range conformational shift more favorably aligns crucial P1 and P4 residues into the furin binding sites. The D614G mutation may enhance cleavage of the S1 site on the S protein furin and thereby give an advantage to the G614 mutant for S protein processing.

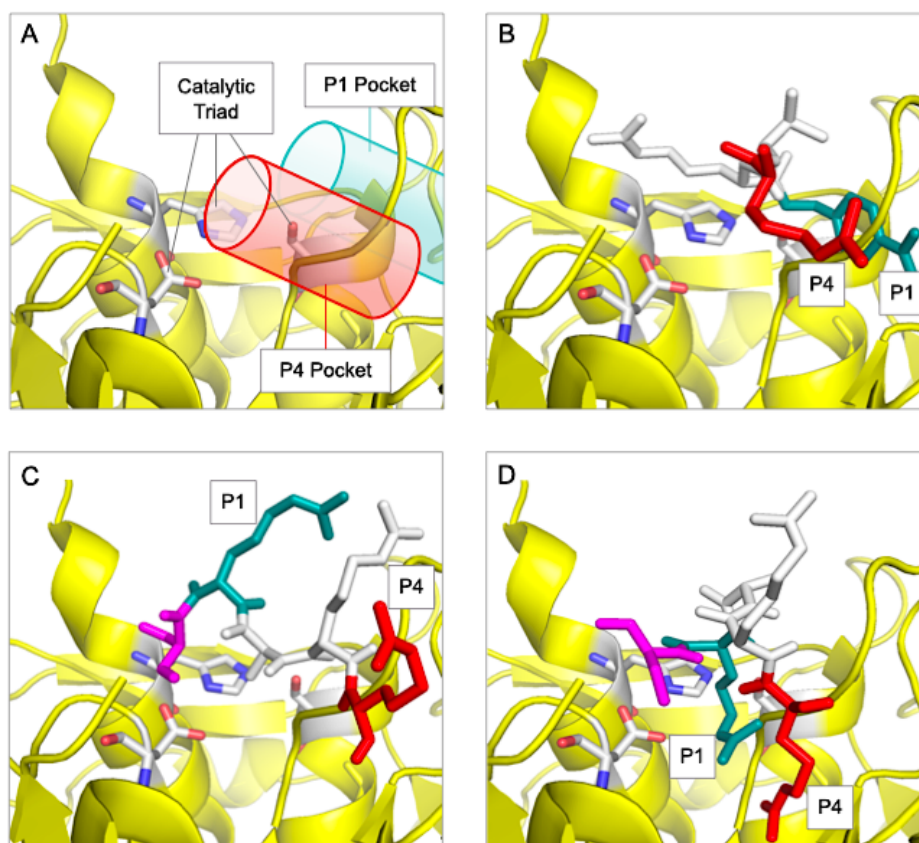


Figure 1.9. Alignment of D614 and G614 in the catalytic domain of furin

A. The catalytic domain of furin is shown in yellow (panels A-D) with the locations of the P1 (green) and P4 (red) binding pockets shown as cylinders. B. Alignments of Inhibitor, Meta-guanidinomethyl-phenylacetyl-RVR. C. D614 682-RRARS-686. D. G614 682-RRARS-686.

1.11. CD147:

As mentioned above, the primary determinant of coronavirus tropism is spike protein, which mediates the viral infection by binding to membrane receptors on the host cells [21]. A member of the immunoglobulin superfamily's type-I transmembrane glycoproteins, CD147 is sometimes referred to as basigin or EMMPRIN. CD147 was purified for the first time from the plasma membrane of the human LX-1 lung carcinoma cell line in 1982 [17]. This transmembrane glycoprotein is expressed widely in both humans and animals (e.g., rat, mouse, chicken). In humans, it is found expressed in various cells like platelets, fibroblasts, T-lymphocytes, plasmodium invasion, bacterial and virus infection but it is well known to be expressed in tumor cells so that scientists use the transmembrane glycoprotein as an identification factor of the tumor cells in humans [17,21].

CD147 glycoprotein has solid structures in human which generated by differential splicing and differences in transcription initiation sites. Retina specific form has been explored to have three domains as one of the isoform structures of CD147 also known as BSG-1 (1.10) The more common form of CD147, has been reported to have two domains also known as BSG-2 (Figure 1.10). The 3D structure of the extracellular portion of CD147 (BSG-2) is determined and widely reported in the protein banks data bases [64]. The transmembrane portion of this glycoprotein includes 23 amino acids which are highly conserved among species and members of the BSG family (BSG1, BSG2) [64].

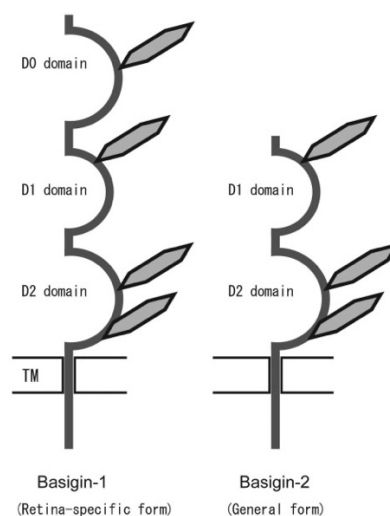


Figure 1.10. CD147 or basigin isoform [64]

1.12. Inflammatory responses of CD147:

In addition to its SARS-CoV-2 binding capability, CD147, a transmembrane glycoprotein receptor encoded in humans by the BSG gene [48], is of interest as a key mediator of inflammatory response, in particular, as related to vascular occlusion. In response to immunogenic stimuli, CD147 is upregulated in T cells [49,50], platelets [51,52] and endothelial cells [53], with upregulation of CD147 in endothelial cells occurring upon exposure to active or UV-deactivated betacoronavirus MHV-4 in vitro. CD147, in turn, has been observed to promote adhesion by RBCs [54–56], leukocytes [52,57–59] and platelets [57,58,60] to other blood cells and endothelial cells. Also, of particular interest are the indicated pro-infectious roles of CD147 and its binding partner cyclophilin A for SARS-CoV-2, SARS-CoV and other viruses [21,61–63]. In a broader clinical framework, the involvement of CD147 in the pathogenesis of a number of diseases, including lung inflammation, atherosclerosis, heart failure, ischemic myocardial injury and stroke [52,56,58,64,65], further suggests that CD147 antagonists or masking agents could mitigate a COVID-19 infection.

Interaction between ivermectin and spike protein at spike protein's binding sites: The potential for competitive binding to restrict such attachments has been one focus in the quest for repurposed COVID-19 therapies given that the attachment of the SARS-CoV-2 spike protein to host cell targets, including ACE2, SA, and CD147, is essential to viral infectivity and morbidity. [3]. Four molecular modeling studies that collectively screened over 800 such molecules were conducted toward that goal [66–69]. The strongest or close to strongest binding affinity in each study was obtained for ivermectin, a macrocyclic lactone with multifaceted antiparasitic and antimicrobial activity which has been distributed in 3.7 billion doses worldwide since 1987 [70–73]. Additional molecular modeling studies of competitive binding to SARS-CoV-2 spike protein sites that focused on ivermectin in particular likewise found strong binding affinities for that agent [74–79].

These findings are of interest given clinical, animal and epidemiological studies, including most of the 20 randomized clinical trials (RCTs) conducted to date, indicating the efficacy of ivermectin against COVID-19 [70,80,81], although interpretations of which of these RCTs are most reliable have been controversial. Ivermectin is suitable

for mass use on a global scale, having been the mainstay of two worldwide campaigns to eliminate two devastating scourges affecting millions, onchocerciasis and lymphatic filariasis [82]. It is safe even at much higher doses than the standard dose of 200 µg/kg [83,84], and its limited side effects were noted in the Nobel Committee's 2015 award honoring its discovery and its record of improving the health and wellbeing of millions [85]. However a biological mechanism that was initially put up for ivermectin efficacy against SARS-CoV-2, entailing blocking of its trafficking into the host cell nucleus, was questioned in connection with in vitro investigations carried out at considerably higher doses than normal. [86–88].

1.13. Nicotinic Acetylcholine Receptors:

Another biological mechanism of activity that may underlie the observed clinical benefits of ivermectin treatment of COVID-19 is a potent anti-inflammatory and immune modulatory effect mediated by its action as a positive allosteric modulator of the alpha-7 nicotinic acetylcholine receptor ($\alpha 7nAChr$) [89]. The core receptor of the cholinergic anti-inflammatory pathway is $\alpha 7nAChr$, which is under the control of the vagus nerve [90] and plays a crucial role in balancing of the body's response to inflammation and sepsis [90,91]. This anti-inflammatory pathway connects the involuntary parasympathetic nervous system innervating all major organs to cytokine-producing cells such as TNF, IL1 and IL6-secreting macrophages, lymphocytes and mast cells [90,91], which are reported to play a major role during the inflammatory phase of COVID-19 infection (i.e., the cytokine storm [92]). The ivermectin-induced enhancement of this pathway might rapidly lower pro-inflammatory cytokine levels and decrease expressions of chemokines as well as adhesion molecules at the inflammatory sites [90,91]. Importantly, the marked increase in Ca^{++} current evoked by acetylcholine (ACh) in the presence of micromolar concentrations of ivermectin (e.g., a 20-fold shift of the affinity of ACh [89]) may also potentially explain the reported clinical activity of ivermectin during the late (i.e., inflammatory), critical phase of severe COVID-19 cases [93].

Recent in silico docking studies have indicated a potential direct interaction between the SARS-CoV-2 spike glycoprotein and $\alpha 7nAChr$, due to a "toxin-like" epitope on the spike glycoprotein, with homology to a sequence of a snake venom toxin [5,6]. Of

interest, the $\alpha 7$ nAChR receptor, which is densely distributed on neuronal tissue, has previously been shown to serve as the port of entry in the human body for another RNA virus endowed with strong neurotropic action, the rabies virus [7]. The loss of smell (anosmia) and/or taste (ageusia) are considered hallmarks of COVID-19 infection and are likely consequences of the direct SARS-CoV-2 infection of the olfactory and gustatory nerve [94]. Ivermectin high affinity binding to $\alpha 7$ nAChR may therefore interfere with the attachment and internalization of SARS-CoV-2 on the olfactory/gustatory nerves, as recently reported in both animal models [94] and human patients [95].

Materials and methods

2. *Material and Methods*

2.1. *Ligand database preparation:*

Ivermectin was selected as the main target of this study. 14 extra compounds which have similar chemical structure to ivermectin were collected from PubChem database and used in the docking simulation to investigate the possible inhibitory behavior of collected compounds. Online Drug Bank database provide structurally similar compounds and families to the searched compound (Ivermectin) [107]. By using this tool, the user would be capable to rapidly search for structurally similar small molecules, without spending too much time for redrawing the molecules structures and performing ChemQuery research. The selected ligand set database was prepared through a “WASH” wizard of the molecular operating environment (MOE) software in advance to run any kind of simulation and interaction analysis. MOE software is capable of generating the 3D dominant protonation state of each molecule at the neutral physiological pH and a built-in energy minimization procedure. all these actions were performed to minimize any possible simulation error in molecular dynamic simulation.

2.2. *Protein preparation:*

CD147: As it is explained in the literature review section of this study, CD147 is expressed in widely in both humans and animals. CD147 expression in humans happen in different 3D structures and in different cell types. The crystal structure of CD147 was obtained from its Protein Data Bank (PDB: 3B5H) which is the special configuration of extracellular portion of CD147 expressed in human cell having the strongest electron density in the Chain A (extracellular portion of CD147) was the second reason of using this specific configuration for structural analysis.

SARS-CoV2-Spike: The CHARMM-GUI Archive of COVID-19 Proteins Library [108] was used to collect the structures of the spike protein conformations. This library contains several 3D structural model of spike protein with different properties. The conformations are provided in open and closed structures, fully glycosylated full length

of the protein. Other configuration for other uses could be found in this database (i.e., Complex model of S-protein, Models of the head only (S1), Complex with small molecules and ligands). For this study the two general conformation of spike protein which are the closed (PDB: 6VXX) and open (PDB: 6VSB) states are considered [9,109,110]. The NTD (aa 18–292) and RBD (aa 318–513) of one monomer were considered separately in this study.

SARS-CoV-2-Mutated Spike protein: Same procedure was implemented in case of mutated spike protein preparation through the CHARMM-GUI archive of covid-19 proteins library [108]. In this study only open conformation of the mutated spike protein is used which can be found in the CHARMM-GUI Archive of COVID-19 Proteins Library under the code's name of (7BNN). This is very important to note that, the mutation D614G is the most common mutation among all lethal variant which is repeated constantly and were reported by many authors. This mutation is occurred in the joint function of S1 and S2 trimer.

Nicotinic Acetylcholine protein: $\alpha 7nAChR$ has three different structural conformation which are introduced by different researchers. Resting conformation (PDB: 7KOO) and Desensitized conformation (PDB: 7KOQ) and activated conformation (PDB: 7KOX). The atomic coordinates of three possible conformations of $\alpha 7nAChR$ were obtained from the PDB [111]. Only the extracellular region of the protein was the interest of this study (aa 1–207) and was considered in the docking analysis.

All the considered proteins are collected from the online databases (CHARMM-GUI Archive of COVID-19 Proteins Library, PDB) and imported into MOE. The adjustment of protonation state of each protein structure was performed in the MOE to achieve a neutral physiological pH and to obtain the minimum potential energy configuration.

2.3. *Biding sites identification:*

SARS-CoV-2: To identify all the potential binding sites in the spike proteins of both original and mutated one, site finder tool in the MOE software was employed to investigate the potent [112] binding sites in the NTD, RBD and S1/S2 joint (specifically for D614G mutation) domains of the spike protein. All the sites which were identified by site finder tool in the MOE software had already been reported in the literature by

other researchers. A summary of all the reported binding sites in both original and mutated spike protein that has been considered in this study for docking simulation are provided below in the Table.2.1. At the end, molecular modeling calculations was performed by using the sites specified in Table 2.1. All the center of binding sites were manually calculated with respect to the residues involved.

Table 2.1. Binding Sites of Spike Protein

<i>Reference</i>	<i>Binding site</i>	<i>Binding site type</i>	<i>Residues</i>	<i>Domain</i>
<i>Milanetti et al. [103]</i>	<i>Site 1</i>	<i>Sialoside</i>	<i>L18-Q23, H66-T78 and G252-S254</i>	<i>NTD</i>
<i>Behloul et al. [113]</i>	<i>Site 2</i>	<i>Sialoside</i>	<i>E154, F157, Y160 and the so-called stabilizing loop (N122-N125)</i>	<i>NTD</i>
<i>Baker et al. [12]</i>	<i>Site 3</i>	<i>Sialoside</i>	<i>(R21, Q23, L24, H69, F79, P82 and R246)</i>	<i>NTD</i>
<i>Di Gaetano et al. [114]</i>	<i>Site 4</i>	<i>Sialoside</i>	<i>21, T22, Q23, L24, P26, R78, P82, V83, L110, F135, C136, N137 and R237</i>	<i>NTD</i>
<i>Di Gaetano et al. [114]</i>	<i>Site 5</i>	<i>Sialoside</i>	<i>F92, S94, E96, K97, S98, R102, N121, V126, I128, M177, D178, K182, N188, R190, F192, I203, L226, V227 and L229.</i>	<i>NTD</i>
<i>Watanabe et al. [11]</i>	<i>Site 6-14</i>	<i>glycosylation</i>	<i>N122, N149, N165, N17, N61, N74, N234, N282</i>	<i>NTD</i>

<i>Reference</i>	<i>Binding site</i>	<i>Binding site type</i>	<i>Residues</i>	<i>Domain</i>
<i>Fantini et al. [101]</i>	<i>Site 15</i>	<i>ganglioside</i>	<i>Domain (111–158)- core Q-134 to D-138</i>	<i>NTD</i>
<i>Carino et al. [117]</i>	<i>Site 16</i>	-	<i>F342 N343 A343 T345 R346–W436 N437 S438–L441 D442, S443–G446–N448–Y451 L452</i>	<i>RBD</i>
<i>Carino et al. [117]</i>	<i>Site 17</i>	-	<i>S375–G404 D405–V502 G503–Q506–Y508</i>	<i>RBD</i>
<i>Carino et al. [117]</i>	<i>Site 18</i>	-	<i>E340 V341–F347 A348–N354 R355 K356–S399 F400, V401–V512</i>	<i>RBD</i>
<i>Carino et al. [117]</i>	<i>Site 19</i>	-	<i>F374–N388–Y495 G496 F497</i>	<i>RBD</i>
<i>Carino et al. [117]</i>	<i>Site 20</i>	-	<i>T376 F377 K378 C379 Y380–V407 R408–I410–V433 I444, A445</i>	<i>RBD</i>
<i>Watanabe et al. [11]</i>	<i>Site 21-22</i>	<i>glycosylation</i>	<i>N331–N3443</i>	<i>RBD</i>

Milanetti et al. [103] proposed a potential sialoside binding site which includes three divergent loops (introduced as binding site 1 in this study). Several sialoside-, glycosylation- and ganglioside- binding sites have been reported in the literature. By using iso-electron density mapping, they reported the hypothesis of structural resemblance between two MERS-CoV and SARS-CoV. In another study Behloul et al. [113] successfully characterized the second binding pocket in the spike protein that is capable of binding with SA species like Neu5,9Ac2 while comparing the structural

features of SARS-CoV-2 spike protein N terminal in the S1 region with BCoV (Binding site 2). Baker et al. [12] aligned the sequences of the SARS-CoV-2 spike protein, mainly focusing on human coronavirus OC43 as the SA-binding protein. They identified a potential SA binding site, associating its glycan-binding characteristic utilizing glyconanoparticles for the detection (site 3). Gaetano et al. [114] calculated the druggability of all available ligand-binding pockets within the NTD segment of the spike protein S1 using SiteMap of Schrodinger software [115]. As a result, among all of the three hypothesized sialoside-binding pockets in the literature, site 3 by Baker et al. [12] is part of a cavity with a druggable property identified by Gaetano et al. (site 4 in Table 1, or site P1 as Gaetano et al. referenced in their paper [114]). Gaetano et al. also identified an unexpected binding pocket (site 5 in Table 1, or P2 as they referenced in their paper) within S1-NTD. Site 5 (P2) aligns with the recent experimental findings by Bangaru et al. [116].

Sites 6 to 14 are associated with the glycosylation binding sites proposed by Watanabe et al. [11]. Fantini et al. [101], meanwhile, suggested a new type of ganglioside-binding domain performing molecular dynamics (MD) calculations. The results of his simulations reveal a strong interaction between GM1 ganglioside and S1-NTD (site 15). Finally, Carino et al. [117] utilized the Fpocket server (<https://bioserv.rpbs.univ-paris-diderot.fr/services/fpocket/>, accessed on 22 February 2022) and computationally identified sites 16 to 20 in the RBD fragment of the spike protein. They also studied the binding of several triterpenoids (e.g., glycyrrhetic and oleanolic acids) and natural bile acids and demonstrated that their semisynthetic derivatives can reduce RBD adhesion to ACE2 in vitro. Sites 21 to 22 belong to the set of glycosylation binding sites proposed by Watanabe et al. [11].

SARS-CoV-2, D614G mutation: As mentioned above, D614G mutation, is the most common mutation in all different SARS-CoV2 variations. MOE is employed to identify all the possible binding sites of this protein. The 3D structure of D614G mutation is introduced by [Benton, D, J] in 2021, as the open conformation of mutated spike protein with 1 erect RBD. In this study, they provide structural analysis to compare D614 spike protein with G614 spike protein, and the outcome supported the fact that, G614 mutant spike adopts a range of more open conformations that may facilitate the binding procedure and the subsequent structural rearrangements required for viral membrane

fusion. Same procedure for identifying the binding sites of mutated spike protein is implemented as it was conducted for the Wuhan variation. The possible binding site of this mutation is presented in the table 2.2 which identified by MOE site finder and reported by other researchers. There are more than 200 introduced binding sites in spike protein. In this study only binding sites with possibility of ligand binding more than 2 are selected. As a results, only 7 binding sites are investigated.

Table 2.2. Binding Sites of Mutated spike protein

<i>Site</i>	<i>Residues</i>	<i>Domain</i>
<i>Site 1</i>	<p>THR912 ASN914 GLU918 PRO1090 ARG1091 GLU1092 GLY1093 VAL1104 THR1105 GLN1106 GLU1111 PRO1112 GLN1113 ILE1114 THR1116 THR1117 ASP1118 ASN1119 THR1120 PHE1121 VAL1122 SER1123 TYR1138 ASP1139 PRO1140 LEU1141 GLU1144)2:(ILE712 ALA713 ILE714 PRO715 ILE909 GLY910 VAL911 THR912 ASN914 TYR1047 PRO1090 ARG1091 GLU1092 GLY1093 VAL1094 VAL1104 THR1105 GLN1106 ARG1107 ASN1108 GLU1111 GLN1113 ILE1114 THR1116 THR1117 ASP1118 ASN1119 THR1120 PHE1121 VAL1122 SER1123 GLY1124 ASP1139 PRO1140 LEU1141 GLU1144)3:(SER884 TRP886 THR887 LEU894 GLN895 ILE896 TYR904 PHE906 ASN907 GLY910 VAL911 THR912 ASN914 GLU918 LYS1086 HIS1088 PRO1090 ARG1091 GLU1092 GLY1093 VAL1104 THR1105 GLN1106 GLU1111 PRO1112 GLN1113 ILE1114 THR1116 THR1117 ASP1118 ASN1119 THR1120 PHE1121 VAL1122 SER1123 GLY1124 ASP1139 PRO1140 LEU1141 GLU1144)</p>	<i>S2</i>

<i>Site</i>	<i>Residues</i>	<i>Domain</i>
<i>Site 2</i>	<p>1:(TYR38 PRO39 ASP40 LYS41 VAL42 LYS195 ILE197 ASP198 TYR200 LYS202 TYR204 PRO225 ASP228 MET740 TYR741 ILE742 CYS743 GLY744 ASP745 PHE855 ASN856 VAL963 LEU966 SER967 GLY971 ALA972 ILE973 SER974 SER975 VAL976 LEU977 ASN978 ASP979 SER982 ARG983 ARG1000)3:(ARG319 VAL320 GLN321 PRO322 PRO330 GLY381 LEU390 CYS391 PHE392 THR393 ASN394 TYR396 ASP427 ASP428 PHE429 THR430 PHE464 SER514 PHE515 GLU516 LEU517 LEU518 HIS519 ALA520 PRO521 ALA522 THR523 CYS538 ASN540 PHE541 PHE543 ASN544 GLY545 LEU546 THR547 GLY548 THR549 GLY550 GLN564 PHE565 ARG567 ASP568 ALA570 ASP571 THR572 THR573 ASP574 VAL576 ARG577 ASP578 PRO579 ASP586 ILE587 THR588 PRO589 CYS590 PHE592)</p>	<i>S1, NTD</i>

<i>Site</i>	<i>Residues</i>	<i>Domain</i>
<i>Site 3</i>	<p>1:(GLU725 LEU727 PRO728 MET731 GLU773 GLU780 LYS947 ASP950 VAL951 GLN954 ASN955 ILE1013 ARG1014 ALA1015 ALA1016 GLU1017 ILE1018 ARG1019 ALA1020 SER1021 ASN1023 LEU1024 ALA1026 THR1027 LYS1028 ARG1039 ASP1041 PHE1042 CYS1043 GLY1044 LYS1045)2:(GLU725 LEU727 PRO728 MET731 GLU773 LYS776 ASN777 GLU780 ALA783 GLN784 LYS947 ASP950 VAL951 GLN954 ASN955 GLN957 ALA958 THR961 LEU962 GLN965 SER1003 THR1006 TYR1007 GLN1010 ILE1013 ARG1014 ALA1016 GLU1017 ILE1018 ARG1019 ALA1020 SER1021 ASN1023 LEU1024 ALA1026 THR1027 LYS1028 SER1030 GLU1031 ARG1039 VAL1040 ASP1041 PHE1042)3:(PHE759 GLN762 LEU763 ARG765 ALA766 GLY769 ILE770 VAL772 GLU773 LYS776 ASN777 GLU780 VAL1008 LEU1012 ALA1015 ALA1016 GLU1017 ARG1019 ALA1020 ASN1023 LEU1024 ALA1026 THR1027 SER1030 GLU1031 ARG1039)</p>	<i>S2</i>

<i>Site</i>	<i>Residues</i>	<i>Domain</i>
<i>Site 4</i>	<p>1:(ARG319 VAL320 GLN321 PRO322 CYS538 PHE541 LEU546 THR547 GLY548 THR549 GLY550 ARG567 ASP568 ILE569 ALA570 ASP571 THR572 THR573 ASP574 ILE587 THR588 PRO589 CYS590 PHE592)2:(ARG44 VAL47 LEU48 HIS49 SER50 CYS301 THR302 LEU303 LYS304 SER305 THR307 GLU309 MET740 TYR741 ILE742 CYS743 GLY744 ASP745 SER746 ALA852 PHE855 ASN856 ASN953 ALA956 GLN957 ALA958 ASN960 THR961 VAL963 LYS964 GLN965 LEU966 SER967 SER968 SER975 VAL976 LEU977 ASN978 LEU981 ARG1000)3:(TYR756 GLY757 SER758 THR761 ARG765)</p>	<i>S1/S2 joint function</i>

<i>Site</i>	<i>Residues</i>	<i>Domains</i>
<i>Site 5</i>	<p>1:(SER50 THR274 LEU276 THR299 CYS301 THR302 LEU303 LYS304 ILE312 TYR313 GLN314 THR315 SER316 ASN317 GLY593 GLY594 VAL595 SER596 LEU611 GLN613 GLY614 VAL615 ASN616 GLN644 THR645 ARG646 ALA647 GLY648 CYS649 PRO665 ILE666 GLY667 ALA668 GLN957 ASN960 THR961 LYS964)2:(THR732 LYS733 SER735 VAL736 ASP737 CYS738 THR739 SER750 LEU753 LEU754 TYR756 GLY757 SER758 PHE759 CYS760 THR761 ASN764 ARG765 THR768 ALA771 VAL772 ASP775 LEU828 LYS854 GLY857 THR859 VAL860 LEU861 PRO862 PRO863 LEU864 HIS1058)</p>	S2
<i>Site 6</i>	<p>1:(PHE86 ASN87 ASP88 GLY89 THR108 LYS113 THR114 GLN115 SER116 VAL130 CYS131 GLU132 ASN165 THR167 PHE168 ASN196 ILE197 ASP198 GLY199 TYR200 PRO230 ILE231 GLY232 ILE233 ASN234 ILE235)3:(TRP353 ASN354 ARG355 LYS356 ARG357 TYR396 PRO463 PHE464 GLU465 ARG466 ASP467 ILE468 SER469)</p>	S1, RBD

<i>Site</i>	<i>Residues</i>	<i>Domain</i>
<i>Site 7</i>	1:(ASN907 GLY908 ILE909 GLY910 GLN1036 SER1037 LYS1038 ARG1039 VAL1040 ASP1041 PHE1042 CYS1043 GLY1044 LYS1045 GLY1046 TYR1047 HIS1048 ARG1091 GLU1092 ARG1107 ASN1108)2:(GLN784 SER884 GLY885 TRP886 THR887 GLY889 ALA890 ILE896 GLN901 TYR904 ASN907 GLY908 SER1030 LEU1034 GLY1035 GLN1036 LYS1038)	S2

CD147: According to the workflow implemented in this study, after identification of all the potential binding sites in the both original and mutated spike protein of SARS-CoV-2, CD147 is the next target to be analyzed. Similarly, by using the site finder tool in the MOE software, nine different binding sites has been identified which are listed in the table below TABLE 2.3. and for more clarity these binding sites are presented graphically as well in Figure 2.1. the most promising *N*-glycosylation binding sites of CD147 are N44 (site 8), N152 (site 3) and N186 (site 3).

Table 2.3. Binding sites of CD147

<i>Binding Site</i>	<i>Residues</i>
<i>Site 1</i>	S78 D79 D80 Q81 W82 G83 Q100 L101 HID102 G103 P104 P105 R106 E129 S130 V131 P132 S193 D194
<i>Site 2</i>	A109 V110 K111 E114 M123 L124 V125 I198
<i>Site 3</i>	W137 A138 W139 L150 M151 N152 V160 N186
<i>Site 4</i>	R106 V107 K108 K127 S128 E129 Q164 G165 R166
<i>Site 5</i>	HIP53 W55 L62 E64 L67 K71 T72 E73
<i>Site 6</i>	L38 L62 E73 F74 K75
<i>Site 7</i>	K57 V61 F74 D80 W82 Y85
<i>Site 8</i>	I37 Q81 Q100 L101 HID102 G103 P104 N44
<i>Site 9</i>	K57 W82 G83 E84 Q100 E129

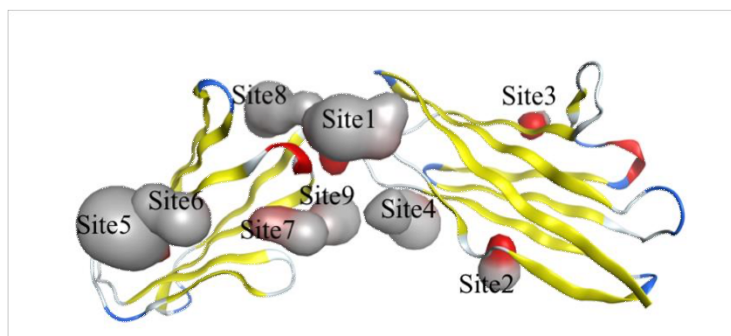


Figure 2.1. CD 147, Binding sites illustration

Nicotinic Acetylcholine: Next step of binding sites identification is about investigation on $\alpha 7nAChr$ potential binding sites. By using MOE site finder tool which aims to characterize the possible binding sites of the imported protein with geometrical approach through the 3D structure of targeted protein. Three different conformations of $\alpha 7nAChr$ (Resting, Activated, Desensitized) were analyzed by site finder tool in MOE. For each protein, only the sites characterized by a propensity for ligand binding (PLB) greater than or equal to 1 were considered in for docking simulation. Among all the identified binding sites of three different configurations of $\alpha 7nAChr$ (Resting, Activated, Desensitized), the common ones are excluded, and the rest are presented in Table 2.4.

Table 2.4. Binding sites of $\alpha 7nAChr$

<i>Conformation</i>	<i>Binding site</i>	<i>residues</i>
<i>Resting</i>	<i>Site 1</i>	(P16 L17 R19 D24 S25 Q26 P27 L55 M57 D81 G82 I84 W85 K86 P87 D88 I89 L90 Y92 D100 T102 HIP104 Y117 P119 S147 W148 S149 Y150 G151 W153 S154 Y187 C189 C190 E192 Y194) and (Q3 Y7 G73 V74 K75 T76 V77 R78 F103 T105 N106 L108 Q116 Y117 L118)

<i>Conformation</i>	<i>Binding site</i>	<i>Residues</i>
<i>Resting</i>	<i>Site 2</i>	(Q3 G73 V74 K75 T76 R78 T105 N106 L108 Q116 Y117 L118) and (R19 D24 S25 Q26 P27 Y92 S147 W148 S149 Y150 G151 W153 S154 Y187 C189 C190 E192 Y194)
<i>Resting</i>	<i>Site 3</i>	(P16 L17 L55 M57 D81 G82 I84 W85 K86 P87 D88 I89 L90 D100 T102 HIP104 Y117 P119 W148 S149 Y150) and (Y7 R78 F103 HIP104 T105 N106)
<i>Desensitized</i>	<i>Site 1</i>	(K45 N46 Q47 S126 C127 A257 E258 M260 P261 A262 T263) and (Q38 I39 M40 D41 V42 D43 E44 K45 F134 P169 N170 G171 E172 W173 R205 Y209 Y210 N213 L214 L255 V256 E258 I259 M260)
<i>Desensitized</i>	<i>Site 2</i>	Y7 R78 F79 P80 D81 F103 H04 T105 N106) and (P16 L17 E18 L55 M57 D81 I84 W85 K86 P87 D88 I89 L90 D100 T102 H04 Y117 P119 S149 Y150)
<i>Desensitized</i>	<i>Site 3</i>	(Y92 S147 W148 S149 Y150 W153 Y187 C189 C190 K191 E192 Y194) and (W54 T76 R78 T105 N106 V107 L108 N110 Q116 Y117 L118 P119)
<i>Desensitized</i>	<i>Site 4</i>	(Q47 Y92 N93 S126 C127 Y128 H40 C141 K142 K144 Y187 T200) and (L37 Q38 N52 W54 I168 P169 N170)
<i>Activated</i>	<i>Site 1</i>	(K45 N46 Q47 V48 A95 E97 K124 S126 C127 Y128 M253 L254 A257 E258 M260 P261 A262 T263) and (Q38 I39 M40 D41 V42 D43 E44 K45 T50 I122 I168 P169 N170 E172

		W173 R205 Y209 Y210 N213 L214 F252 L255 E258 I259 M260)
<i>Activated</i>	Site 2	(R19 D24 S25 Q26 P27 Y92 S147 W148 S149 G151 W153 S154 Y187 C189 C190 K191 E192 Y194) and (Q3 W54 G73 V74 K75 T76 R78 T105 N106 L108 N110 Q116 Y117 L118 P119)
<i>Activated</i>	Site 3	(P16 L17 M57 D81 G82 I84 W85 K86 P87 D88 I89 L90 D100 T102 H04 Y117 P119 W148 S149 Y150) and (Y7 R78 F79 P80 F103 H04 T105 N106)
<i>Activated</i>	Site 4	(V287 I290 V291 Y294 HID295 P299 D300 G302 K303 P305 T308 R309 L312 E436 W437 A440 V444)

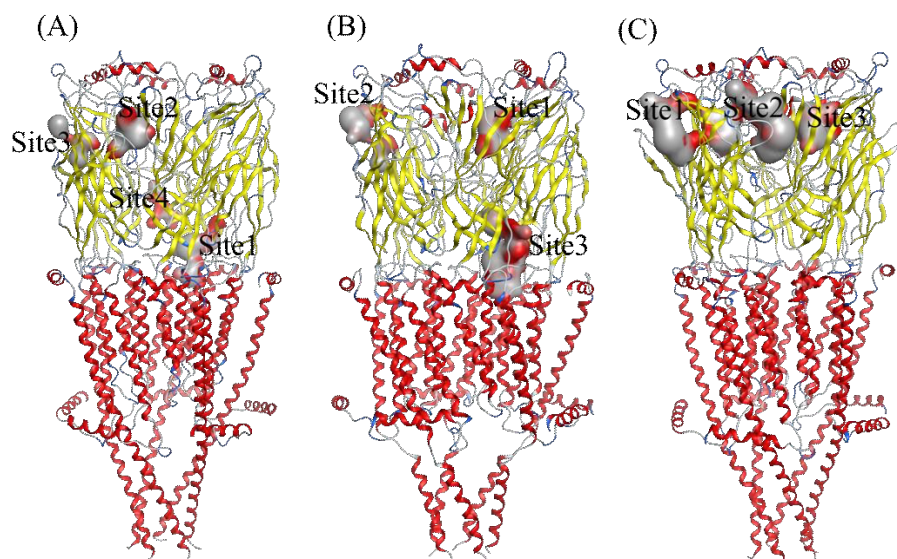


Figure 2.2. Binding sites of (A) desensitized, (B) activated and (C) resting conformations of $\alpha 7$ nAChR protein

2.4. *Molecular docking simulation:*

Flexible ligand and rigid receptor approach is employed to perform the docking procedure by using AutoDock Vina program and MOE (molecular operating environment) software [112,118]. The aim of docking at this stage is to predict different ligand poses in the selected binding site. In this process receptor–ligand binding affinities are predicted as a negative energy (Free Gibbs energy) (ΔG) which the standard unit is expressed as kcal/mol. The binding affinities are calculated on the basis of the scoring function and classified on the basis of a numerical value referred to as the “Score”. Therefore, the interaction of small molecules or ligands with the targeted proteins in the receptor binding sites are predicated based on Score which is a negative value. Score indicates the probability of the docking and interaction between the inhibitors (ligand) and the targeted proteins (receptor), the lower the Score value, the greater interaction. Scoring function incorporates two features from knowledge-based and empirical potentials. A cubic box with 30.0 Å size, required to delimit the docking area, was used on each binding pocket, centered at their center of geometry. A maximum number of poses for each ligand is considered for this study which 20 different poses for each ligand in each binding site. Root mean square deviation (RMSD) to distinguish between two different poses is considered 1 Å at the lowest value (the minimum). Receptors (proteins) are kept fully rigid and then all the different ligand poses that are generated by the software are energy-minimized in Vacuo by using Amber16 [119], in this process then, out of box poses are discarded. Finally, the Vina Score function was used to re-score the poses after the minimization and the pose with the best Score was selected for each compound–receptor pair. The DockBox package was used to facilitate the preparation of docking inputs, the post-processing of the docking results and the rescoring procedure [120]. In the docking process, no extra constraint was applied. The minimization of ligand-protein structures was performed, and the stability of compounds was examined by running 100 ns MD calculations in explicit solvent on the unrestrained ligand-complex structures.

To the best of our knowledge, so far there are no effective therapeutics for COVID-19 which have biological mechanisms similar to those indicated for our studied test compounds to be comparable with our docking results which could be checked for competitive binding to the spike proteins in original and mutated one or the other host receptors such as CD147. Therefore, the limitation of not being able to usefully check

these results against known controls exists. In order to evaluate docking parameters for a given target prior to undertaking docking calculations on unknown ligands, however, it is always beneficial to perform control docking if the binding of known ligands is available in the crystal structure and if they have a non-covalent nature. As a matter of fact, positive control docking calculation was performed for the ligands that were experimentally available in the crystal structure of the proteins that are used in this investigation. It was not possible to use the NAG (N-acetyl-D-glucosamine) ligand (PDB: 6VSB) of the spike protein as a positive control since the nature of the binding was covalent. Also, it was not possible to conduct a control docking on the CD147 protein (PDB: 3B5H) since there was no known ligand available in the crystal structure. The ligand Epibatidine (PDB:7K0X) of the alpha-7 nicotinic acetylcholine receptor was used as a control. One of the successfully generated exact same poses is (RMSD = 1.2 Å) with a binding affinity of -8.73 kcal/mol (see Figure 2.4). Decoys are used, which are molecules that are physically and structurally similar but deeply different chemical formulas to the active ligands [121], as a negative control for the docking calculations. A state-of-the-art benchmark is employed, the Directory of Useful Decoys (<http://dude.docking.org>, accessed on 22 February 2022), to select decoys for ivermectin [122,123]. The structures of the decoy compounds are presented in the (Figure 2.4). The binding affinities of the decoy compounds for the spike protein S1, CD147 and $\alpha 7$ nAChr binding sites are in the range of (-3.345 to -5.496 kcal/mol), (-4.217 to -5.137 kcal/mol) and (-4.940 to -6.070 kcal/mol), respectively. The decoy compounds exhibited lower affinities than ivermectin and the most related compounds.

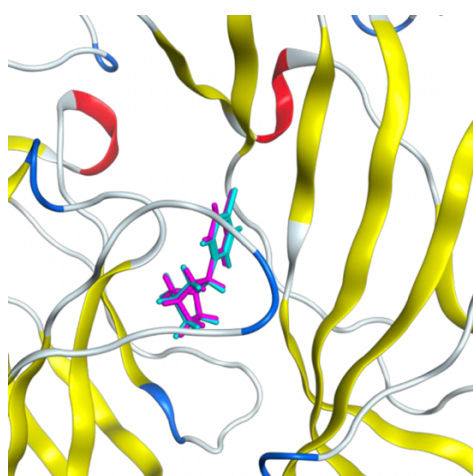


Figure 2.3. Positive control docking of Epibatidine

Experimental pose of Epibatidine is depicted in purple, while the docking pose is shown in cyan.

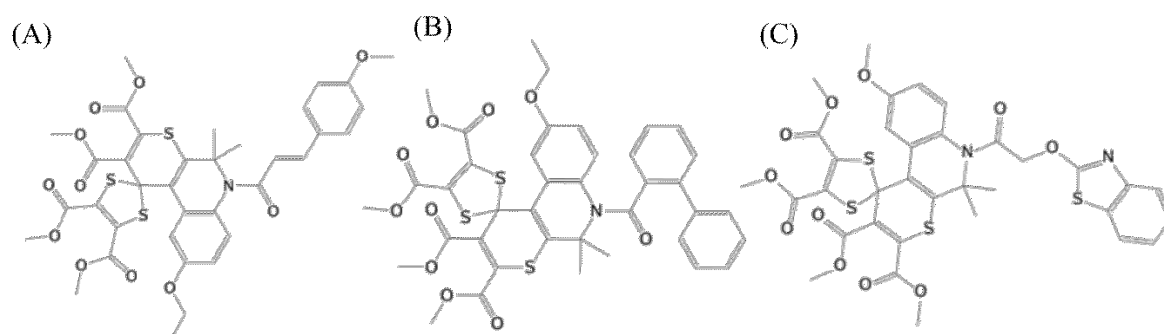


Figure 2.4. Decoy compounds.

2.5. Molecular dynamics simulation:

It is necessary to investigate the stability of each Protein-ligand complex after docking procedure, therefore, MD simulation was employed in explicit solvent by AMBER16 software. A research group on Texas Advanced Computing Center (TACC) successfully hit the benchmarks of ~60 ns/day on 256 GPU nodes [124] which in the presented study the computationally intensive all-atom molecular dynamic simulation is employed both for the open (6x) and closed (3x) system (in each single calculation approximately 1.7 million atoms including explicit water, ions and phospholipid membrane were involved). Several considerations are applied to minimize the computation time and energy consumption. Spike protein in the S1 region is truncated from S698 to D1146 and from P322 to C590 in order to facilitate the ligand binding and receptor interactions in NTD area. S1 is truncated again from M1 to E324 and from C590 to D1146 in the RBD binding area. In case of Nicotinic protein binding and interactions, the hydrophobic part is removed from $\alpha 7nAChr$ protein which is applied from T207 to L320 in each monomer. This is done to make sure the prevention of the exposure of the hydrophobic are in water. Since there is no limitation in case of CD147 protein, no truncation applied to this targeted protein. At the end, all the broken structures in the protein's 3D configurations are capped by MOE's structure preparation mechanism. MD simulations were carried out on Compute Canada's Graham cluster (V100 GPUs), as well as Cedar (P100 NVIDIA GPUs) and personal computer, depending on their respective availability and the calculation power needed to perform the calculation. Each simulation was carried out on a single GPU. Using

the AmberTools 16' leap program, each complex was solvated in a cubic box with a side length of 12 Å using a three-points (TIP3P) water model. Neutralization of the system is done by adding Na⁺ and Cl⁻ ions in such a way to adjust the salt concentration to the physiological value of 0.15 M. the complex minimization is achieved in two different steps, using the steepest descent (5000 steps) and conjugate gradient (5000 steps) methods successively. Initially by restraining the protein-ligand complex the solvent atoms are minimized. then, in the next step the minimization is implemented with the same parameters without any restraint. After the minimization step, the MD simulations are conducted in three stages after the minimization stage. heating, density equilibration and production are different steps in MD simulation. Weak restraints are applied on all backbone atoms while each solvated system is heated up to 298 K for 500 ps. Density equilibrium is the next step which is carried out for 1 ns of constant pressure at 298K with the weak restraints. At the end, MD production (one trajectory per complex) are performed without any restraints for all systems for 100 ns. The trajectory of the ligand–protein complex was visually investigated using the VMD package (the University of Illinois at Urbana-Champaign, Urbana, IL, USA). Time-evolutions of the RMSD of top-ranked inhibitors with respect to different receptors (Spike protein, mutated Spike protein, CD147 and α7nAChr) are calculated using the CPPTRAJ module of the AMBER16 software. Clustering analyses are carried out on the protein-bound ligand poses where the trajectory reached a plateau using Amber's CPPTRAJ program [67]. Consequently, the representative pose selected from the dominant cluster was considered as a predicted ligand pose.

2.6. *Ligand interaction fingerprint:*

In order to fully depict the protein-ligand interaction, MOE software was employed. By using the Fingerprint tool in the MOE, interaction between ligand and receptor with a fingerprint scheme are illustrated. These interactions are fully explained and detailed since the information about the type of chemical bonds such as hydrogen, ionic and surface contacts are fully classified in accordance with the residue in the receptors. Another useful information that is visible in the Fingerprint scheme illustration is the number of interactions between the ligand and receptor which could lead to a better and higher binding affinity.

Results

3. Results

3.1. Molecular docking result:

All the selected compounds (15 compounds including ivermectin) are employed as ligands to be involved in a docking procedure while SARS-CoV-2 spike protein mutated and original, CD147 and $\alpha 7nAChr$ (activated, desensitized and resting states) are the receptor/target which contain the identified binding sites. In the table below all the binding sites in each receptor protein and calculated docking scores are reported. After reporting all the docking scores, respectively the top five ligands which showed lower binding score (higher affinity) are selected and reported in all four targeted proteins. By this means, it would be clear, which ligands (inhibitors) are reported as the top five inhibitors in case of different receptors, and the common inhibitor would be identified.

Table Table 3.1. Docking Scores of all tested compounds and spike protein

Compounds Name	Close Configuration			
	NTD		RDB	
	Score (kcal/mol)	Site	Score (kcal/mol)	Site
<i>Ivermectin</i>	-8.205	Site 4	-7.735	site 22
<i>Moxidectin</i>	-7.659	Site 2	-7.989	site 18
<i>Doramectin</i>	-8.867	Site 9	-8.216	site 19
<i>Oleandrin</i>	-8.083	Site 14	-8.787	site 19
<i>Selamectin</i>	-8.774	Site 10	-8.142	site 16
<i>Okadaic acid</i>	-7.937	Site 4	-8.25	site 18
<i>Gitoformate</i>	-7.88	Site 10	-7.992	site 19
<i>Amphotericin_B</i>	-7.931	Site 4	-7.332	site 21
<i>P-57AS3</i>	-7.704	Site 5	-7.627	site 19
<i>Eprinomectin</i>	-7.088	Site 6	-7.302	site 21
<i>Concanamycin A</i>	-7.347	Site 3	-7.302	site 21
<i>Natamycin</i>	-7.359	Site 4	-6.87	site 18
<i>Nystatin</i>	-6.867	site 14	-6.773	site 19
<i>beta-Escin</i>	-7.264	site 4	-7.296	site 19
<i>Fusicoccin</i>	-6.353	site 10	-6.381	site 18

Compounds Name	Open Configuration			
	NTD		RDB	
	Score (kcal/mol)	Site	Score (kcal/mol)	Site
<i>Ivermectin</i>	-8.948	Site 10	-8.256	Site 17
<i>Moxidectin</i>	-8.902	Site 2	-8.218	Site 21
<i>Doramectin</i>	-8.885	Site 2	-8.144	Site 21
<i>Oleandrin</i>	-8.787	Site 10	-8.051	Site 22
<i>Selamectin</i>	-8.476	Site 15	-7.432	Site 19
<i>Okadaic acid</i>	-8.716	Site 10	-8.067	Site 21
<i>Gitoformate</i>	-8.514	Site 10	-7.669	Site 21
<i>Amphotericin_B</i>	-8.304	Site 15	-7.516	Site 21
<i>P-57AS3</i>	-8.045	Site 4	-7.663	Site 22
<i>Eprinomectin</i>	-7.646	Site 6	-7.584	Site 21
<i>Concanamycin A</i>	-7.564	Site 10	-7.335	Site 19
<i>Natamycin</i>	-7.388	Site 13	-7.529	Site 21
<i>Nystatin</i>	-7.226	site 6	-6.845	site 21
<i>beta-Escin</i>	-7.324	site 10	-7.333	site 21
<i>Fusicoccin</i>	-6.705	site 2	-6.123	site 22

Compounds Name	Docking Score	
	Score (kcal/mol)	Site
<i>Ivermectin</i>	-8.948	NTD-open site 10
<i>Moxidectin</i>	-8.902	NTD-open site 2
<i>Doramectin</i>	-8.885	NTD-open site 2
<i>Oleandrin</i>	-8.787	RBD-closed site 19
<i>Selamectin</i>	-8.774	NTD-closed site 10
<i>Okadaic acid</i>	-8.716	NTD-open site 10
<i>Gitoformate</i>	-8.514	NTD-open site 10
<i>Amphotericin_B</i>	-8.304	NTD-open site 15
<i>P-57AS3</i>	-8.045	NTD-open site 4
<i>Eprinomectin</i>	-7.646	NTD-open site 6
<i>Concanamycin A</i>	-7.564	NTD-open site 10
<i>Natamycin</i>	-7.529	RBD-open site 21
<i>Nystatin</i>	-7.333	RBD-open site 21
<i>beta-Escin</i>	-7.324	NTD-open site 10
<i>Fusicoccin</i>	-6.705	NTD-open site 2

Table3.1. Results of the docking analysis for spike protein S1 binding sites on NTD and RBD in open and closed positions. Scores listed are maximum absolute values for the sites listed in Table 1 for NTD or RBD, open or closed, with the maximum for all four combinations shown in column 2. Compounds are sorted in descending order of that maximum |Score| (column 2).

Table 3.2. Docking scores of all selected compounds and mutated spike protein

<i>Mutated Spike protein (D614G)</i>			
<i>Compound Name</i>	<i>Score (kcal/mol)</i>	<i>Site</i>	<i>Domain</i>
<i>Amphotericin_B</i>	<i>-11.117</i>	<i>Site 5</i>	<i>RBD</i>
<i>Doramectin</i>	<i>-11.039</i>	<i>Site 4</i>	<i>S1/S2 junction (Mutation spot/ NTD)</i>
<i>Ivermectin</i>	<i>-10.788</i>	<i>Site 4</i>	<i>S1/S2 junction (Mutation spot/ NTD)</i>
<i>Gitoformate</i>	<i>-10.750</i>	<i>Site 5</i>	<i>RBD</i>
<i>Eprinomectin</i>	<i>-10.646</i>	<i>Site 5</i>	<i>RBD</i>
<i>Okadaic acid</i>	<i>-10.333</i>	<i>Site 2</i>	<i>NTD</i>
<i>Nystatin</i>	<i>-9.964</i>	<i>Site 5</i>	<i>RBD</i>
<i>beta-Escin</i>	<i>-9.947</i>	<i>Site 2</i>	<i>NTD</i>
<i>Selamectin</i>	<i>-9.928</i>	<i>Site 2</i>	<i>NTD</i>
<i>Fusicoccin</i>	<i>-9.787</i>	<i>Site 4</i>	<i>S1/S2 junction (Mutation spot/ NTD)</i>
<i>Natamycin</i>	<i>-9.189</i>	<i>Site 4</i>	<i>S1/S2 junction (Mutation spot/ NTD)</i>
<i>Moxidectin</i>	<i>-9.044</i>	<i>Site 1</i>	<i>NTD</i>
<i>Concanamycin A</i>	<i>-8.901</i>	<i>Site 2</i>	<i>NTD</i>
<i>P-57AS3</i>	<i>-8.842</i>	<i>Site 5</i>	<i>RBD</i>
<i>Oleandrin</i>	<i>-8.819</i>	<i>Site 4</i>	<i>S1/S2 junction (Mutation spot/ NTD)</i>

Table 3.3. Docking scores of all selected compounds and CD147

<i>CD147</i>		
<i>Compound Name</i>	<i>Score (kcal/mol)</i>	<i>Site</i>
<i>Okadaic acid</i>	-8.578	<i>Site 5</i>
<i>Doramectin</i>	-8.253	<i>Site 1</i>
<i>Selamectin</i>	-8.082	<i>Site 5</i>
<i>P-57AS3</i>	-8.010	<i>Site 1</i>
<i>Concanamycin A</i>	-7.847	<i>Site 9</i>
<i>Ivermectin</i>	-7.527	<i>Site 5</i>
<i>Amphotericin_B</i>	-7.481	<i>Site 1</i>
<i>Moxidectin</i>	-7.469	<i>Site 1</i>
<i>Oleandrin</i>	-7.434	<i>Site 4</i>
<i>Gitoformate</i>	-7.297	<i>Site 8</i>
<i>Nystatin</i>	-7.038	<i>Site 9</i>
<i>Eprinomectin</i>	-6.827	<i>Site 9</i>
<i>beta-Escin</i>	-6.755	<i>Site 1</i>
<i>Natamycin</i>	-6.739	<i>Site 7</i>
<i>Fusicoccin</i>	-5.872	<i>Site 1</i>

Table 3.4. Docking scores of all selected compounds and $\alpha 7nAChr$

<i>$\alpha 7nAChr$</i>		
<i>Compound Name</i>	<i>Score (kcal/mol)</i>	<i>Site</i>
<i>Ivermectin</i>	-10.636	<i>Activated site 2</i>
<i>Doramectin</i>	-10.243	<i>Activated site 2</i>
<i>Okadaic acid</i>	-10.240	<i>Activated site 2</i>
<i>Moxidectin</i>	-10.142	<i>Resting site 1</i>
<i>Concanamycin A</i>	-9.932	<i>Activated site 2</i>
<i>P-57AS3</i>	-9.799	<i>Desensitized site 3</i>
<i>Gitoformate</i>	-9.794	<i>Resting site 1</i>
<i>beta-Escin</i>	-9.711	<i>Resting site 3</i>
<i>Natamycin</i>	-9.611	<i>Activated site 1</i>
<i>Oleandrin</i>	-9.465	<i>Activated site 2</i>
<i>Selamectin</i>	-9.397	<i>Activated site 2</i>
<i>Nystatin</i>	-9.214	<i>Resting site 3</i>
<i>Eprinomectin</i>	-8.968	<i>Resting site 3</i>
<i>Fusicoccin</i>	-8.814	<i>Resting site 3</i>
<i>Amphotericin_B</i>	-8.811	<i>Resting site 3</i>

Compounds are sorted in descending order according to |Score| separately for CD147 and $\alpha 7nAChr$.

3.2. *Compounds selection:*

According to the docking result that are shown in the tables above (TABLES 3.1, 3.2, 3.3, 3.4) the top 5 promising compounds which showed the highest binding affinity, highest absolute value of the score, are reported in accordance with the related receptor (protein). For CD147, 6 compounds are reported since the Ivermectin, the main target of this study is in the 6th place. Okadaic acid, Doramectin, Selamectin, P-57AS3, Concanamycin A are the first 5 compounds. By considering $\alpha 7nAChr$ as the protein receptor, the top 5 most promising compounds are slightly different. Ivermectin, Doramectin, Okadaic acid, Moxidectin and Concanamycin A are best inhibitors for $\alpha 7nAChr$ receptor protein.

In case of considering mutated spike protein, most promising compounds which showed the highest binding affinity are Amphotericin-B, Doramectin, Ivermectin, Gitoformate, Eprinomectin. The top 5 compounds introduced as the most probable inhibitors for spike protein are Ivermectin, Moxidectin, Doramectin, Oleandrin and Selamectin.

Common top inhibitors between CD147 and $\alpha 7nAChr$ are Ivermectin, Doramectin, Okadaic acid and Concanamycin A. In case of CD147 and Spike protein inhibitors, Ivermectin, Doramectin, Selamectin are the common ligands. Comparison between $\alpha 7nAChr$ and Spike protein showed that only Ivermectin and Doramectin plus Moxidectin are the common inhibitors in docking simulation.

Finally, according to the docking simulation results, the common compounds among all 15 tested ligands, Ivermectin and Doramectin are the only ligands that showed high binding affinity to inhibit all four targeted proteins. Ivermectin showed relatively high binding score for docking at the 5th binding site of CD147 with -7.527 (kcal/mol), while Doramectin showed significantly higher binding affinity in the 1st identified binding site of CD147 with -8.253(kcal/mol) binding score. As for $\alpha 7nAChr$ both inhibitors, are docked in the activated state of receptor binding site. Ivermectin and Doramectin, both are docked in the NTD binding domain of spike protein while in both cases, the

absolute value scores are higher for open configuration of Spike protein. These two compounds docked in the NTD domain where is the junction point of S1 and S2, where the mutated is developed in that region. Doramectin reported -11.039 (kcal/mol) and Ivermectin showed -10.788(kcal/mol).

All the top inhibitors considered, with the exception of oleandrin, were found to bind to S1-NTD. Both ivermectin and selamectin bound to site 10 of S1-NTD (Figure 2A,C), which is a glycosylation binding site (N61). Moxidectin and doramectin bound to site 2 S1-NTD (Figure 2A), which is a sialoside binding site proposed by Behloul et al. [113]. Oleandrin bound to site 19 of S1-RBD proposed by Carino et al. [117] (Figure 2B). Site 19 includes the N388 glycosylation binding site.

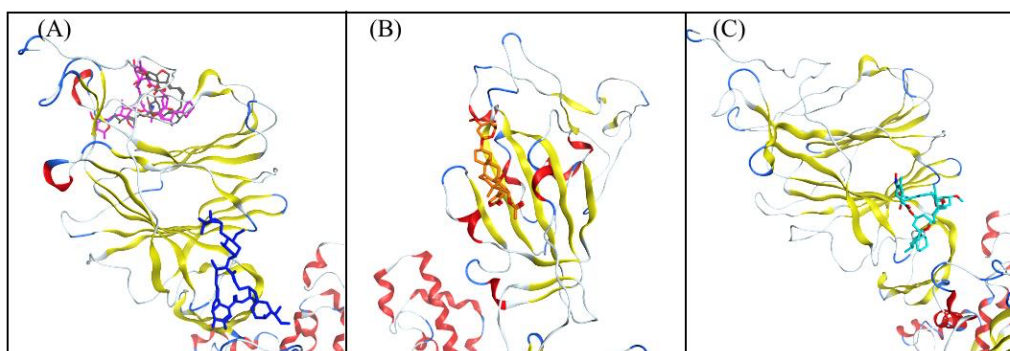


Figure 3.1. Binding poses of ligands and Spike protein

Binding poses of (A) ivermectin (dark blue), moxidectin (dark gray), doramectin (purple) on S1-NTD open conformation; (B) oleandrin (orange) on S1-RBD closed conformation; (C) selamectin (cyan) on S1-NTD closed conformation.

Top ligand compounds for inhabitation of mutated spike protein are docked either in RBD or NTD domain of the receptor. Doramectin and Ivermectin docked in NTD domain and Amphotericin-B, Eprinomectin and gitoformate docked in RBD domain.

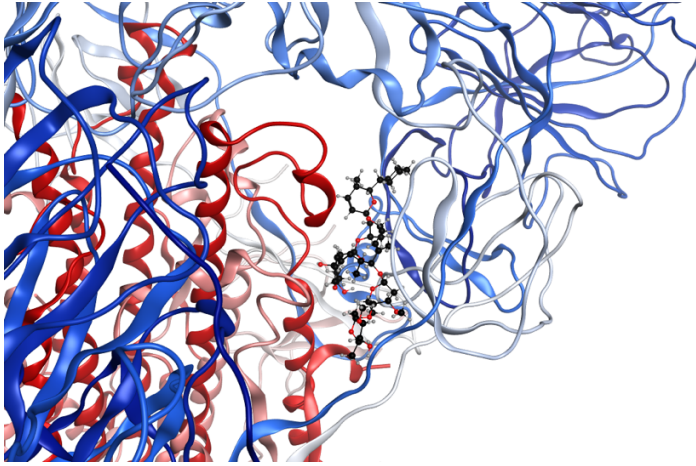


Figure 3.2. Doramectin and Mutated spike protein complex

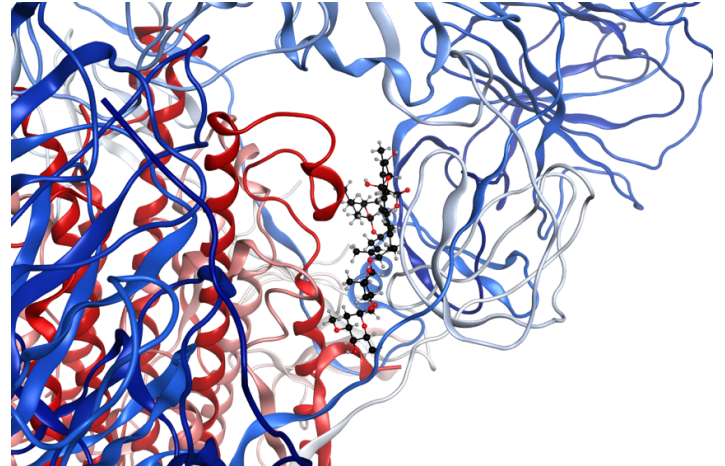


Figure 3.3. Ivermectin and mutated spike protein complex

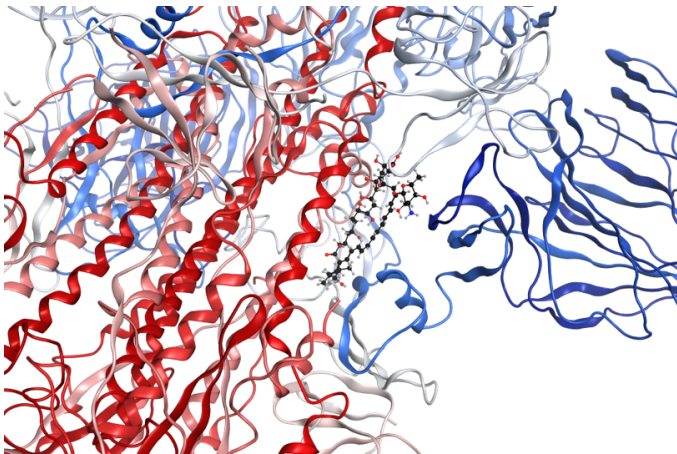


Figure 3.4. Amphotericin-B and mutated spike protein complex

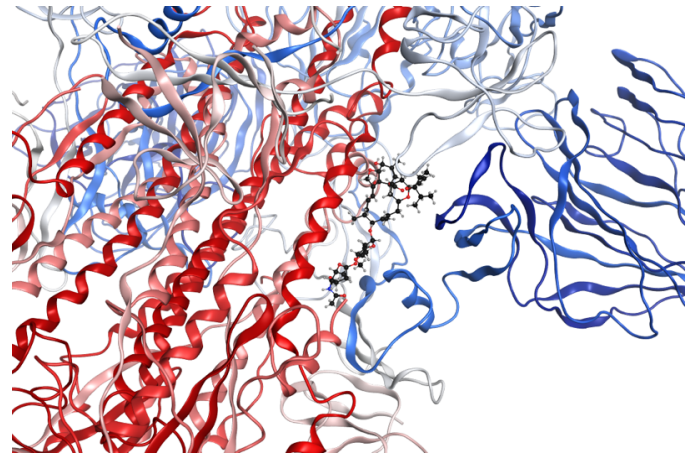


Figure 3.5. Eprinomectin and mutated spike protein complex

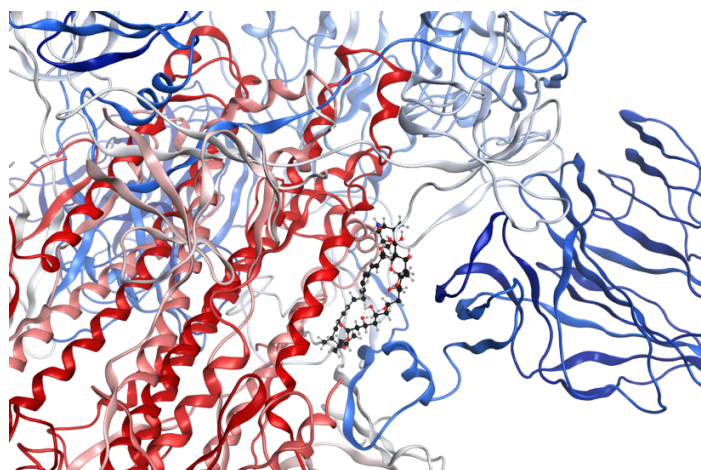


Figure 3.6. Gitoformate and mutated spike protein complex

The binding poses of all the compounds with high affinity for CD147 are shown in Figure 3.7. Okadaic acid, selamectin and ivermectin were found to bind to site 5, which is located in domain A of CD147 protein. Doramectin and P-57AS3 were found to bind to site 1 of CD147, which is in the interface of domain 1 and domain 2 of CD147. Concanamycin A was found to bind to site 9 of CD147.

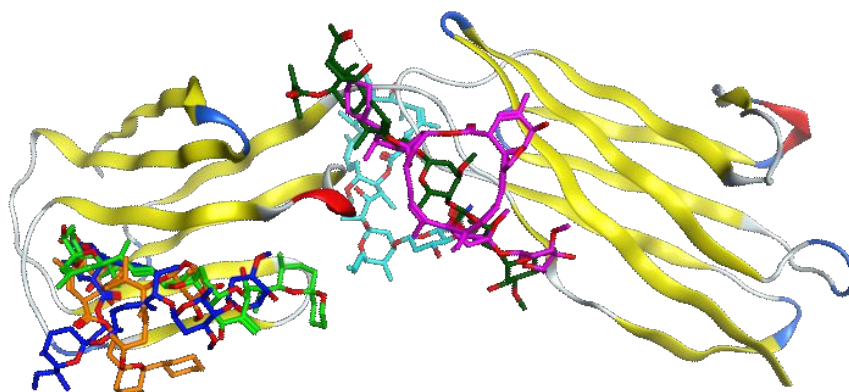


Figure 3.7. Binding poses of top compounds and CD147

Binding poses of okadaic acid (green), doramectin (purple), selamectin (orange), P-57AS3 (dark green), concanamycin A (cyan) and ivermectin (dark blue) on CD147 is depicted in figure 3.7.

The binding poses of all the compounds with high affinity for $\alpha 7nAChR$ are shown in Figure 4. Ivermectin, doramectin, okadaic acid and concanamycin A were found to bind to site 1 of the activated conformation of $\alpha 7nAChR$ (Figure 4A,C). Moxidectin was found to bind to site 1 of the resting conformation of $\alpha 7nAChR$ (Figure 4B,D). In what follows, the interactions of the top inhibitors for the spike, CD147 and $\alpha 7nAChR$ will be discussed.

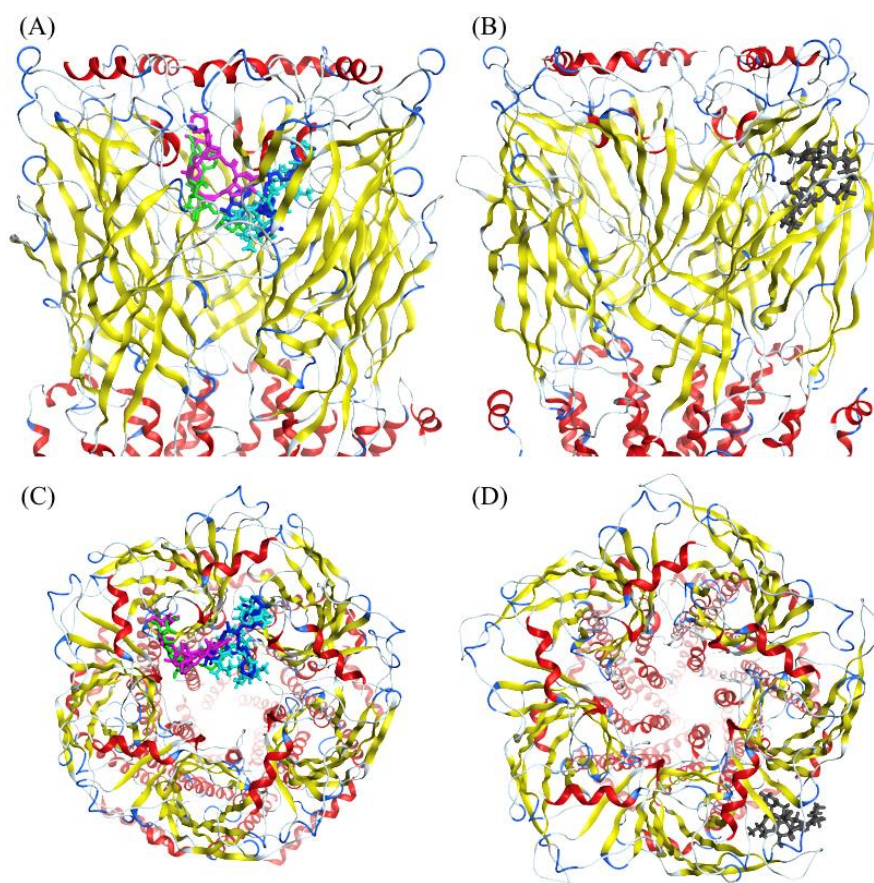


Figure 3.8. Binding poses of top compounds and $\alpha 7nAChR$

Binding poses of ivermectin (dark blue), doramectin (purple), okadaic acid (green), concanamycin A (cyan) on $\alpha 7nAChR$ (A) side and (C) top view. Binding pose of moxidectin (dark gray) on (B) side and (D) top view.

3.3. Molecular dynamics simulation and RMSD analysis:

A 100ns-long MD simulation was performed to check the stability of each protein-inhibitor complex and to discriminate between stable and unstable docked poses. The top-docked pose (with the lowest docking Score) for each protein–ligand complex was

used as an initial structure for the simulations. The binding stability was assessed by following the time evolution of the ligand RMSD in each trajectory, where we used the starting structure as a reference and RMSD alignment was carried out on protein atoms.

From the RMSD analysis and a visual inspection of MD trajectories, we found that, except for salemectin, all of the top five compounds in complex with the spike protein were relatively stable, reaching a RMSD plateau between 2 Å and 4 Å (Figure S5). Conversely, CD147 went through hinge movements during MD (Figure S6), which made it difficult to align the structures and caused fluctuations and higher RMSD values. Visual inspections and ligand–protein interaction analysis (Section 3.4) confirmed that all compounds, except for okadaic acid, maintained their binding to the same binding site during MD simulations ($2 \text{ \AA} < \text{RMSD} < 6 \text{ \AA}$) (Figure S6). Regarding $\alpha 7\text{nAChr}$, a common behaviour was observed for almost all of the compounds: before MD, binding to $\alpha 7\text{nAChr}$ occurred through the interaction between the disaccharide group of each ligand and the activated site2 of $\alpha 7\text{nAChr}$ inside the pore (except for moxidectin, which bound to the outer wall of $\alpha 7\text{nAChr}$). Benzofuran and spiroketal groups were pointed toward the center of the pore, with no apparent hydrogen bonds with any residue. After conducting MD simulations, the stable structure of compounds tended toward a conformation that maintained its binding with activated site 2, with extra binding through the benzofuran group, by getting close to the pore wall. Ivermectin, okadaic acid and moxidectin manifested a stable RMSD ($1.5 < \text{RMSD} < 4$) (Figure S7). An abrupt shift in the RMSD of doramectin was due to the detachment of the benzofuran group from one monomer and the attachment to another monomer due to the symmetry of the $\alpha 7\text{nAChr}$ protein. The new conformation still bound, through disaccharide, with the same binding site, and it was as stable as the first conformation. During visual inspection and through ligand– protein interactions, it was confirmed that concanamycin underwent major binding adjustments with regard to its initial docked conformation and ended up leaving the binding site.

3.4. Protein ligand interaction:

In stable MD trajectories, the top representative pose of each compound was selected from the populationally dominant cluster using clustering analysis on all the trajectories for further ligand–protein interaction analysis. The Protein-Ligand Interaction Fingerprint module of MOE was used to summarize the interactions between ligands and proteins with a fingerprint scheme. N61, R415, F157 and D40 emerged as main residues of the spike protein due to their interaction with high-affinity compounds. As for CD147, the residues interacting with the selected compounds were L46, K87, R85 and H32. In case of $\alpha 7nAChR$, four out of the five selected compounds bound to activated site 2 and interacted with P16, N106, W85 and N100, that are exposed on the interior surface of the protein channel. One compound, namely moxidectin, interacted with N110 of resting state $\alpha 7nAChR$, which is exposed on the outer surface of the protein.

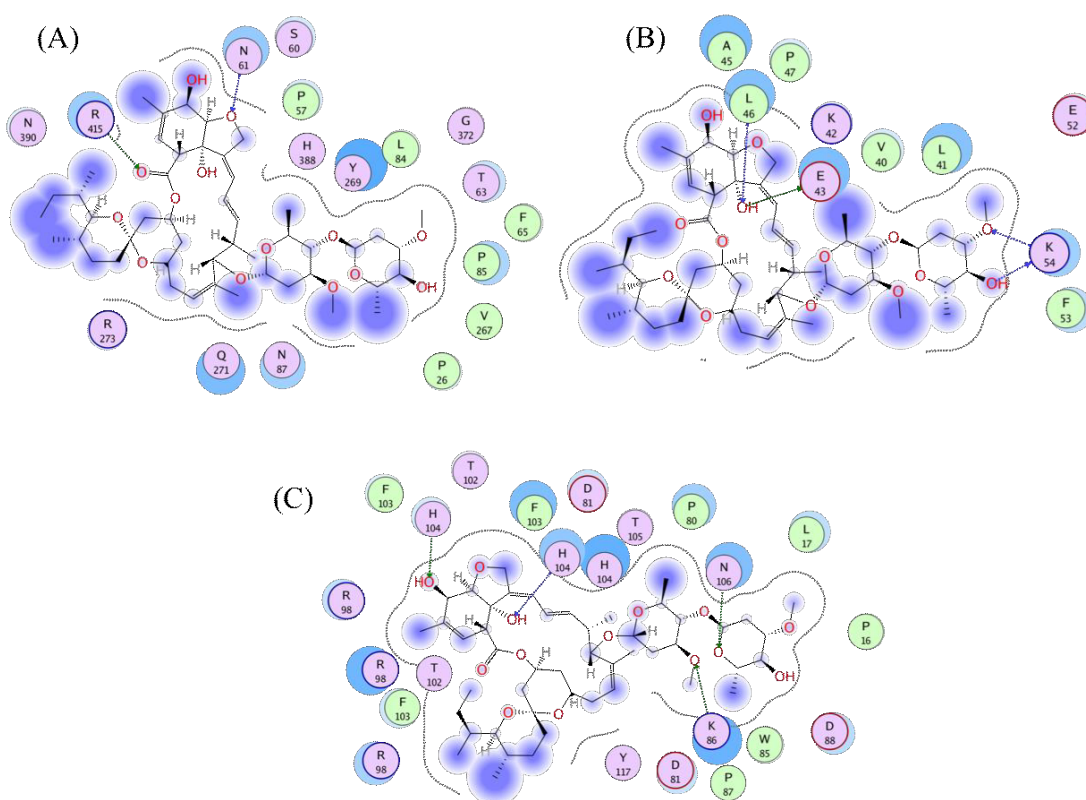


Figure 3.9. Ligand interaction plots of Ivermectin and (A)Spike protein, (B)CD147, (C) $\alpha 7nAChR$

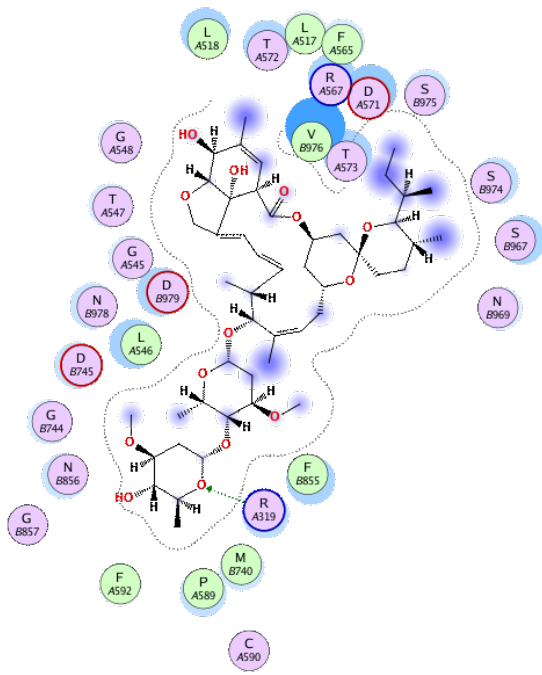


Figure 3.10. Ligand interaction plots of ivermectin for Mutated spike protein (Amino acid D614G)

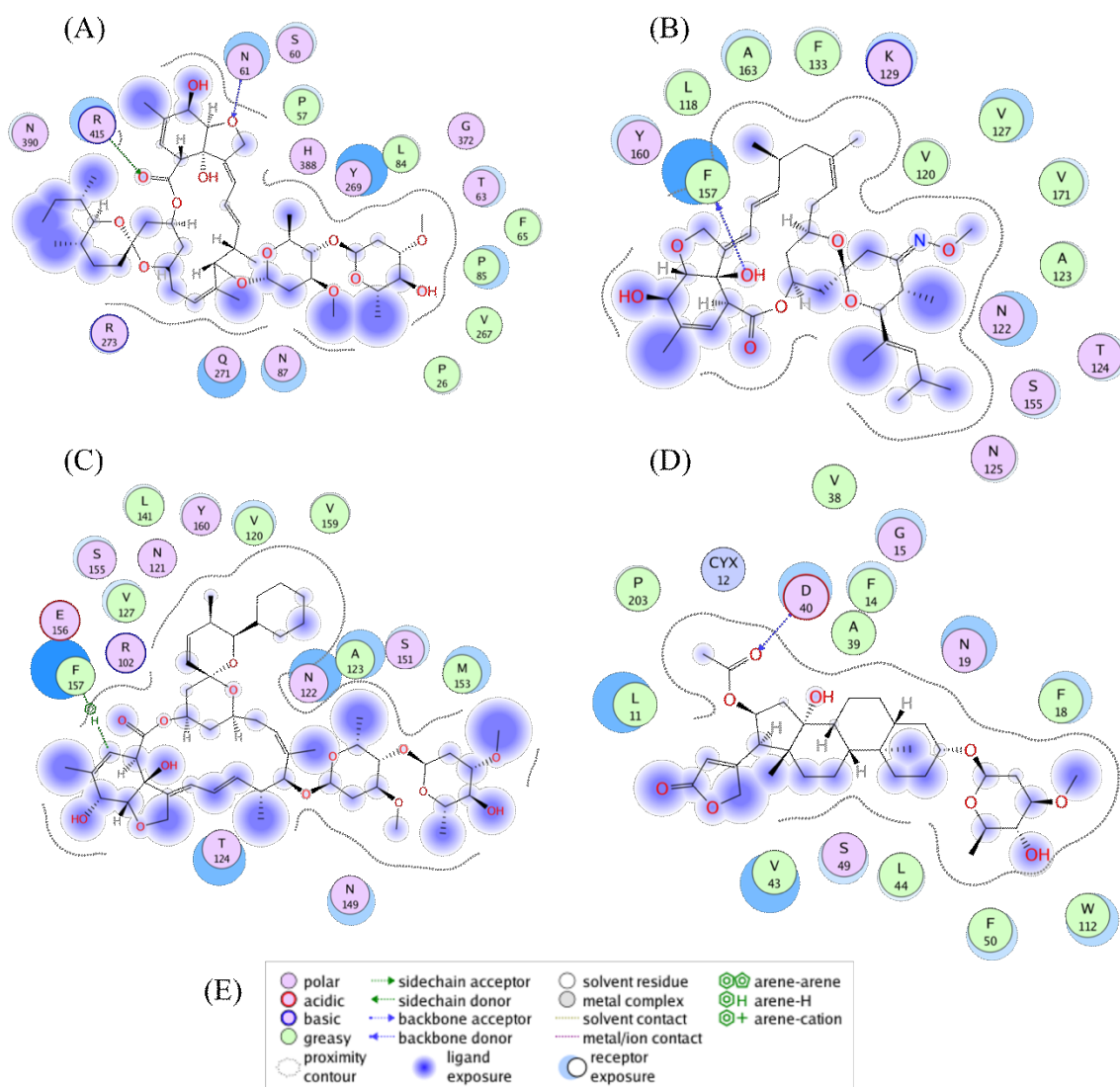


Figure 3.12. Ligand interaction of top compounds and Spike protein

Ligand interaction plots of compounds selected for spike inhibition are provided. (A) Ivermectin, (B) Moxidectin, (C) Doramectin (D) Oleanthin. A graphical key (E) is included to help interpret the 2-D part of the ligand interactions panel.

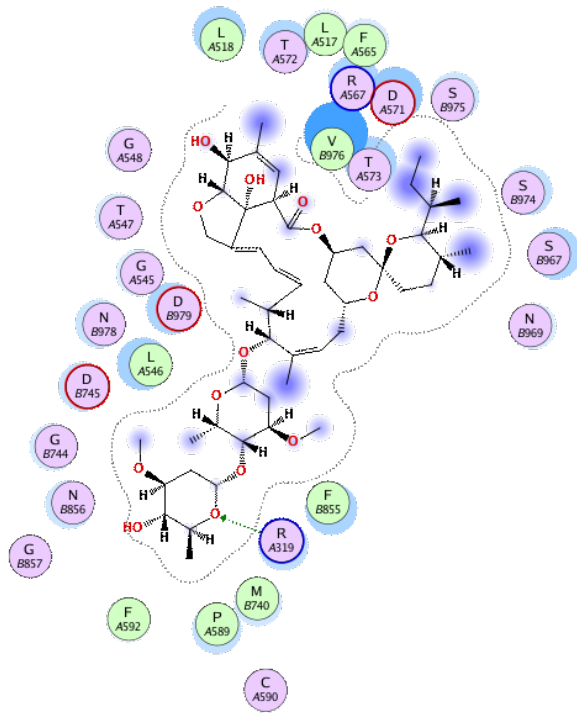


Figure 3.15. Ivermectin and mutated spike protein interaction

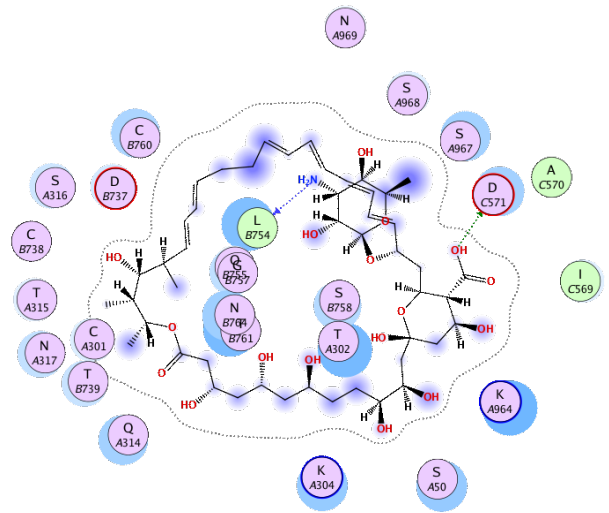


Figure 3.17. Gitoformate and mutated spike protein interaction

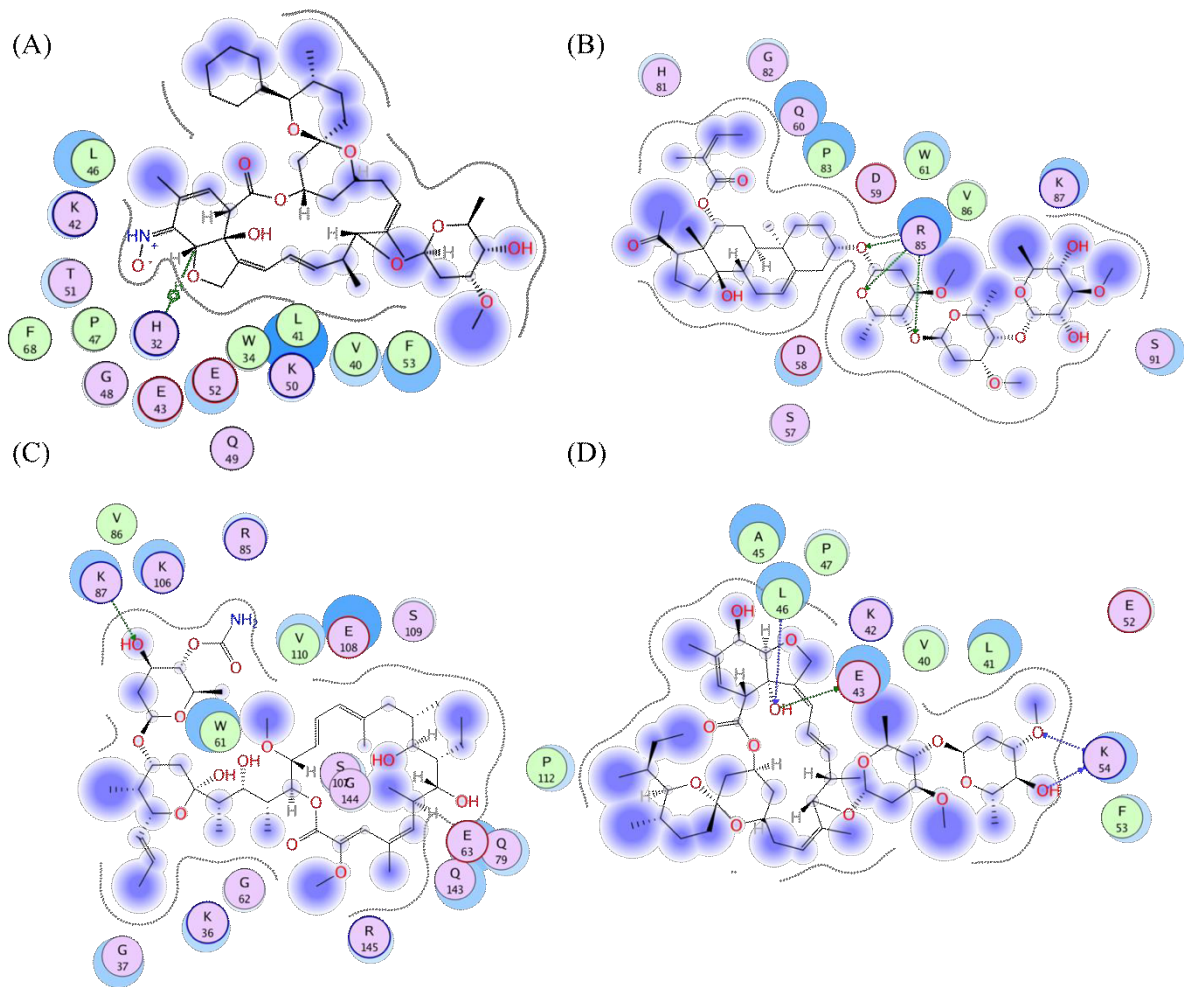


Figure 3.18. Ligand interaction plots of compounds selected for CD147 inhibition (A) Selamectin, (B) P-57AS3, (C) Concanamycin_A and (D) Ivermectin

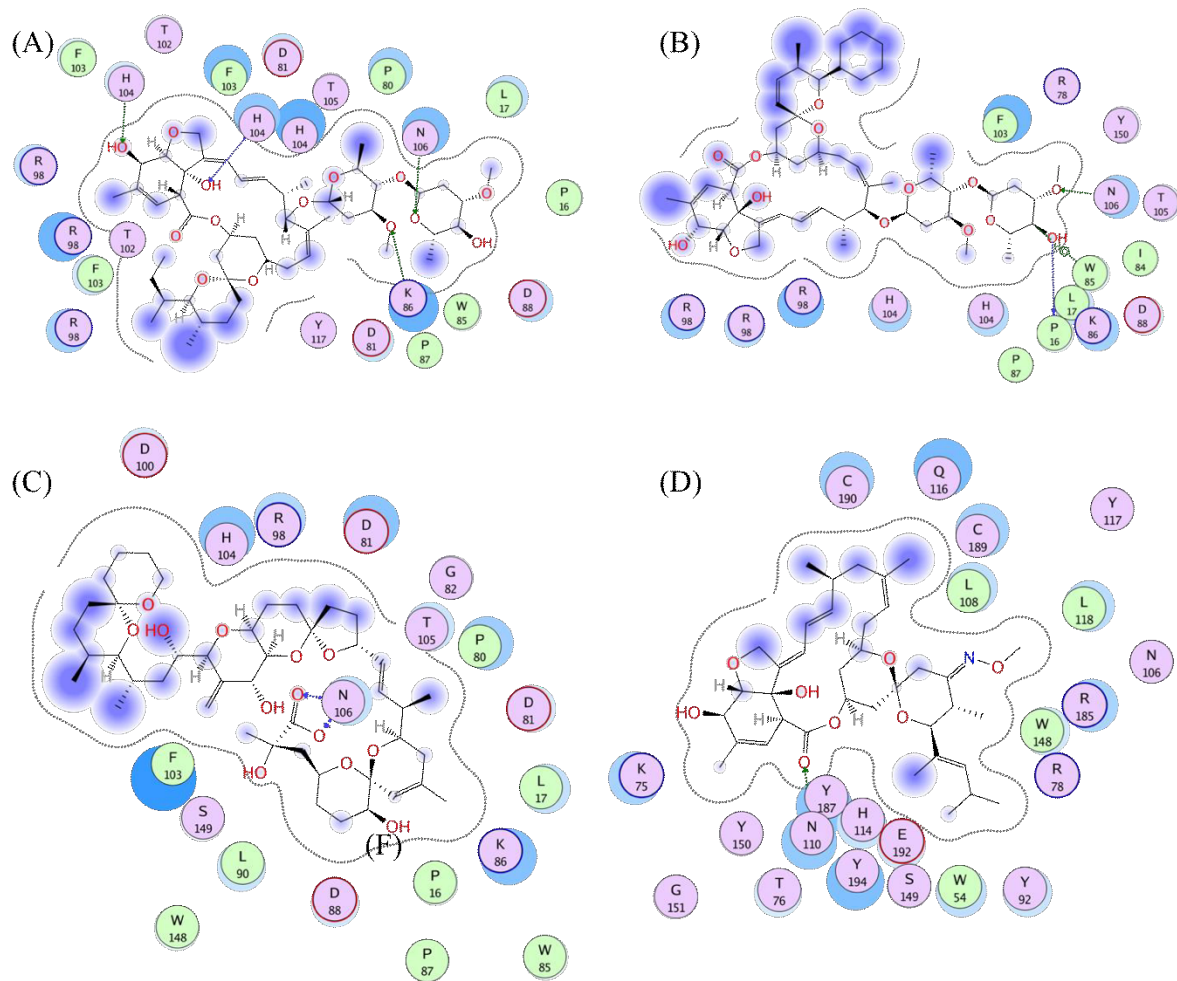


Figure 3.19.Ligand interaction plots of compounds selected for $\alpha 7nAChR$ inhibition. (A) Ivermectin, (B) Doramectin , (C) Okadaic acid, (D) Moxidectin.

The interaction mechanisms of ivermectin with the SARS-CoV-2 spike protein, CD147 and $\alpha 7nAChR$ were analysed using MOE software. Binding energies were obtained through the GBVI/WSA forcefield-based scoring function, which uses the AMBER99 forcefield to compute electrostatic, solvation, van der Waals and surface area contributions to the free energy given the ligand pose. Two to four hydrogen bond acceptor interactions were characterized in the best pose of the compounds in all receptors. Ivermectin remained in the same binding site for all the receptors during MD simulations ($2 \text{ \AA} < \text{RMSD} < 4 \text{ \AA}$). In case of the spike protein ($\text{RMSD} \sim 2.5 \text{ \AA}$), N61 (the main residue of the glycosylation site 10) were involved, with a binding energy of

-2.9 kcal/mol, with the benzofuran group of ivermectin and R415 were involved with the lactone group of ivermectin, with a binding energy of -2.9 kcal/mol (Figure 5A).

During MD simulations, CD147 underwent hinge movements which gave rise to a relatively higher (RMSD < 6 Å) value for ivermectin. Ivermectin stayed stable after 60 ns and strongly bound to CD147 through its disaccharide group, featuring E43 and K54 residues with -2.7 kcal/mol and -4.1 kcal/mol of binding energies, respectively, and a lactone core group featuring L46 residue with -1.1 kcal/mol of binding energy.

As for α 7nAChr, strong hydrogen bond acceptor interactions were found with K86 (-6.8 kcal/mol of binding energy) and N106 (-3 kcal/mol of binding energy). Moreover, it was characterized by an additional hydrophobic interaction with H85 (-2.7 kcal/mol of binding energy) (Figure 5C). In addition to maintaining disaccharide group binding with α 7nAChr through K86 and N106, the equilibrated structure formed an extra binding to α 7nAChr through its benzofuran group with H85 compared to the initial docking pose. Ivermectin maintained its attachment to α 7nAChr at the same binding site with (RMSD < 4 Å). The presence of the same type and number of interactions in the analyzed proteins may support the hypothesis of a multi-targeted action of ivermectin.

3.5. *Bioactivity of the Test Agents with Greatest Binding Strength*

According to Lipinski's rule of five, agents with a molecular mass greater than 500 would tend to be suboptimally bioactive as oral agents. However, although among these test agents, ivermectin and doramectin, for example, have molecular masses of 875.1 and 899.1, respectively, both are well-absorbed with similar pharmacokinetics [125]. Ivermectin, in particular, is distributed throughout the human body within eight hours of oral administration [83,126,127], and its success in combatting diseases affecting hundreds of millions of people is well established [70].

Conclusions

4. *Conclusions and future research*

This study presented a computational investigation based on molecular dynamic simulation and molecular docking to assess the binding possibility of ivermectin and 14 structurally similar compounds to four targets of interest (the spike, mutated spike protein, CD147 and $\alpha 7nAChr$) that are relevant for drug activity against COVID-19 during the interaction between the human host cell and the virus. Strong or moderate affinity bindings were found for ivermectin to multiple sites on the both the original and mutated spike protein, CD147 and $\alpha 7nAChr$, which could provide effective competitive bindings to all variants of the virus since D614G mutation is repeated in almost all the introduced variants. According to our calculations, ivermectin binds strongly to a glycosylation binding site (site 10: N61) of the spike protein S1-NTD and site 4 in mutated spike protein in the open position and to several other sites on S1 NTD and RBD. The potential binding affinity of ivermectin to CD147 is also examined. Ivermectin was found to bind to site 5, which is located in domain A of the CD147 protein, and to other sites on CD147, indicating that ivermectin might limit glycan bindings of SARS-CoV-2 at the host cell end as well. Among all the targets, ivermectin has the highest affinity to the $\alpha 7nAChr$ receptor. In this context, the high affinity of ivermectin and related compounds to $\alpha 7nAChr$ may both prevent viral entry and potentiate the activation of the cholinergic pathway and attenuate SARS-CoV-2-induced parasympathetic dysregulation by restoring the function of these receptors since the mutated spike protein difference is mainly within the S2 cleavage almost the result are comparable and expandable for both spike proteins. These preliminary results warrant further in vitro and in vivo testing of the 15 test compounds, ivermectin, an available and safe drug, against SARS-CoV-2 and all the new variants with the hope of containing the virus and limiting its morbidity.

Bibliography:

1. Hoffmann, M.; Kleine-Weber, H.; Schroeder, S.; Krüger, N.; Herrler, T.; Erichsen, S.; Schiergens, T.S.; Herrler, G.; Wu, N.H.; Nitsche, A.; et al. SARS-CoV-2 Cell Entry Depends on ACE2 and TMPRSS2 and Is Blocked by a Clinically Proven Protease Inhibitor. *Cell* **2020**, *181*, 271–280.e8.
2. Yang, J.; Petitjean, S.J.L.; Koehler, M.; Zhang, Q.; Dumitru, A.C.; Chen, W.; Derclaye, S.; Vincent, S.P.; Soumillion, P.; Alsteens, D. Molecular interaction and inhibition of SARS-CoV-2 binding to the ACE2 receptor. *Nat. Commun.* **2020**, *11*, 4541.
3. Aminpour, M.; Cannariato, M.; Zucco, A.; Di Gregorio, E.; Israel, S.; Perioli, A.; Tucci, D.; Rossi, F.; Pionato, S.; Marino, S.; et al. Computational Study of Potential Galectin-3 Inhibitors in the Treatment of COVID-19. *Biomedicines* **2021**, *9*, 1208.
4. Scheim, D.E. A Deadly Embrace: Hemagglutination Mediated by SARS-CoV-2 Spike Protein at its 22 N-Glycosylation Sites, Red Blood Cell Surface Sialoglycoproteins, and Antibody. *Int. J. Mol. Sci.* **2022**, *23*, 2558.
5. Changeux, J.P.; Amoura, Z.; Rey, F.A.; Miyara, M. A nicotinic hypothesis for COVID-19 with preventive and therapeutic implications. *Comptes Rendus Biol.* **2020**, *343*, 33–39.
6. Lagoumintzis, G.; Chasapis, C.T.; Alexandris, N.; Kouretas, D.; Tzartos, S.; Eliopoulos, E.; Farsalinos, K.; Poulas, K. Nicotinic cholinergic system and COVID-19: In Silico identification of interactions between alpha7 nicotinic acetylcholine receptor and the cryptic epitopes of SARS-Co-V and SARS-CoV-2 Spike glycoproteins. *Food Chem. Toxicol.* **2021**, *149*, 112009.
7. Lentz, T.L.; Burrage, T.G.; Smith, A.L.; Crick, J.; Tignor, G.H. Is the acetylcholine receptor a rabies virus receptor? *Science* **1982**, *215*, 182–184.
8. Chen, W.; Hui, Z.; Ren, X.; Luo, Y.; Shu, J.; Yu, H.; Li, Z. The N-glycosylation sites and Glycan-binding ability of S-protein in SARS-CoV-2 Coronavirus. *bioRxiv* **2020**. <https://doi.org/10.1101/2020.12.01.406025>.
9. Choi, Y.K.; Cao, Y.; Frank, M.; Woo, H.; Park, S.-J.; Yeom, M.S.; Croll, T.I.; Seok, C.; Im, W. Structure, Dynamics, Receptor Binding, and Antibody Binding of the Fully Glycosylated Full-Length SARS-CoV-2 Spike Protein in a Viral Membrane. *J. Chem. Theory Comput.* **2021**, *17*, 2479–2487.
10. Shajahan, A.; Supekar, N.T.; Gleinich, A.S.; Azadi, P. Deducing the N- and O-glycosylation profile of the spike protein of novel coronavirus SARS-CoV-2. *Glycobiology* **2020**, *30*, 981–988.
11. Watanabe, Y.; Allen, J.D.; Wrapp, D.; McLellan, J.S.; Crispin, M. Site-specific glycan analysis of the SARS-CoV-2 spike. *Science* **2020**, *369*, 330–333.
12. Baker, A.N.; Richards, S.-J.; Guy, C.S.; Congdon, T.R.; Hasan, M.; Zwetsloot, A.J.; Gallo, A.; Lewandowski, J.R.; Stansfeld, P.J.; Straube, A.; et al. The SARS-CoV-2 Spike Protein Binds Sialic Acids and Enables Rapid Detection in a Lateral Flow Point of Care Diagnostic Device. *ACS Cent. Sci.* **2020**, *6*, 2046–2052.
13. Bharara, R.; Singh, S.; Pattnaik, P.; Chitnis, C.E.; Sharma, A. Structural analogs of sialic acid interfere with the binding of erythrocyte binding antigen-175 to glycophorin A, an interaction crucial for erythrocyte invasion by Plasmodium falciparum. *Mol. Biochem. Parasitol.* **2004**, *138*, 123–129.
14. Stencel-Baerenwald, J.E.; Reiss, K.; Reiter, D.M.; Stehle, T.; Dermody, T.S. The sweet spot: Defining virus–sialic acid interactions. *Nat. Rev. Microbiol.* **2014**, *12*, 739–749.
15. Levine, S.; Levine, M.; Sharp, K.A.; Brooks, D.E. Theory of the electrokinetic behavior of human erythrocytes. *Biophys. J.* **1983**, *42*, 127–135.

16. Odièvre, M.-H.; Bony, V.; Benkerrou, M.; Lapoumériou, C.; Alberti, C.; Ducrocq, R.; Jacqz-Aigrain, E.; Elion, J.; Cartron, J.-P. Modulation of erythroid adhesion receptor expression by hydroxyurea in children with sickle cell disease. *Haematologica* **2008**, *93*, 502–510.
17. Bai, Y.; Huang, W.; Ma, L.T.; Jiang, J.L.; Chen, Z.N. Importance of N-glycosylation on CD147 for its biological functions. *Int. J. Mol. Sci.* **2014**, *15*, 6356–6377.
18. Silva-Filho, J.C.; de Melo, C.G.F.; de Oliveira, J.L. The influence of ABO blood groups on COVID-19 susceptibility and severity: A molecular hypothesis based on carbohydrate-carbohydrate interactions. *Med. Hypotheses* **2020**, *144*, 110155.
19. Modrof, J.; Kerschbaum, A.; Farcet, M.R.; Niemeyer, D.; Corman, V.M.; Kreil, T.R. SARS-CoV-2 and the safety margins of cell- based biological medicinal products. *Biologicals* **2020**, *68*, 122–124.
20. Lam, L.M.; Murphy, S.J.; Kuri-Cervantes, L.; Weisman, A.R.; Ittner, C.A.G.; Reilly, J.P.; Pampena, M.B.; Betts, M.R.; Wherry, E.J.; Song, W.-C.; et al. Erythrocytes Reveal Complement Activation in Patients with COVID-19. *MedRxiv* **2020**. <https://doi.org/10.1101/2020.05.20.20104398>.
21. Wang, K.; Chen, W.; Zhang, Z.; Deng, Y.; Lian, J.-Q.; Du, P.; Wei, D.; Zhang, Y.; Sun, X.-X.; Gong, L.; et al. CD147-spike protein is a novel route for SARS-CoV-2 infection to host cells. *Signal Transduct. Target. Ther.* **2020**, *5*, 283.
22. Bian, H.; Zheng, Z.-H.; Wei, D.; Wen, A.; Zhang, Z.; Lian, J.-Q.; Kang, W.-Z.; Hao, C.-Q.; Wang, J.; Xie, R.-H.; et al. Safety and efficacy of meplazumab in healthy volunteers and COVID-19 patients: A randomized phase 1 and an exploratory phase 2 trial. *Signal Transduct. Target. Ther.* **2021**, *6*, 194.
23. Hulswit, R.J.G.; Lang, Y.; Bakkers, M.J.G.; Li, W.; Li, Z.; Schouten, A.; Ophorst, B.; van Kuppeveld, F.J.M.; Boons, G.J.; Bosch, B.J.; et al. Human coronaviruses OC43 and HKU1 bind to 9-O-acetylated sialic acids via a conserved receptor-binding site in spike protein domain A. *Proc. Natl. Acad. Sci. USA* **2019**, *116*, 2681–2690.
24. Neu, U.; Bauer, J.; Stehle, T. Viruses and sialic acids: Rules of engagement. *Curr. Opin. Struct. Biol.* **2011**, *21*, 610–618.
25. Qing, E.; Hantak, M.; Perlman, S.; Gallagher, T. Distinct Roles for Sialoside and Protein Receptors in Coronavirus Infection. *MBio* **2020**, *11*, e02764–e02719.
26. Huang, X.; Dong, W.; Milewska, A.; Golda, A.; Qi, Y.; Zhu, Q.K.; Marasco, W.A.; Baric, R.S.; Sims, A.C.; Pyrc, K.; et al. Human Coronavirus HKU1 Spike Protein Uses O-Acetylated Sialic Acid as an Attachment Receptor Determinant and Employs Hemagglutinin-Esterase Protein as a Receptor-Destroying Enzyme. *J. Virol.* **2015**, *89*, 7202–7213.
27. Li, W.; Hulswit, R.J.G.; Widjaja, I.; Raj, V.S.; McBride, R.; Peng, W.; Widagdo, W.; Tortorici, M.A.; van Dieren, B.; Lang, Y.; et al. Identification of sialic acid-binding function for the Middle East respiratory syndrome coronavirus spike glycoprotein. *Proc. Natl. Acad. Sci. USA* **2017**, *114*, E8508–E8517.
28. Dai, X.; Zhang, X.; Ostrikov, K.; Abrahamyan, L. Host receptors: The key to establishing cells with broad viral tropism for vaccine production. *Crit. Rev. Microbiol.* **2020**, *46*, 147–168.
29. Koehler, M.; Delguste, M.; Sieben, C.; Gillet, L.; Alsteens, D. Initial Step of Virus Entry: Virion Binding to Cell-Surface Glycans. *Annu. Rev. Virol.* **2020**, *7*, 143–165.
30. Baum, J.; Ward, R.H.; Conway, D.J. Natural selection on the erythrocyte surface. *Mol. Biol. Evol.* **2002**, *19*, 223–229.
31. Varki, A.; Gagneux, P. Multifarious roles of sialic acids in immunity. *Ann. N. Y. Acad. Sci.* **2012**, *1253*, 16–36.
32. Zeng, Q.; Langereis, M.A.; van Vliet, A.L.W.; Huizinga, E.G.; de Groot, R.J. Structure of coronavirus hemagglutinin-esterase offers insight into corona and influenza virus evolution. *Proc. Natl. Acad. Sci. USA* **2008**, *105*, 9065–9069.

33. De Groot, R.J. Structure, function and evolution of the hemagglutinin-esterase proteins of corona- and rotaviruses. *Glycoconj. J.* **2006**, *23*, 59–72.
34. Bakkers, M.J.G.; Lang, Y.; Feitsma, L.J.; Hulswit, R.J.G.; de Poot, S.A.H.; van Vliet, A.L.W.; Margine, I.; de Groot-Mijnes, J.D.F.; van Kuppeveld, F.J.M.; Langereis, M.A.; et al. Betacoronavirus Adaptation to Humans Involved Progressive Loss of Hemagglutinin-Esterase Lectin Activity. *Cell Host Microbe* **2017**, *21*, 356–366.
35. Matrosovich, M.; Herrler, G.; Klenk, H.D. Sialic Acid Receptors of Viruses. In *SialoGlyco Chemistry and Biology II: Tools and Techniques to Identify and Capture Sialoglycans*; Gerardy-Schahn, R., Delannoy, P., von Itzstein, M., Eds.; Springer International Publishing: New York, NY, USA, 2015; pp. 1–28.
36. Miyagi, T.; Yamaguchi, K. 3.17—Sialic Acids. In *Comprehensive Glycoscience*; Kamerling, H., Ed.; Elsevier: Oxford, UK, 2007; pp. 297–323.
37. Wagner, R.; Matrosovich, M.; Klenk, H.D. Functional balance between haemagglutinin and neuraminidase in influenza virus infections. *Rev. Med. Virol.* **2002**, *12*, 159–166.
38. Lang, Y.; Li, W.; Li, Z.; Koerhuis, D.; van den Burg, A.C.S.; Rozemuller, E.; Bosch, B.-J.; van Kuppeveld, F.J.M.; Boons, G.-J.; Huizinga, E.G.; et al. Coronavirus hemagglutinin-esterase and spike proteins coevolve for functional balance and optimal virion avidity. *Proc. Natl. Acad. Sci. USA* **2020**, *117*, 25759–25770.
39. Chan, J.F.-W.; Kok, K.-H.; Zhu, Z.; Chu, H.; To, K.K.-W.; Yuan, S.; Yuen, K.-Y. Genomic characterization of the 2019 novel human-pathogenic coronavirus isolated from a patient with atypical pneumonia after visiting Wuhan. *Emerg. Microbes Infect.* **2020**, *9*, 221–236.
40. Chen, Y.; Liu, Q.; Guo, D. Emerging coronaviruses: Genome structure, replication, and pathogenesis. *J. Med. Virol.* **2020**, *92*, 418–423.
41. Zaki, A.M.; van Boheemen, S.; Bestebroer, T.M.; Osterhaus, A.D.; Fouchier, R.A. Isolation of a novel coronavirus from a man with pneumonia in Saudi Arabia. *N. Engl. J. Med.* **2012**, *367*, 1814–1820.
42. Couzin-Frankel, J. The mystery of the pandemic's 'happy hypoxia'. *Science* **2020**, *368*, 455–456.
43. Rapkiewicz, A.V.; Mai, X.; Carsons, S.E.; Pittaluga, S.; Kleiner, D.E.; Berger, J.S.; Thomas, S.; Adler, N.M.; Charytan, D.M.; Gasmi, B.; et al. Megakaryocytes and platelet-fibrin thrombi characterize multi-organ thrombosis at autopsy in COVID-19: A case series. *EClinicalMedicine* **2020**, *24*, 100434.
44. Lodigiani, C.; Lapichino, G.; Carenzo, L.; Cecconi, M.; Ferrazzi, P.; Sebastian, T.; Kucher, N.; Studt, J.D.; Sacco, C.; Alexia, B.; et al. Venous and arterial thromboembolic complications in COVID-19 patients admitted to an academic hospital in Milan, Italy. *Thromb. Res.* **2020**, *191*, 9–14.
45. Price, L.C.; McCabe, C.; Garfield, B.; Wort, S.J. Thrombosis and COVID-19 pneumonia: The clot thickens! *Eur. Respir. J.* **2020**, *56*, 2001608.
46. Tang, N.; Li, D.; Wang, X.; Sun, Z. Abnormal coagulation parameters are associated with poor prognosis in patients with novel coronavirus pneumonia. *J. Thromb. Haemost.* **2020**, *18*, 844–847.
47. Marini, J.J.; Gattinoni, L. Management of COVID-19 Respiratory Distress. *JAMA* **2020**, *323*, 2329–2330.
48. Liao, C.G.; Kong, L.M.; Song, F.; Xing, J.L.; Wang, L.X.; Sun, Z.J.; Tang, H.; Yao, H.; Zhang, Y.; Wang, L.; et al. Characterization of basigin isoforms and the inhibitory function of basigin-3 in human hepatocellular carcinoma proliferation and invasion. *Mol. Cell. Biol.* **2011**, *31*, 2591–2604.
49. Koch, C.; Staffler, G.; Hüttinger, R.; Hilgert, I.; Prager, E.; Cerný, J.; Steinlein, P.; Majdic, O.; Horejsí, V.; Stockinger, H. T cell activation-associated epitopes of CD147 in regulation of the T cell response, and their definition by antibody affinity and antigen density. *Int. Immunol.* **1999**, *11*, 777–786.
50. Lv, M.; Miao, J.; Zhao, P.; Luo, X.; Han, Q.; Wu, Z.; Zhang, K.; Zhu, P. CD147-mediated chemotaxis of CD4(+)CD161(+) T cells may contribute to local inflammation in rheumatoid arthritis. *Clin. Rheumatol.* **2018**, *37*, 59–66.

51. Schmidt, R.; Bültmann, A.; Fischel, S.; Gillitzer, A.; Cullen, P.; Walch, A.; Jost, P.; Ungerer, M.; Tolley, N.D.; Lindemann, S.; et al. Extracellular matrix metalloproteinase inducer (CD147) is a novel receptor on platelets, activates platelets, and augments nuclear factor kappaB-dependent inflammation in monocytes. *Circ. Res.* **2008**, *102*, 302–309.
52. Loh, D. The potential of melatonin in the prevention and attenuation of oxidative hemolysis and myocardial injury from cd147 SARS-CoV-2 spike protein receptor binding. *Melatonin Res.* **2020**, *3*, 380–416.
53. Joseph, J.; Knobler, R.L.; Lublin, F.D.; Burns, F.R. Regulation of the expression of intercellular adhesion molecule-1 (ICAM-1) and the putative adhesion molecule Basigin on murine cerebral endothelial cells by MHV-4 (JHM). *Adv. Exp. Med. Biol.* **1993**, *342*, 389–391.
54. De Back, D.Z.; Kostova, E.; Klei, T.; Beuger, B.; van Zwieten, R.; Kuijpers, T.; Juffermans, N.; van den Berg, T.; Korte, D.; van Kraaij, M.; et al. RBC Adhesive Capacity Is Essential for Efficient 'Immune Adherence Clearance' and Provide a Generic Target to Deplete Pathogens from Septic Patients. *Blood* **2016**, *128*, 1031.
55. Telen, M.J. Red blood cell surface adhesion molecules: Their possible roles in normal human physiology and disease. *Semin. Hematol.* **2000**, *37*, 130–142.
56. Yurchenko, V.; Constant, S.; Bukrinsky, M. Dealing with the family: CD147 interactions with cyclophilins. *Immunology* **2006**, *117*, 301–309.
57. Schulz, C.; von Brühl, M.L.; Barocke, V.; Cullen, P.; Mayer, K.; Okrojek, R.; Steinhart, A.; Ahmad, Z.; Kremmer, E.; Nieswandt, B.; et al. EMMPRIN (CD147/basigin) mediates platelet-monocyte interactions in vivo and augments monocyte recruitment to the vascular wall. *J. Thromb. Haemost.* **2011**, *9*, 1007–1019.
58. Von Ungern-Sternberg, S.N.I.; Zerneck, A.; Seizer, P. Extracellular Matrix Metalloproteinase Inducer EMMPRIN (CD147) in Cardiovascular Disease. *Int. J. Mol. Sci.* **2018**, *19*, 507.
59. Yee, C.; Main, N.M.; Terry, A.; Stevanovski, I.; Maczurek, A.; Morgan, A.J.; Calabro, S.; Potter, A.J.; Iemma, T.L.; Bowen, D.G.; et al. CD147 mediates intrahepatic leukocyte aggregation and determines the extent of liver injury. *PLoS ONE* **2019**, *14*, e0215557.
60. Pennings, G.J.; Kritharides, L. CD147 in cardiovascular disease and thrombosis. *Semin. Thromb. Hemost.* **2014**, *40*, 747–755.
61. Carbajo-Lozoya, J.; Ma-Lauer, Y.; Malešević, M.; Theuerkorn, M.; Kahlert, V.; Prell, E.; von Brunn, B.; Muth, D.; Baumert, T.F.; Drosten, C.; et al. Human coronavirus NL63 replication is cyclophilin A-dependent and inhibited by non-immunosuppressive cyclosporine A-derivatives including Alisporivir. *Virus Res.* **2014**, *184*, 44–53.
62. Chen, Z.; Mi, L.; Xu, J.; Yu, J.; Wang, X.; Jiang, J.; Xing, J.; Shang, P.; Qian, A.; Li, Y.; et al. Function of HAb18G/CD147 in invasion of host cells by severe acute respiratory syndrome coronavirus. *J. Infect. Dis.* **2005**, *191*, 755–760.
63. Pushkarsky, T.; Zybarth, G.; Dubrovsky, L.; Yurchenko, V.; Tang, H.; Guo, H.; Toole, B.; Sherry, B.; Bukrinsky, M. CD147 facilitates HIV-1 infection by interacting with virus-associated cyclophilin A. *Proc. Natl. Acad. Sci. USA* **2001**, *98*, 6360–6365.
64. Muramatsu, T. Basigin (CD147), a multifunctional transmembrane glycoprotein with various binding partners. *J. Biochem.* **2016**, *159*, 481–490.
65. Zhu, X.; Song, Z.; Zhang, S.; Nanda, A.; Li, G. CD147: A Novel Modulator of Inflammatory and Immune Disorders. *Curr. Med. Chem.* **2014**, *21*, 2138–2145.
66. Dayer, M. Coronavirus (2019-nCoV) Deactivation via Spike Glycoprotein Shielding by Old Drugs, Bioinformatic Study. *Preprints.Org.* **2020**. <https://doi.org/10.20944/preprints202005.0020.v1>.

67. Nallusamy, S.; Mannu, J.; Ravikumar, C.; Angamuthu, K.; Nathan, B.; Nachimuthu, K.; Ramasamy, G.; Muthurajan, R.; Subbarayalu, M.; Neelakandan, K. Shortlisting Phytochemicals Exhibiting Inhibitory Activity against Major Proteins of SARS- CoV-2 through Virtual Screening. *Res. Sq.* **2020**. <https://doi.org/10.21203/rs.3.rs-31834/v1>.
68. Suravajhala, R.; Parashar, A.; Malik, B.; Nagaraj, V.A.; Padmanaban, G.; Kavi Kishor, P.B.; Polavarapu, R.; Suravajhala, P. Comparative Docking Studies on Curcumin with COVID-19 Proteins. *Preprints.Org.* **2020**. <https://doi.org/10.20944/preprints202005.0439.v2>.
69. Kalhor, H.; Sadeghi, S.; Abolhasani, H.; Kalhor, R.; Rahimi, H. Repurposing of the approved small molecule drugs in order to inhibit SARS-CoV-2 S protein and human ACE2 interaction through virtual screening approaches. *J. Biomol. Struct. Dyn.* **2020**, *40*, 1299–1315.
70. Yagisawa, M.; Foster, P.J.; Hanaki, H.; Omura, S. Global Trends in Clinical Studies of Ivermectin in COVID-19. *Jpn. J. Antibiot.* **2021**, *74*, 44–95.
71. Campbell, W.C. History of avermectin and ivermectin, with notes on the history of other macrocyclic lactone antiparasitic agents. *Curr. Pharm. Biotechnol.* **2012**, *13*, 853–865.
72. Juarez, M.; Schcolnik-Cabrera, A.; Dueñas-Gonzalez, A. The multitargeted drug ivermectin: From an antiparasitic agent to a repositioned cancer drug. *Am. J. Cancer Res.* **2018**, *8*, 317–331.
73. Rizzo, E. Ivermectin, antiviral properties and COVID-19: A possible new mechanism of action. *Naunyn Schmiedebergs Arch. Pharm.* **2020**, *393*, 1153–1156.
74. Lehrer, S.; R Feinstein, P.H. Ivermectin Docks to the SARS-CoV-2 Spike Receptor-binding Domain Attached to ACE2. *Vivo* **2020**, *34*, 3023–3026.
75. Maurya, D. A Combination of Ivermectin and Doxycycline Possibly Blocks the Viral Entry and Modulate the Innate Immune Response in COVID-19 Patients. *ChemRxiv* **2020**. <https://doi.org/10.26434/chemrxiv.12630539.v1>.
76. Dasgupta, J.; Sen, U.; Bakashi, A.; Dasgupta, A. Nsp7 and Spike Glycoprotein of SARS-CoV-2 Are Envisaged as Potential Targets of Vitamin D and Ivermectin. *Preprints.Org.* **2020**. <https://doi.org/10.20944/preprints202005.0084.v1>.
77. Kaur, H.; Shekhar, N.; Sharma, S.; Sarma, P.; Prakash, A.; Medhi, B. Ivermectin as a potential drug for treatment of COVID-19: An in-sync review with clinical and computational attributes. *Pharmacol. Rep.* **2021**, *73*, 736–749. <https://doi.org/10.1007/s43440-020-00195-y>.
78. Saha, J.K.; Raihan, J. The Binding mechanism of Ivermectin and levosalbutamol with spike protein of SARS-CoV-2. *Struct. Chem.* **2021**, *32*, 1985–1992.
79. Hussien, M.A.; Abdelaziz, A.E.M. Molecular docking suggests repurposing of brincidofovir as a potential drug targeting SARS- CoV-2 ACE2 receptor and main protease. *Netw. Modeling Anal. Health Inform. Bioinform.* **2020**, *9*, 56.
80. Santin, A.D.; Scheim, D.E.; McCullough, P.A.; Yagisawa, M.; Borody, T.J. Ivermectin: A multifaceted drug of Nobel prize- honored distinction with indicated efficacy against a new global scourge, COVID-19. *New Microbes New Infect.* **2021**, *43*, 100924.
81. Kory, P.; Meduri, G.U.; Varon, J.; Iglesias, J.; Marik, P.E. Review of the Emerging Evidence Demonstrating the Efficacy of Ivermectin in the Prophylaxis and Treatment of COVID-19. *Am. J. Ther.* **2021**, *28*, e299–e318.
82. Crump, A.; Ōmura, S. Ivermectin, 'wonder drug' from Japan: The human use perspective. *Proc. Jpn. Acad. Ser. B Phys. Biol. Sci.* **2011**, *87*, 13–28.
83. Guzzo, C.A.; Furtek, C.I.; Porras, A.G.; Chen, C.; Tipping, R.; Clineschmidt, C.M.; Sciberras, D.G.; Hsieh, J.Y.; Lasseter, K.C. Safety, tolerability, and pharmacokinetics of escalating high doses of ivermectin in healthy adult subjects. *J. Clin. Pharm.* **2002**, *42*, 1122–1133.

84. Navarro, M.; Camprubí, D.; Requena-Méndez, A.; Buonfrate, D.; Giorli, G.; Kamgno, J.; Gardon, J.; Boussinesq, M.; Muñoz, J.; Krolewiecki, A. Safety of high-dose ivermectin: A systematic review and meta-analysis. *J. Antimicrob. Chemother.* **2020**, *75*, 827–834.
85. *The 2015 Nobel Prize in Physiology or Medicine—Press Release*; The Nobel Assembly at Karolinska Institutet: Solna, Sweden, 2015. Available online: <https://www.nobelprize.org/prizes/medicine/2015/press-release/> (accessed on 22 February 2022).
86. Caly, L.; Druce, J.D.; Catton, M.G.; Jans, D.A.; Wagstaff, K.M. The FDA-approved drug ivermectin inhibits the replication of SARS-CoV-2 in vitro. *Antivir. Res.* **2020**, *178*, 104787.
87. Momekov, G.; Momekova, D. Ivermectin as a potential COVID-19 treatment from the pharmacokinetic point of view: Antiviral levels are not likely attainable with known dosing regimens. *Biotechnol. Biotechnol. Equip.* **2020**, *34*, 469–474.
88. Schmith, V.D.; Zhou, J.J.; Lohmer, L.R.L. The Approved Dose of Ivermectin Alone is not the Ideal Dose for the Treatment of COVID-19. *Clin. Pharm.* **2020**, *108*, 762–765.
89. Krause, R.M.; Buisson, B.; Bertrand, S.; Corringer, P.J.; Galzi, J.L.; Changeux, J.P.; Bertrand, D. Ivermectin: A positive allosteric effector of the $\alpha 7$ neuronal nicotinic acetylcholine receptor. *Mol. Pharm.* **1998**, *53*, 283–294.
90. Wang, H.; Yu, M.; Ochani, M.; Amella, C.A.; Tanovic, M.; Susarla, S.; Li, J.H.; Wang, H.; Yang, H.; Ulloa, L.; et al. Nicotinic acetylcholine receptor $\alpha 7$ subunit is an essential regulator of inflammation. *Nature* **2003**, *421*, 384–388.
91. Ren, C.; Tong, Y.L.; Li, J.C.; Lu, Z.Q.; Yao, Y.M. The Protective Effect of Alpha 7 Nicotinic Acetylcholine Receptor Activation on Critical Illness and Its Mechanism. *Int. J. Biol. Sci.* **2017**, *13*, 46–56.
92. Fajgenbaum, D.C.; June, C.H. Cytokine Storm. *N. Engl. J. Med.* **2020**, *383*, 2255–2273.
93. Rajter, J.C.; Sherman, M.S.; Fatteh, N.; Vogel, F.; Sacks, J.; Rajter, J.-J. Use of Ivermectin is Associated with Lower Mortality in Hospitalized Patients with COVID-19 (ICON study). *Chest* **2020**, *159*, 85–92.
94. de Melo, G.D.; Lazarini, F.; Levallois, S.; Hautefort, C.; Michel, V.; Larrous, F.; Verillaud, B.; Aparicio, C.; Wagner, S.; Gheusi, G.; et al. COVID-19-related anosmia is associated with viral persistence and inflammation in human olfactory epithelium and brain infection in hamsters. *Sci Transl Med* **2021**, *13*, eabf8396.
95. Chaccour, C.; Casellas, A.; Blanco-Di Matteo, A.; Pineda, I.; Fernandez-Montero, A.; Ruiz-Castillo, P.; Richardson, M.-A.; Rodríguez-Mateos, M.; Jordán-Iborra, C.; Brew, J.; et al. The effect of early treatment with ivermectin on viral load, symptoms and humoral response in patients with non-severe COVID-19: A pilot, double-blind, placebo-controlled, randomized clinical trial. *EClinicalMedicine* **2021**, *32*, 100720.
96. Shang, J.; Wan, Y.; Luo, C.; Ye, G.; Geng, Q.; Auerbach, A.; Li, F. Cell entry mechanisms of SARS-CoV-2. *Proc. Natl. Acad. Sci. USA* **2020**, *117*, 11727–11734.
97. Li, F. Structure, Function, and Evolution of Coronavirus Spike Proteins. *Annu. Rev. Virol.* **2016**, *3*, 237–261.
98. Hulswit, R.J.G.; de Haan, C.A.M.; Bosch, B.J. Chapter Two—Coronavirus Spike Protein and Tropism Changes. In *Advances in Virus Research*, Ziebuhr, J., Ed.; Academic Press: New York, NY, USA, 2016; Volume 96, pp. 29–57.
99. Huang, Y.; Yang, C.; Xu, X.-F.; Xu, W.; Liu, S.-W. Structural and functional properties of SARS-CoV-2 spike protein: Potential antivirus drug development for COVID-19. *Acta Pharmacol. Sin.* **2020**, *41*, 1141–1149.
100. Awasthi, M.; Gulati, S.; Sarkar, D.; Tiwari, S.; Kateriya, S.; Ranjan, P.; Verma, S.K. The Sialoside-Binding Pocket of SARS-CoV-2 Spike Glycoprotein Structurally Resembles MERS-CoV. *Viruses* **2020**, *12*, 909.

101. Fantini, J.; Di Scala, C.; Chahinian, H.; Yahi, N. Structural and molecular modelling studies reveal a new mechanism of action of chloroquine and hydroxychloroquine against SARS-CoV-2 infection. *Int. J. Antimicrob. Agents* **2020**, *55*, 105960.
102. Tortorici, M.A.; Walls, A.C.; Lang, Y.; Wang, C.; Li, Z.; Koerhuis, D.; Boons, G.J.; Bosch, B.J.; Rey, F.A.; de Groot, R.J.; et al. Structural basis for human coronavirus attachment to sialic acid receptors. *Nat. Struct. Mol. Biol.* **2019**, *26*, 481–489.
103. Milanetti, E.; Miotto, M.; Rienzo, L.D.; Monti, M.; Gosti, G.; Ruocco, G. In-Silico evidence for two receptors based strategy of SARS-CoV-2. *bioRxiv* **2020**. <https://doi.org/10.1101/2020.03.24.006197>.
104. Mornioli, D.; Gianni, M.L.; Consales, A.; Pietrasanta, C.; Mosca, F. Human Sialome and Coronavirus Disease-2019 (COVID-19) Pandemic: An Understated Correlation? *Front. Immunol.* **2020**, *11*, 1480.
105. Wrapp, D.; Wang, N.; Corbett, K.S.; Goldsmith, J.A.; Hsieh, C.-L.; Abiona, O.; Graham, B.S.; McLellan, J.S. Cryo-EM structure of the 2019-nCoV spike in the prefusion conformation. *Science* **2020**, *367*, 1260–1263.
106. Sikora, M.; von Bülow, S.; Blanc, F.E.C.; Gecht, M.; Covino, R.; Hummer, G. Computational epitope map of SARS-CoV-2 spike protein. *PLoS Comput. Biol.* **2021**, *17*, e1008790.
107. DrugBank Online Database, Ivermectin (DB00602). Available online: https://go.drugbank.com/structures/search/small_molecule_drugs/structure?database_id=DB00602&search_type=similarity#results (accessed on 21 February 2022).
108. CHARMM-GUI Archive—COVID-19 Proteins Library. Available online: <https://www.charmm-gui.org/?doc=archive&lib=covid19> (accessed on 21 February 2022).
109. Jo, S.; Kim, T.; Iyer, V.G.; Im, W. CHARMM-GUI: A web-based graphical user interface for CHARMM. *J. Comput. Chem.* **2008**, *29*, 1859–1865.
110. Woo, H.; Park, S.-J.; Choi, Y.K.; Park, T.; Tanveer, M.; Cao, Y.; Kern, N.R.; Lee, J.; Yeom, M.S.; Croll, T.I.; et al. Developing a Fully Glycosylated Full-Length SARS-CoV-2 Spike Protein Model in a Viral Membrane. *J. Phys. Chem. B* **2020**, *124*, 7128–7137.
111. Noviello, C.M.; Gharpure, A.; Mukhtasimova, N.; Cabuco, R.; Baxter, L.; Borek, D.; Sine, S.M.; Hibbs, R.E. Structure and gating mechanism of the $\alpha 7$ nicotinic acetylcholine receptor. *Cell* **2021**, *184*, 2121–2134. e13.
112. *Molecular Operating Environment (MOE)*; ULC, Chemical Computing Group: Montreal, QC, Canada, 2019.
113. Behloul, N.; Baha, S.; Shi, R.; Meng, J. Role of the GTNGTKR motif in the N-terminal receptor-binding domain of the SARS-CoV-2 spike protein. *Virus Res.* **2020**, *286*, 198058.
114. Di Gaetano, S.; Capasso, D.; Delre, P.; Pirone, L.; Saviano, M.; Pedone, E.; Mangiatordi, G.F. More Is Always Better Than One: The N-Terminal Domain of the Spike Protein as Another Emerging Target for Hampering the SARS-CoV-2 Attachment to Host Cells. *Int. J. Mol. Sci.* **2021**, *22*, 6462.
115. *Schrödinger Release 2019-4: SiteMap*; Schrödinger, LLC.: New York, NY, USA, 2019.
116. Bangaru, S.; Ozorowski, G.; Turner, H.L.; Antanasijevic, A.; Huang, D.; Wang, X.; Torres, J.L.; Diedrich, J.K.; Tian, J.-H.; Portnoff, A.D.; et al. Structural analysis of full-length SARS-CoV-2 spike protein from an advanced vaccine candidate. *bioRxiv* **2020**. <https://doi.org/10.1101/2020.08.06.234674>.
117. Carino, A.; Moraca, F.; Fiorillo, B.; Marchiano, S.; Sepe, V.; Biagioli, M.; Finamore, C.; Bozza, S.; Francisci, D.; Distretti, E.; et al. Hijacking SARS-CoV-2/ACE2 Receptor Interaction by Natural and Semi-synthetic Steroidal Agents Acting on Functional Pockets on the Receptor Binding Domain. *Front. Chem.* **2020**, *8*, 572885.
118. Trott, O.; Olson, A.J. AutoDock Vina: Improving the speed and accuracy of docking with a new scoring function, efficient optimization, and multithreading. *J. Comput. Chem.* **2010**, *31*, 455–461.
119. Case, D.; Aktulga, H.; Belfon, K.; Ben-Shalom, I.; Brozell, S.; Cerutti, D.; Cheatham, I.T.E.; Cisneros, G. Amber 2021. Available online: <https://ambermd.org/index.php> (accessed on 21 February 2022).

120. Preto, J.; Gentile, F. Assessing and improving the performance of consensus docking strategies using the DockBox package. *J. Comput. Aided Mol. Des.* **2019**, *33*, 817–829.
121. Graves, A.P.; Brenk, R.; Shoichet, B.K. Decoys for docking. *J. Med. Chem.* **2005**, *48*, 3714–3728.
122. Mysinger, M.M.; Carchia, M.; Irwin, J.J.; Shoichet, B.K. Directory of useful decoys, enhanced (DUD-E): Better ligands and decoys for better benchmarking. *J. Med. Chem.* **2012**, *55*, 6582–6594.
123. Huang, N.; Shoichet, B.K.; Irwin, J.J. Benchmarking sets for molecular docking. *J. Med. Chem.* **2006**, *49*, 6789–6801.
124. Casalino, L.; Gaieb, Z.; Goldsmith, J.A.; Hjorth, C.K.; Dommer, A.C.; Harbison, A.M.; Fogarty, C.A.; Barros, E.P.; Taylor, B.C.; McLellan, J.S.; et al. Beyond Shielding: The Roles of Glycans in the SARS-CoV-2 Spike Protein. *ACS Cent. Sci.* **2020**, *6*, 1722–1734.
125. Toutain, P.L.; Upson, D.W.; Terhune, T.N.; McKenzie, M.E. Comparative pharmacokinetics of doramectin and ivermectin in cattle. *Vet. Parasitol.* **1997**, *72*, 3–8.
126. González Canga, A.; Sahagún Prieto, A.M.; Díez Liébana, M.J.; Fernández Martínez, N.; Sierra Vega, M.; García Vieitez, J.J. The Pharmacokinetics and Interactions of Ivermectin in Humans—A Mini-review. *AAPS J.* **2008**, *10*, 42–46.
127. Muñoz, J.; Ballester, M.R.; Antonijoan, R.M.; Gich, I.; Rodríguez, M.; Colli, E.; Gold, S.; Krolewiecki, A.J. Safety and pharmacokinetic profile of fixed-dose ivermectin with an innovative 18mg tablet in healthy adult volunteers. *PLoS Negl. Trop. Dis.* **2018**, *12*, e0006020.
128. Duhovny, D.; Nussinov, R.; Wolfson, H.J. *Efficient Unbound Docking of Rigid Molecules*; Springer: Berlin/Heidelberg, Germany, 2002; pp. 185–200.
129. Schneidman-Duhovny, D.; Inbar, Y.; Nussinov, R.; Wolfson, H.J. PatchDock and SymmDock: Servers for rigid and symmetric docking. *Nucleic Acids Res.* **2005**, *33*, W363–W367.
130. Farsalinos, K.; Eliopoulos, E.; Leonidas, D.D.; Papadopoulos, G.E.; Tzartos, S.; Poulas, K. Nicotinic Cholinergic System and COVID-19: In Silico Identification of an Interaction between SARS-CoV-2 and Nicotinic Receptors with Potential Therapeutic Targeting Implications. *Int. J. Mol. Sci.* **2020**, *21*, 5807.
131. Gao, C.; Zeng, J.; Jia, N.; Stavenhagen, K.; Matsumoto, Y.; Zhang, H.; Li, J.; Hume, A.J.; Mühlberger, E.; van Die, I.; et al. SARS-CoV-2 Spike Protein Interacts with Multiple Innate Immune Receptors. *bioRxiv* **2020**. <https://doi.org/10.1101/2020.07.29.227462>.
132. Cohen, M.; Varki, A. Chapter Three—Modulation of Glycan Recognition by Clustered Saccharide Patches. In *International Review of Cell and Molecular Biology*; Jeon, K.W., Ed.; Academic Press: New York, NY, USA, 2014; Volume 308, pp. 75–125.
133. Jaskiewicz, E.; Jodłowska, M.; Kaczmarek, R.; Zerka, A. Erythrocyte glycoporphins as receptors for Plasmodium merozoites. *Parasites Vectors* **2019**, *12*, 317.
134. Anderson, H.L.; Brodsky, I.E.; Mangalmurti, N.S. The Evolving Erythrocyte: Red Blood Cells as Modulators of Innate Immunity. *J. Immunol.* **2018**, *201*, 1343–1351.
135. Chang, M.W.; Lindstrom, W.; Olson, A.J.; Belew, R.K. Analysis of HIV Wild-Type and Mutant Structures via In Silico Docking against Diverse Ligand Libraries. *J. Chem. Inf. Modeling* **2007**, *47*, 1258–1262.
136. Mol-Instincts, Structure of IVERMECTIN (C₄₈H₇₄O₁₄), Interactive 3-Dimensional (3D) Visualization. Available online: <https://www.molinstincts.com/structure/IVERMECTIN-cstr-CT1079779157.html> (accessed on 21 February 2022).
137. Ke, Z.; Oton, J.; Qu, K.; Cortese, M.; Zila, V.; McKeane, L.; Nakane, T.; Zivanov, J.; Neufeldt, C.J.; Cerikan, B.; et al. Structures and distributions of SARS-CoV-2 spike proteins on intact virions. *Nature* **2020**, *588*, 498–502.

138. Kiss, B.; Kis, Z.; Pályi, B.; Kellermayer, M.S.Z. Topography, Spike Dynamics, and Nanomechanics of Individual Native SARS-CoV-2 Virions. *Nano Lett.* **2021**, *21*, 2675–2680.
139. Xu, H.; Shaw, D.E. A Simple Model of Multivalent Adhesion and Its Application to Influenza Infection. *Biophys. J.* **2016**, *110*, 218–233.
140. Cardinale, A.; Nastrucci, C.; Cesario, A.; Russo, P. Nicotine: Specific role in angiogenesis, proliferation and apoptosis. *Crit. Rev. Toxicol.* **2012**, *42*, 68–89.
141. Macklin, K.D.; Maus, A.D.; Pereira, E.F.; Albuquerque, E.X.; Conti-Fine, B.M. Human vascular endothelial cells express functional nicotinic acetylcholine receptors. *J. Pharm. Exp.* **1998**, *287*, 435–439.
142. Gordan, R.; Gwathmey, J.K.; Xie, L.H. Autonomic and endocrine control of cardiovascular function. *World J. Cardiol.* **2015**, *7*, 204–214.
143. Lei, Y.; Zhang, J.; Schiavon, C.R.; He, M.; Chen, L.; Shen, H.; Zhang, Y.; Yin, Q.; Cho, Y.; Andrade, L.; et al. SARS-CoV-2 Spike Protein Impairs Endothelial Function via Downregulation of ACE 2. *Circ. Res.* **2021**, *128*, 1323–1326.
144. Walls AC, Park Y-J, Tortorici MA, Wall A, McGuire AT, Velesler D. Structure, function and antigenicity of the SARS-CoV-2 spike glycoprotein. *bioRxiv*. 2020;:2020.02.19.956581.
145. Roy A, Kucukural A, Zhang Y. I-TASSER: a unified platform for automated protein structure and function prediction. *Nat Protoc.* 2010;5:725–38.
146. Yang J, Zhang Y. Protein Structure and Function Prediction Using I-TASSER. *Curr Protoc Bioinformatics.* 2015;52:5.8.1-5.815.
147. Yuan Y, Cao D, Zhang Y, Ma J, Qi J, Wang, Q. et al. RCSB PDB - 5X58: Prefusion structure of SARS-CoV spike glycoprotein, conformation 1. 2017. doi:10.2210/pdb5x58/pdb.
148. Xu J, Zhang Y. How significant is a protein structure similarity with TM-score = 0.5? *Bioinformatics.* 2010;26:889–95.
149. Kabsch W, Sander C. Dictionary of protein secondary structure: pattern recognition of hydrogen-bonded and geometrical features. *Biopolymers.* 1983;22:2577–637.
150. Thomas G. Furin at the cutting edge: from protein traffic to embryogenesis and disease. *Nat Rev Mol Cell Biol.* 2002;3:753–66.
151. Bestle D, Heindl MR, Limburg H, van TVL, Pilgram O, Moulton H, et al. TMPRSS2 and furin are both essential for proteolytic activation and spread of SARS-CoV-2 in human airway epithelial cells and provide promising drug targets. preprint. *Microbiology*; 2020. doi:10.1101/2020.04.15.042085.
152. Dahms SO, Arciniega M, Steinmetzer T, Huber R, Than ME. Structure of the unliganded form of the proprotein convertase furin suggests activation by a substrate-induced mechanism. *Proc Natl Acad Sci U S A.* 2016;113:11196–201.
153. Jencks WP. *Catalysis in chemistry and enzymology.* New York: Dover; 1987. 28. Gonzalez-Reiche AS, Hernandez MM, Sullivan M, Ciferri B, Alshammary H, Obla A, et al. *Introductions*
154. Korber, B.; Fischer, W. M.; Gnanakaran, S.; Yoon, H.; Theiler, J.; Abfalterer, W.; Hengartner, N.; Giorgi, E. E.; Bhattacharya, T.; Foley, B.; Hastie, K. M.; Parker, M. D.; Partridge, D. G.; Evans, C. M.; Freeman, T. M.; de Silva, T. I.; McDanal, C.; Perez, L. G.; Tang, H.; Moon-Walker, A.; Whelan, S. P.; LaBranche, C. C.; Saphire, E. O.; Montefiori, D. C. Tracking changes in SARS-CoV-2 Spike: evidence that D614G increases infectivity of the COVID-19 virus. *Cell* 2020, *182*, 1–16 on behalf of the Sheffield COVID-19 Genomics Group.
155. Hu, J.; He, C.-L.; Gao, Q.-Z.; Zhang, G.-J.; Cao, X.-X.; Long, Q.-X.; Deng, H.-J.; Huang, L.-Y.; Chen, J.; Wang, K.; Tang, N.; Huang, A.-L. The D614G mutation of SARS-CoV-2 spike protein enhances viral

- infectivity and decreases neutralization sensitivity to individual convalescent sera. *boRxiv* 2020, 06.20.161323. DOI: 10.1101/2020.06.20.161323.
156. Ozono, S.; Zhang, Y.; Ode, H.; Seng, T. T.; Imai, K.; Miyoshi, K.; Kishigami, S.; Ueno, T.; Iwatani, Y.; Suzuki, T.; Tokunaga, K. Naturally mutated spike proteins of SARS-CoV-2 variants show differential levels of cell entry. *boRxiv* 2020, 06.15.151779. DOI: 10.1101/2020.06.15.151779.
 157. Zhang, L.; Jackson, C. B.; Mou, H.; Ojha, A.; Rangarajan, E. S.; Izard, T.; Farzan, M.; Choe, H. The D614G mutation in the SARS-CoV-2 spike protein reduces S1 shedding and increases infectivity. *boRxiv* 2020, 06.12.148726. DOI: 10.1101/2020.06.12.148726.
 158. Ferañ dez, A. *Physics at the Biomolecular Interface: Fundamentals for Molecular Targeted Therapy*; Springer International Publishing: Switzerland, 2016; Chapters 1–3.
 159. Fernández, A.; Crespo, A. Protein wrapping: a marker for association, aggregation and molecular targeted therapy. *Chem. Soc. Rev.* 2008, 37, 2373–2382.
 160. Ferañ dez, A.; Scheraga, H. A. Insufficiently dehydrated hydrogen bonds as determinants for protein interactions. *Proc. Natl. Acad. Sci. U. S. A.* 2003, 100, 113–118.
 161. Fernández, A. Stickiness of the hydrogen bond. *Ann. Phys. (Berlin, Ger.)* 2018, 530, 1800162.
 162. Fernández, Ariel. "Structural impact of mutation D614G in SARS-CoV-2 spike protein: enhanced infectivity and therapeutic opportunity." *ACS medicinal chemistry letters* 11.9 (2020): 1667-1670.
 163. Zhou P, Yang XL, Wang XG, Hu B, Zhang L, Zhang W, Si HR, Zhu Y, Li B, Huang CL et al.: A pneumonia outbreak associated with a new coronavirus of probable bat origin. *Nature* 2020, 579:270- 273
 164. Barcena M, Barnes CO, Beck M, Bjorkman PJ, Canard B, Gao GF, Gao Y, Hilgenfeld R, Hummer G, Patwardhan A et al.: Structural biology in the fight against COVID-19. *Nat Struct Mol Biol* 2021, 28:2-7.
 165. Hoffmann M, Kleine-Weber H, Schroeder S, Kruger N, Herrler T, Erichsen S, Schiergens TS, Herrler G, Wu NH, Nitsche A et al.:
 166. Zhao P, Praissman JL, Grant OC, Cai Y, Xiao T, Rosenbalm KE, Aoki K, Kellman BP, Bridger R, Barouch DH et al.: Virus-receptor interactions of glycosylated SARS-CoV-2 spike and human ACE2 receptor. *Cell Host Microbe* 2020, 28:586-601 e586.
 167. Watanabe Y, Allen JD, Wrapp D, McLellan JS, Crispin M: Site- specific glycan analysis of the SARS-CoV-2 spike. *Science* 2020, 369:330-333.
 168. Wrapp D, Wang N, Corbett KS, Goldsmith JA, Hsieh CL, Abiona O, Graham BS, McLellan JS: Cryo-EM structure of the 2019-nCoV spike in the prefusion conformation. *Science* 2020, 367:1260- 1263
 169. Walls AC, Park YJ, Tortorici MA, Wall A, McGuire AT, Velesler D: Structure, function, and antigenicity of the SARS-CoV-2 spike glycoprotein. *Cell* 2020, 183:1735
 170. Lan J, Ge J, Yu J, Shan S, Zhou H, Fan S, Zhang Q, Shi X, Wang Q, Zhang L et al.: Structure of the SARS-CoV-2 spike receptor- binding domain bound to the ACE2 receptor. *Nature* 2020, 581:215-220
 171. Shang J, Ye G, Shi K, Wan Y, Luo C, Aihara H, Geng Q, Auerbach A, Li F: Structural basis of receptor recognition by SARS-CoV-2. *Nature* 2020, 581:221-224
 172. Yan R, Zhang Y, Li Y, Xia L, Guo Y, Zhou Q: Structural basis for the recognition of SARS-CoV-2 by full-length human ACE2. *Science* 2020, 367:1444-1448.
 173. Wang Q, Zhang Y, Wu L, Niu S, Song C, Zhang Z, Lu G, Qiao C, Hu Y, Yuen KY et al.: Structural and functional basis of SARS-CoV-2 entry by using human ACE2. *Cell* 2020, 181:894-904 e899.
 174. Xia S, Liu M, Wang C, Xu W, Lan Q, Feng S, Qi F, Bao L, Du L, Liu S et al.: Inhibition of SARS-CoV-2 (previously 2019-nCoV) infection by a highly potent pan-coronavirus fusion inhibitor targeting its spike protein that harbors a high capacity to mediate membrane fusion. *Cell Res* 2020, 30:343-355.
 175. Cai Y, Zhang J, Xiao T, Peng H, Sterling SM, Walsh RM Jr, Rawson S, Rits-Volloch S, Chen B: Distinct conformational states of SARS-CoV-2 spike protein. *Science* 2020, 369:1586- 1592

176. Bangaru S, Ozorowski G, Turner HL, Antanasijevic A, Huang D, Wang X, Torres JL, Diedrich JK, Tian JH, Portnoff AD et al.: Structural analysis of full-length SARS-CoV-2 spike protein from an advanced vaccine candidate. *Science* 2020, 370:1089- 1094.
177. Yao H, Song Y, Chen Y, Wu N, Xu J, Sun C, Zhang J, Weng T, Zhang Z, Wu Z et al.: Molecular architecture of the SARS-CoV-2 virus. *Cell* 2020, 183:730-738 e713
178. Ke Z, Oton J, Qu K, Cortese M, Zila V, McKeane L, Nakane T, Zivanov J, Neufeldt CJ, Cerikan B et al.: Structures and distributions of SARS-CoV-2 spike proteins on intact virions. *Nature* 2020, 588:498-502
179. Turonova B, Sikora M, Schurmann C, Hagen WJH, Welsch S, Blanc FEC, von Bulow S, Gecht M, Bagola K, Horner C et al.: In situ structural analysis of SARS-CoV-2 spike reveals flexibility mediated by three hinges. *Science* 2020, 370:203-208
180. Liu C, Mendonca L, Yang Y, Gao Y, Shen C, Liu J, Ni T, Ju B, Liu C, Tang X et al.: The architecture of inactivated SARS-CoV-2 with postfusion spikes revealed by cryo-EM and cryo-ET. *Structure* 2020, 28:1218-1224 e1214
181. Walls AC, Tortorici MA, Bosch BJ, Frenz B, Rottier PJM, DiMaio F, Rey FA, Velesler D: Cryo-electron microscopy structure of a coronavirus spike glycoprotein trimer. *Nature* 2016, 531:114- 117.
182. Kirchdoerfer RN, Cottrell CA, Wang N, Pallesen J, Yassine HM, Turner HL, Corbett KS, Graham BS, McLellan JS, Ward AB: Pre- fusion structure of a human coronavirus spike protein. *Nature* 2016, 531:118-121.
183. Gui M, Song W, Zhou H, Xu J, Chen S, Xiang Y, Wang X: Cryo- electron microscopy structures of the SARS-CoV spike glycoprotein reveal a prerequisite conformational state for receptor binding. *Cell Res* 2017, 27:119-129.
184. Yuan Y, Cao D, Zhang Y, Ma J, Qi J, Wang Q, Lu G, Wu Y, Yan J, Shi Y et al.: Cryo-EM structures of MERS-CoV and SARS-CoV spike glycoproteins reveal the dynamic receptor binding domains. *Nat Commun* 2017, 8:15092.
185. Li Z, Tomlinson AC, Wong AH, Zhou D, Desforjes M, Talbot PJ, Benlekber S, Rubinstein JL, Rini JM: The human coronavirus HCoV-229E S-protein structure and receptor binding. *eLife* 2019, 8.
186. Zhang J, Cai Y, Xiao T, Lu J, Peng H, Sterling SM, Walsh RM Jr, Rits-Volloch S, Zhu H, Woosley AN et al.: Structural impact on SARS-CoV-2 spike protein by D614G substitution. *Science* 2021, 372:525-530
187. Fan X, Cao D, Kong L, Zhang X: Cryo-EM analysis of the post- fusion structure of the SARS-CoV spike glycoprotein. *Nat Commun* 2020, 11:3618.
188. Walls AC, Tortorici MA, Snijder J, Xiong X, Bosch BJ, Rey FA, Velesler D: Tectonic conformational changes of a coronavirus spike glycoprotein promote membrane fusion. *Proc Natl Acad Sci U S A* 2017, 114:11157-11162.
189. Zhou H, Chen Y, Zhang S, Niu P, Qin K, Jia W, Huang B, Zhang S, Lan J, Zhang L et al.: Structural definition of a neutralization epitope on the N-terminal domain of MERS-CoV spike glycoprotein. *Nat Commun* 2019, 10:3068.
190. Peng G, Xu L, Lin YL, Chen L, Pasquarella JR, Holmes KV, Li F: Crystal structure of bovine coronavirus spike protein lectin domain. *J Biol Chem* 2012, 287:41931-41938.
191. Chi X, Yan R, Zhang J, Zhang G, Zhang Y, Hao M, Zhang Z, Fan P, Dong Y, Yang Y et al.: A neutralizing human antibody binds to the N-terminal domain of the Spike protein of SARS-CoV-2. *Science* 2020, 369:650-655
192. Cerutti G, Guo Y, Zhou T, Gorman J, Lee M, Rapp M, Reddem ER, Yu J, Bahna F, Bimela J et al.: Potent SARS-CoV-2 neutralizing antibodies directed against spike N-terminal domain target a single supersite. *Cell Host Microbe* 2021

193. Voss WN, Hou YJ, Johnson NV, Delidakis G, Kim JE, Javanmardi K, Horton AP, Bartzoka F, Paresi CJ, Tanno Y et al.: Prevalent, protective, and convergent IgG recognition of SARS-CoV-2 non-RBD spike epitopes. *Science* 2021.
194. McCallum M, De Marco A, Lempp FA, Tortorici MA, Pinto D, Walls AC, Beltramello M, Chen A, Liu Z, Zatta F et al.: N-terminal domain antigenic mapping reveals a site of vulnerability for SARS-CoV-2. *Cell* 2021, 184:2332-2347 e2316
195. Li D, Edwards RJ, Manne K, Martinez DR, Schafer A, Alam SM, Wiehe K, Lu X, Parks R, Sutherland LL et al.: The functions of SARS-CoV-2 neutralizing and infection-enhancing antibodies in vitro and in mice and nonhuman primates. *bioRxiv* 2021.
196. Tong P, Gautam A, Windsor I, Travers M, Chen Y, Garcia N, Whiteman NB, McKay LGA, Lelis FJN, Habibi S et al.: Memory B cell repertoire for recognition of evolving SARS-CoV-2 spike. *bioRxiv* 2021.
197. McCarthy KR, Rennick LJ, Nambulli S, Robinson-McCarthy LR, Bain WG, Haidar G, Duprex WP: Recurrent deletions in the SARS-CoV-2 spike glycoprotein drive antibody escape. *Science* 2021, 371:1139-1142.
198. Wang P, Nair MS, Liu L, Iketani S, Luo Y, Guo Y, Wang M, Yu J, Zhang B, Kwong PD et al.: Antibody resistance of SARS-CoV-2 variants B.1.351 and B.1.1.7. *Nature* 2021, 593:130-135.
199. Li F, Li W, Farzan M, Harrison SC: Structure of SARS coronavirus spike receptor-binding domain complexed with receptor. *Science* 2005, 309:1864-1868.
200. Xiao T, Lu J, Zhang J, Johnson RI, McKay LGA, Storm N, Lavine CL, Peng H, Cai Y, Rits-Volloch S et al.: A trimeric human angiotensin converting enzyme 2 as an anti-SARS-CoV-2 agent. *Nat Struct Mol Biol* 2021, 28:202-209.
201. Zhou T, Tsybovsky Y, Gorman J, Rapp M, Cerutti G, Chuang GY, Katsamba PS, Sampson JM, Schon A, Bimela J et al.: Cryo-EM structures of SARS-CoV-2 spike without and with ACE2 reveal a pH-dependent switch to mediate endosomal positioning of receptor-binding domains. *Cell Host Microbe* 2020, 28:867-879 e865.
202. Gobeil SM, Janowska K, McDowell S, Mansouri K, Parks R, Stalls V, Kopp MF, Manne K, Saunders K, Edwards RJ et al.: Effect of natural mutations of SARS-CoV-2 on spike structure, conformation and antigenicity. *bioRxiv* 2021.
203. Cai Y, Zhang J, Xiao T, Lavine CL, Rawson S, Peng H, Zhu H, Anand K, Tong P, Gautam A et al.: Structural basis for enhanced infectivity and immune evasion of SARS-CoV-2 variants. *bioRxiv* 2021.
204. Piccoli L, Park YJ, Tortorici MA, Czudnochowski N, Walls AC, Beltramello M, Silacci-Fregni C, Pinto D, Rosen LE, Bowen JE et al.: Mapping neutralizing and immunodominant sites on the SARS-CoV-2 spike receptor-binding domain by structure-guided high-resolution serology. *Cell* 2020, 183:1024-1042 e1021.
205. Finkelstein MT, Mermelstein AG, Parker Miller E, Seth PC, Stancofski ED, Fera D: Structural analysis of neutralizing epitopes of the SARS-CoV-2 spike to guide therapy and vaccine design strategies. *Viruses* 2021, 13.
206. Hansen J, Baum A, Pascal KE, Russo V, Giordano S, Wloga E, Fulton BO, Yan Y, Koon K, Patel K et al.: Studies in humanized mice and convalescent humans yield a SARS-CoV-2 antibody cocktail. *Science* 2020, 369:1010-1014
207. Barnes CO, Jette CA, Abernathy ME, Dam KA, Esswein SR, Gristick HB, Malyutin AG, Sharaf NG, Huey-Tubman KE, Lee YE et al.: SARS-CoV-2 neutralizing antibody structures inform therapeutic strategies. *Nature* 2020, 588:682-687.
208. Huo J, Zhao Y, Ren J, Zhou D, Duyvesteyn HME, Ginn HM, Carrique L, Malinauskas T, Ruza RR, Shah PNM et al.: Neutralization of SARS-CoV-2 by destruction of the prefusion spike. *Cell Host Microbe* 2020, 28:445-454.e446.

209. Haschke M, Schuster M, Poglitsch M, Loibner H, Salzberg M, Bruggisser M, Penninger J, Krahenbuhl S: Pharmacokinetics and pharmacodynamics of recombinant human angiotensin- converting enzyme 2 in healthy human subjects. *Clin Pharmacokinet* 2013, 52:783-792.
210. Monteil V, Kwon H, Prado P, Hagelkruys A, Wimmer RA, Stahl M, Leopoldi A, Garreta E, Hurtado Del Pozo C, Prosper F et al.: Inhibition of SARS-CoV-2 infections in engineered human tissues using clinical-grade soluble human ACE2. *Cell* 2020, 181:905-913 e907.
211. Chan KK, Dorosky D, Sharma P, Abbasi SA, Dye JM, Kranz DM, Herbert AS, Procko E: Engineering human ACE2 to optimize binding to the spike protein of SARS coronavirus 2. *Science* 2020, 369:1261-1265.
212. Cao L, Goreshnik I, Coventry B, Case JB, Miller L, Kozodoy L, Chen RE, Carter L, Walls AC, Park YJ et al.: De novo design of picomolar SARS-CoV-2 miniprotein inhibitors. *Science* 2020, 370:426-431.
213. Dai L, Gao GF: Viral targets for vaccines against COVID-19. *Nat Rev Immunol* 2021, 21:73-82.
214. Chan DC, Fass D, Berger JM, Kim PS: Core structure of gp41 from the HIV envelope glycoprotein. *Cell* 1997, 89:263-273.
215. Weissenhorn W, Dessen A, Harrison SC, Skehel JJ, Wiley DC: Atomic structure of the ectodomain from HIV-1 gp41. *Nature* 1997, 387:426-430.
216. Zhang, Jun, et al. "Structure of SARS-CoV-2 spike protein." *Current Opinion in Virology* 50 (2021): 173-182.
217. Fernández, Ariel. "Structural impact of mutation D614G in SARS-CoV-2 spike protein: enhanced infectivity and therapeutic opportunity." *ACS medicinal chemistry letters* 11.9 (2020): 1667-1670.